POLITECNICO DI TORINO

Corso di Laurea Magistrale
in Ingegneria Aerospaziale

Tesi di Laurea Magistrale

COMPRESSOR AERODYNAMICS AT NEGATIVE INCIDENCE

Academic Supervisors:
Prof. Dario Giuseppe Pastrone
Prof. Vassilios Pachidis

Candidate:
Giulio Lovo

PhD Advisor:
Luis Ferrer-Vidal

August 2019

ABSTRACT

In the last decades, customers and regulators are continuously imposing more stringent requirements on safety, emissions and fuel consumption, pushing the manufacturers to optimise every single phase of the engine operations. Many goals in design point operations and off-design ones have already been reached. However, in order to meet the requirements on ground start and altitude relight capabilities, the sub-idle regime performance still needs to be fully comprehended. In this regime, the engine is operating at a speed below the idle one and, since these are extreme off-design conditions, innovative approaches to create high-fidelity prediction tools are required. For this purpose, one of the main challenges is to further understand the compressor behaviour. Many performance tools are available to predict it near design point, but, due to the lack of experimental data and the complexity of the flow, they are not reliable for sub-idle conditions. Hence, in the previous years, in Cranfield University a surrogate model for loss and deviation in sub-idle conditions was developed to be implemented in mean-line or through-flow codes. The maps generated through these tools will then be used for the whole engine sub-idle performance analysis.

The main target of this research was then to improve and generalise this model by considering the effects of the camber angle and of the flow unsteadiness. Using the same 2D CFD parametric model, different blade geometries were considered. The results are suggesting that the camber angle has no effect on the flow deviation. For the pressure loss coefficient, a clear trend was not found probably due to the flow unsteadiness. Hence, transient simulations were performed, assessing the behaviour of the employed turbulence models as well. For the deflection case, the results were confirming the steady-state outcomes in all the cases. Regarding the pressure loss coefficient, there was a discrepancy between the data: the SAS-SST model behaved in a different way depending on the considered geometry, probably due to its scale-adaptive capacity, that in case of a parametric model makes impossible to have a fair comparison. However, the model has been used in the mean-line code, generating compressor maps that were successfully validated against experimental data.

Keywords: axial-flow compressors, compressor performance, deviation angle, mean-line code, surrogate modelling, total pressure loss coefficient, turbulence modelling, sub-idle regime

ACKNOWLEDGEMENTS

First of all, I would like to thank Professor Vassilios Pachidis for allowing me to be part of the Cranfield University Technology Centre and to give my contribution to one of the most interesting projects, and to support me in my work. A special thank should go to Professor Pericles Pilidis for giving me the opportunity to study this year at Cranfield University. Another important thank should go to my PhD advisor Luis Ferrer-Vidal, always present and ready to support and suggest me at every time. Moreover, thanks to him for teaching me and pushing me to think with a different and better approach to my results. I would like to thank Professor Dario Pastrone as well for giving me the possibility to present my individual research project at Politecnico di Torino.

During the year, I lived moments that I never imagined to experience, from the happiest to the, unfortunately, saddest ones. In all those moments I had great friends next to me. I would like then to give an extraordinary thank to Grigoris and Federico for supporting me and for always being present to talk and to discuss together. My appreciation goes also to the other friends I met during the year, that lived the experience with me: Sharan, Santiago, Stephanos and Leon.

Finally, my gratitude should go to the people that were supporting me from Italy, away but always close to me. Thanks to my parents Emilia and Livio, for growing me up giving me the values and the means to face head-on every challenge that was presented to me. And then a special thanks to my brother Luca, always ready for everything I could ask. My gratitude should then go to my friends: first, Stefano, for listening to me in every occasion and supporting me. Then, Alessio, Riccardo and Anthony, that always tried to understand and advise me in the best way. I should then thank Simone, Luca, Massimiliano and Chiara. I am finally grateful to Luca, my coach and mentor when I was swimming, for teaching me to never give up and to be proud of myself.

TABLE OF CONTENTS

LIST OF FIGURES

LIST OF TABLES

LIST OF EQUATIONS

LIST OF ABBREVIATIONS AND SYMBOLS

Abbreviations

1D	One Dimensional
2D	Two Dimensional
3D	Three Dimensional
CFD	Computational Fluid Dynamic
CM	Corrected Mass-flow
CN	Corrected Shaft Rotational Speed
DCA	Double Circular Arc
MCA	Multi Circular Arc
N	Shaft Rotational Speed [rpm]
PR	Pressure Ratio
RANS	Reynolds Averaged Navier-Stokes
SAS	Scale-Adaptive Simulations
SFC	Specific Fuel Consumption [kg/MN]
URANS	Unsteady Reynolds Averaged Navier-Stokes

Latin Symbols

c	Blade Chord [m] or Absolute Flow Velocity [m/s]
c_p	Air Specific Heat at Constant Pressure [J/kg K]
DF	Diffusion Factor
H	Specific Total Enthalpy [J/kg]
M	Mach Number
P	Pressure [Pa]
R	Ideal Gas Constant [J/kg K]
Re	Reynolds Number
s	Specific Entropy [J/kg K] or Blade Spacing [m]
t	Blade Thickness [m]
T	Temperature [K]
U	Blade Speed [m/s]
w	Relative Flow Velocity [m/s]
i	Incidence [deg]

Greek Symbols

η_{is}	Efficiency
α	Flow Angle [deg]
β	Blade Metal Angle [deg]
γ	Stagger Angle [deg] or Air Adiabatic Coefficient
δ	Deviation Angle [deg]
θ	Camber Angle [deg]
ρ	Density [kg/m^3]
σ	Solidity
φ	Stage Loading
ψ	Flow Coefficient
ω	Total Pressure Loss Coefficient

Subscripts

a	Axial Component
bl	Baseline
θ	Tangential Component
0	Total
1	Rotor Inlet Conditions
2	Rotor Exit/Stator Inlet Conditions
3	Stator Exit Conditions

1 INTRODUCTION

1.1 Sub-idle Operations

During its operations, a modern civil aero-engine is subjected to many different regimes, depending on the mission phase. In each of these conditions, the main requirement is to maximise the fuel efficiency and to deliver the required thrust or power output, without penalising safety and reliability. Throughout the years, in order to optimise every operating condition, many simulation software have been developed to model the engine performance in the typical operating conditions of the whole mission, such as take-off, climb, cruise and landing. In all these cases, although the engine is not operating in its design point, the prediction accuracy can be very high since plenty of research has been carried on. However, in the past, the off-design analysis and optimisation have been usually limited above the idle condition, defined as the one in which the shaft rotational speed is in a range between 40% and 70% of design one[1]. This speed is the lowest one at which the engine can be considered in stable operations without the need for auxiliary power sources.

Nonetheless, there are some other extreme off-design conditions that the engine experiences during its operations, such as ground start-ups or potential altitude relights. In these cases, the engine will operate well below the idle regime, hence in much different and extreme operating conditions, extremely complex to analyse and predict. In fact, in such phases the low shaft rotational speed, combined with the possible reduced mass flow, will lead the compressor blades to experience very high negative incidence angles, with wide separation zones. The flow will then encounter higher losses and much different deflection angles, with a limited capacity of the compressor to efficiently compress it. In very extreme cases, the compressor can behave like a turbine extracting energy from the flow, in a phenomenon called wind-milling. This event will lower the total pressure and temperature of the combustor incoming flow, limiting the capacity of igniting the flame. During a ground start-up, this will affect the fuel consumption and the start-up time, leading to higher operating cost. During the possible

altitude relight, this will affect not only the above-mentioned factors but, much more important, the achievement of the safety requirements of the engine, limiting its capacity to quickly recover the thrust.

For these reasons, sub-idle performance analysis has become very important in the last two decades, in order to further reduce the airlines operating costs and achieve the stringent safety regulation requirements in terms of altitude relight. Indeed, this allows to simulate more accurately the flow conditions at the combustor inlet, enabling a more accurate sizing of it and possibly saving time and cost of the design by reducing the possible errors in the initial phases. Of course, these issues will not affect ground-based gas turbines since start-ups are not as usual as in aviation[2].

However, the conventional performance tools are not suitable to simulate the engine performance in sub-idle conditions with acceptable accuracy. Thus, innovative approaches and models are required to achieve it. In the last years, many studies have been conducted at Cranfield University to model and simulate this particular operating condition. One of these is the doctoral research performed by Luis Ferrer-Vidal, in which the aim is to develop a whole engine model for sub-idle conditions. For the compressor modelling, a mean line code has been developed: once provided the compressor geometry, will be able to generate the corresponding map using the set of correlations developed among the previous and the current MSc project.

1.2 Compressor Sub-idle Performance Modelling

A gas turbine is intended to operate at design point for most of its operating conditions (e.g. in cruise flight). However, the engine is supposed to operate in off-design conditions as well. This is the case of mission phases such as taxing, in which the engine is in ground-idle, landing approach, in which the engine is in flight-idle, or in any other condition different from design one. In these off-design conditions, above the idle regime, enough test data are available to validate the maps found through mathematical models and, hence, to have high fidelity in using the performance simulation codes [3].

Nonetheless, there are some extreme off-design conditions that cannot be classified in the above-mentioned category. It is the case of the sub-idle operating ones that, as defined in the previous paragraph, occur when the engine operates below 40% of the design rotational speed. The engine will then experience flow conditions very different from the usual ones and, in many cases, the validity range of the models is not as wide as it is needed. Sub-idle operations occur when the engine, from zero or very low rotational speed, needs to accelerate up to idle speed, hence during ground start-ups or possible altitude relights. Since the flow is very complex, engine performance modelling is very difficult in these particular conditions, considering also the lack of experimental data to validate them.

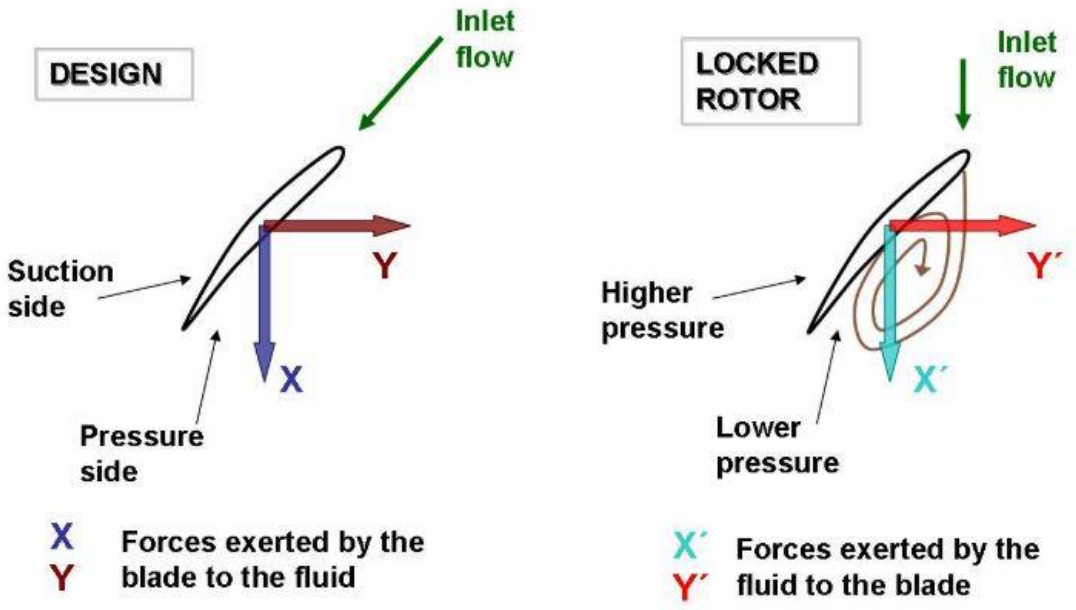

Figure 1-1: Blade inlet flow angle: design point (on the left) and locked rotor condition (on the right) [4]

In Figure 1-1, on the right, is shown the flow configuration encountered in such extreme conditions. The velocity triangles are heavily distorted by the zero or very low linear speed of the blades. In fact, due to the low shaft rotational speed and the incoming mass flow from the previous stages, that delivers a considerable axial velocity, the blade inlet flow will have very high incidence angles, arriving up

to negative incidence of around $-60°$ [5]. For this reason, it will present a big separation zone on the pressure side of the blade that will lead to bigger losses and very different deflection angles when compared to the design ones. Eventually, the deflection can change in such a way that, becoming negative, the compressor starts behaving like a turbine in a phenomenon called wind-milling [6].

In order to have a good understanding of the compressor performance and, finally, of the engine behaviour, it is important to create the tools that allow to do it with the highest possible accuracy. In compressors design, a very important one is the component map, that allows to describe its operating conditions in a very simple way. From the map, it is then possible to proceed with the engine performance modelling in both design and off-design conditions, with the variable already defined in each point.

It is very important to simulate the performance and proceed to the optimisation before the engine prototype is manufactured and tested. By doing this, design cost and time will be reduced since the major issues can be fixed in the preliminary phases. The resulting engine will have enhanced operability and efficiency, with lower fuel consumption, costs and emissions. From the safety point of view, the legislation requirements will be fulfilled without penalising too much the performance.

1.2.1 Compressor Maps

The compressor map, as mentioned before, is directly dependent on its geometry, defined to satisfy the fixed design point requirements. Moreover, it needs to take into consideration the optimisation, in order to extend the “efficiency flat zone” range as much as possible, having the wider possible operability of the engine and the higher possible stability [7].

In the compressor case, the map will provide the following parameters:

- *Pressure Ratio*: $PR = \frac{P_{0_2}}{P_{0_1}}$

- *Non-dimensional Mass-flow*: $CM = \frac{W\sqrt{T_{0_1}}}{P_{0_1}}$
- *Isentropic Efficiency*: $\eta_{is} = \frac{\left(P_{0_2}/P_{0_1}\right)^{\frac{\gamma-1}{\gamma}} - 1}{T_{0_2}/T_{0_1} - 1}$
- *Non-dimensional Rotational Speed*: $CN = N/\sqrt{T_{0_1}}$

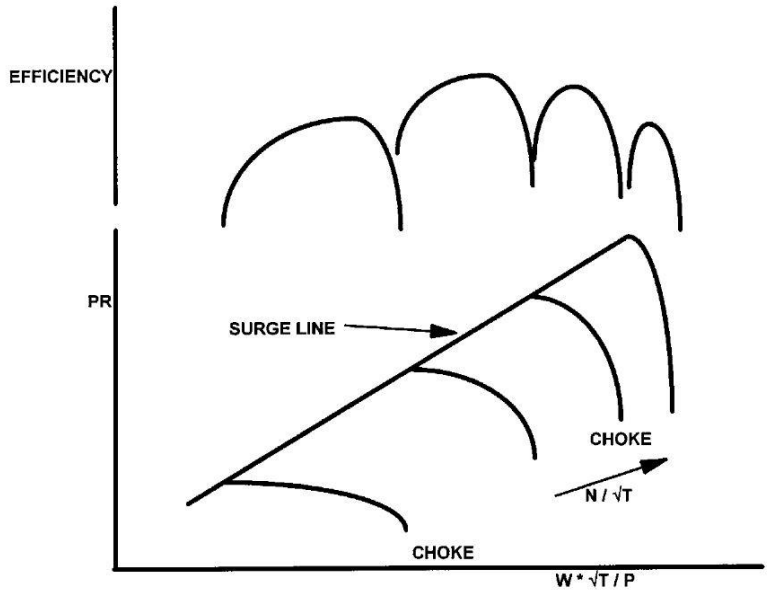

Figure 1-2: Typical compressor map [1]

The map generation can be usually made in two different ways:

- *Experimental rig testing*: a real model of the compressor is run controlling both the shaft rotational speed, through an electric motor, and the mass flow, through a valve, and measuring the resulting overall pressure ratio and the relative efficiency. The points are then plotted, generating the corresponding speed lines. This method cannot be used in a preliminary design phase since it requires a compressor prototype to run. Moreover, only discrete conditions can be tested, with the need to interpolate the data between the tested conditions. Usually, for similar geometries, previous designs maps can be scaled and adapted to the design operating point, allowing to have a first-order tool in the preliminary phases.
- *Numerical modelling*: in a preliminary design phase, the map can be generated by using mean-line (1D) or through-flow (2D, quasi-3D) codes.

These tools consider blade and compressor geometries and calculate each operating point of the map by assuming the total pressure loss and deviation angle values from models based on empirical, analytical or numerical correlations.

It is important to notice that some attempts to develop full 3D simulations of a compressor has been done. This approach is though very complex: due to the very high computational time of the simulations, is not possible to develop a complete characteristic map, but only discrete points. Nevertheless, it can be used to validate some of the points from the above-mentioned processes [6].

1.2.2 Sub-idle Compressor Map Generation

As in any other typical off-design performance models, also in sub-idle ones the codes will need a map to derive the operating parameters. The maps can be found with three main methods, considering that above the idle speed the maps can be already available and reliable [8]:

- *Experimental rig testing*: this is probably the best approach from the physical point of view since it will include the real problem with all the possible mechanism of losses. However, the measurements can include errors due to the complexity of the flow, highly turbulent, and the cost for the testing rig will be high. For this reason, this method is usually employed to validate the following two methods with experimental data, rather than create a complete map [9].
- *Map extrapolation*: in this method, the zero-speed line is extrapolated from existing maps through mathematical algorithms, hence without a real physical meaning (Figure 1-3). The main assumption is that compressibility effects, as well as Reynolds and Mach number effects, are negligible, oversimplifying the approach. However, this is the most used method until now, with many application in Cranfield University in past years, and validation against experimental test data [10]
- *Map interpolation*: in this method, the portion of the map at sub-idle speed is found by interpolating existing data with a zero-speed line (or locked-

rotor line) that is found through very computational expensive 3D CFD simulations or less sophisticated mean-line (1D) or through-flow (2D) codes. Certainly, the physical meaning of this zero-speed line will be more important rather than the extrapolated one. In case of 1D or 2D codes, the line is generated exploiting total pressure loss coefficient and deviation angle models, that need to be as accurate as possible to avoid errors that could propagate.

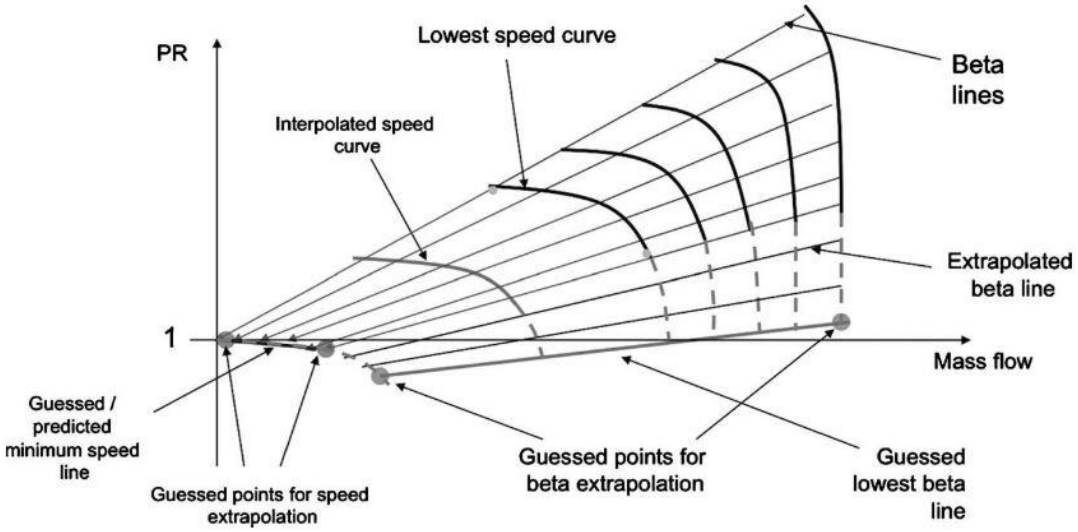

Figure 1-3: Typical extrapolated map, as many methods are based on [11]

It is important to notice that existing loss and deviation models are not suitable for extreme off-design conditions. This means that they may be not valid for the very high negative incidence angles that occur in sub-idle operations since they consider only low incidence angles. In order to fill this knowledge gap, there is the necessity to make further improvements in this topic, researching for alternative models that consider also very extreme inlet blade conditions.

1.3 Aim and Objectives

In this research project, the main aim is to improve and generalise the previous total pressure loss coefficient and deviation angle correlations for compressors blades operating in sub-idle conditions, developing them as a function of stagger angle, solidity, incidence angle and camber angle. Since much work has already

been carried on this topic, some of the correlations are already in use. The target is to continue the analysis by considering more geometries of HP and IP modern compressors and, hence, different camber angles. Once this task is concluded, the following target is to assess the effects of turbulence and instabilities in the flow, that can be significant considering the wide separation zones. In this second phase, the range of validity of the existing correlations will be evaluated throughout the use of 2D transient simulations. The research will be carried on using the ANSYS Software package to run and post-process the CFD simulations, as well as MATLAB.

The main objectives of the project are:

- Adapt the previous model to the different blade geometries
- Run the steady-state cases varying parametrically incidence angle, solidity and camber angle
- Check and confirm previous year correlations
- Investigate camber angle influence, possibly developing a correction for the baseline correlations
- Investigate flow unsteadiness effects, possibly developing a correction for the baseline correlations

1.4 Thesis Structure

In the following pages the thesis structure is described, presenting the main steps followed during the project progress:

Chapter 2 will include the literature review: the relevant background theory and previous work are provided. The basics of axial compressors are presented, describing the features necessary for understanding the compressors' performance in sub-idle conditions. Finally, the previous work done on this topic is presented, focusing on the available total pressure loss coefficient and deviation angle models.

Chapter 3 will describe the methodology used for the current project, presenting the numerical set-up used for ANSYS Fluent and the main settings for both

steady-state and transient models. The investigation parameters and the assessment methodology of error and accuracy are presented as well. The main turbulent flow models will be presented, with a focus on the flow features developed in case of sub-idle operating conditions.

Chapter 4 will include the results of the project, with a discussion about their validity and accuracy, considering aerodynamic and numerical issues in such complex cases.

Chapter 5 will resume the main results of the project and will present the conclusions, highlighting the validity and the accuracy of the relationships. Finally, suggestions for further work will be provided.

2 LITERATURE REVIEW

In this section, an overview of axial flow compressors is provided, highlighting the main issues that occur when they come to work in sub-idle conditions. Then the principal total pressure loss coefficient and deviation models are presented, describing their validity range and application limits.

2.1 Axial Flow Compressors

The purpose of axial flow compressors is to increase the total pressure of the flow in the most efficient way, limiting the energy losses. In an axial compressor (Figure 2-1), the working fluid flows parallel to the axis, allowing to deliver a higher mass flow rate compared to centrifugal compressors. Nonetheless, the typical PR is lower, hence a higher number of stages is needed, compared to the centrifugal ones.

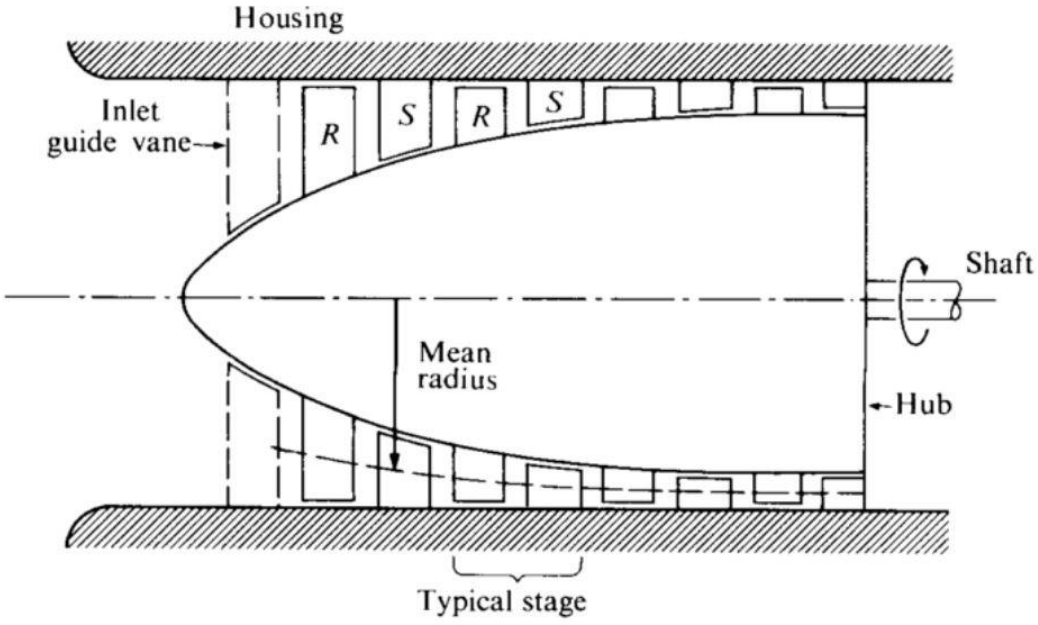

Figure 2-1: Axial compressor scheme [12]

As can be seen from Figure 2-2, a compressor stage is composed of a rotor and a stator coupled together. In the rotor, due to the blades' rotation, the energy coming from the turbine is introduced in the flow as kinetic energy. In the stator,

that kinetic energy is recovered in total pressure through a diffusion process. In fact, the blade passages will behave like a diffuser, reducing the flow velocity and, assuming the conservation of mass, increasing the static pressure.

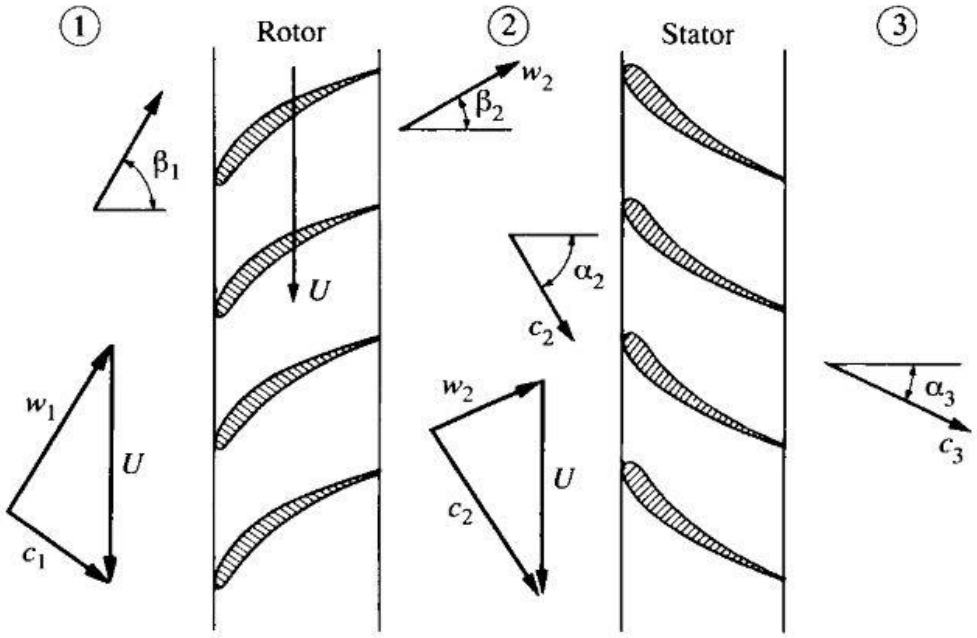

Figure 2-2: Compressor stage and velocity triangles [12]

Since there is a rotating part, two different reference systems will be adopted, an absolute one, fixed with the stator, and a relative one, jointed to the rotor. Hence two different velocities can be defined: an absolute one, related to the absolute reference frame ($\mathbf{c}$), and a relative one, related to the rotating reference frame ($\mathbf{w}$). These two velocities will be related through the blade speed $\boldsymbol{U}$ employing the vector addition [12]:

$$\mathbf{c} = \mathbf{U} + \mathbf{w} \tag{2-1}$$

The combination of rotor and stator action will lead to the velocity triangles (Figure 2-2). These are the result of the flow deflection delivered by the compressor blades.

Since the compression is required, the blade passages are designed to create diffuser-like passages, with an outlet flow area greater than the inlet one, allowing

the flow to decelerate and recovering the static pressure. However, the adverse pressure gradient developed on the blade surface throughout this geometry will limit the possible flow deflection and, hence, the typical value of a stage pressure ratio is limited to $PR \sim 1.6 - 1.8$. It is important to notice that in compressor blades, the cascade effect plays an important role, allowing to have higher deflection compared to an isolated blade with the same profile. The limitation will lead to the presence of several compressor stages to deliver the required pressure ratio, that in modern compressors is around 40, although the trend is to increase it up to about 60 to meet the more stringent SFC requirements [13].

2.1.1 Velocity Triangles and Euler's Equation

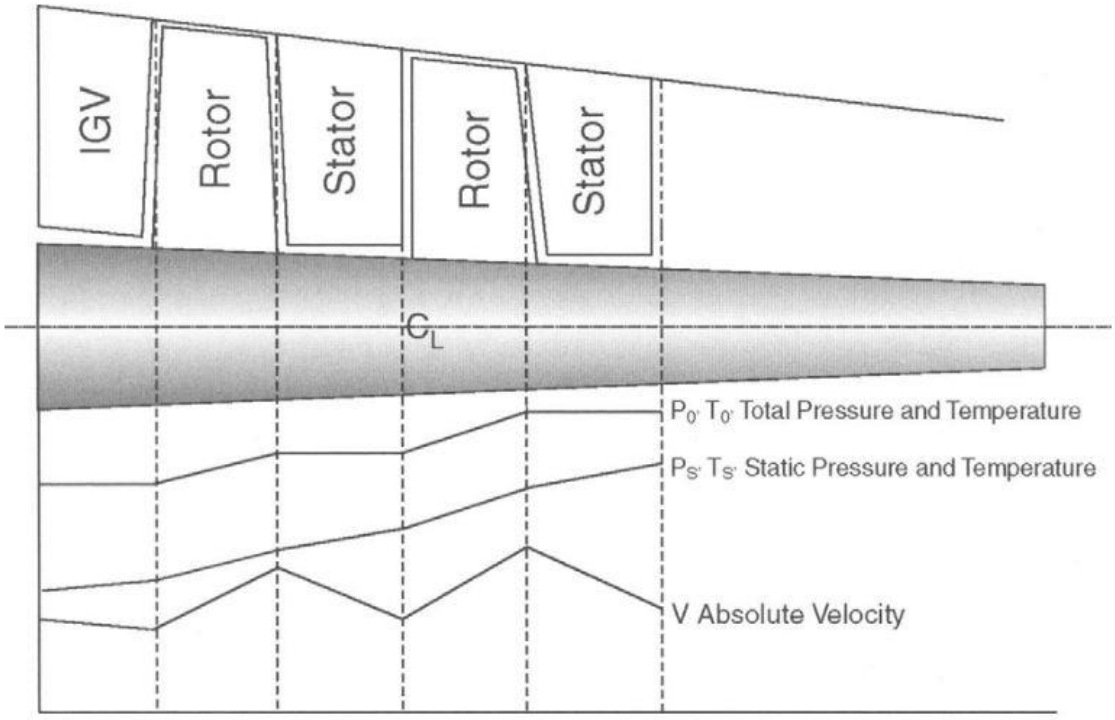

Figure 2-3: Main flow properties along the compressor [13]

As can be seen from Figure 2-2, since there are two different reference frames there will be two different velocities to take into account. Depending on the considered blade row, they will behave in a different way (Figure 2-3):

- *Rotor*: in the rotor there will be the need to consider both relative and absolute velocities. As can be seen, since the effect of rotation is to

increase the kinetic energy of the flow, the exit absolute velocity (c_2) will be greater than the inlet one (c_1). However, due to the geometry of the blade passages, designed with a diffuser-like shape, in the rotor part of the static pressure will be recovered, with an entity determined by the stage reaction. In fact, as can be seen, the relative velocity will decrease, with w_2 smaller than w_1.

- *Stator*: in the stator, only the absolute velocity will need to be considered; as can be seen, no work is done, since it has only the function to convert the kinetic energy introduced by the rotor in the actual pressure rise and to realign the flow to the required direction. This is done by decreasing the flow velocity, with c_3 lower than c_2.

Each blade will introduce a deflection in the flow that, as the Euler's equation states, can be related to the work done [7]:

$$\Delta \mathrm{H} = \mathrm{U}_1 c_{\theta_1} - U_2 c_{\theta_2} = \mathrm{U}_1 w_{\theta_1} - U_2 w_{\theta_2} \quad \textbf{(2-2)}$$

In case of a compressor with a constant mean radius, then $\mathrm{U}_1 = \mathrm{U}_2$ and the Euler's equation can be written as:

$$\Delta \mathrm{H} = \mathrm{U}\left(c_{\theta_1} - c_{\theta_2}\right) = \mathrm{U}\,\Delta c_\theta = \mathrm{U}\left(w_{\theta_1} - w_{\theta_2}\right) = \mathrm{U}\,\Delta w_\theta \quad \textbf{(2-3)}$$

The velocity triangles can also be non-dimensionalised by using the blade speed; the result will be two main parameters of compressor stages:

- Stage Loading: $\psi = \frac{\Delta c_\theta}{U} = \frac{\Delta w_\theta}{U} = \frac{\Delta H}{U^2}$
- Flow Coefficient: $\varphi = \frac{c_a}{U}$

These parameters will be directly linked to the compressor map ones since through the isentropic efficiency, once known the energy input, it is possible to derive the pressure ratio delivered by the compressor.

2.1.2 Blades and Cascade Geometry Definition

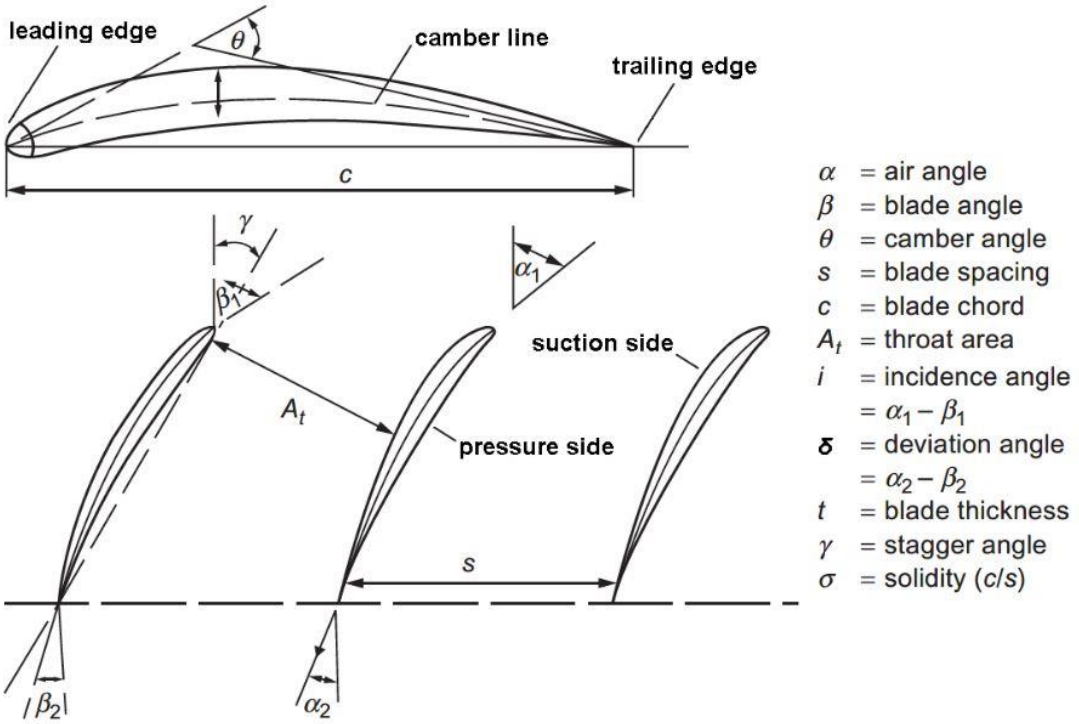

Figure 2-4: Cascade and blade parameters [13]

The required velocity triangles will be delivered by the cascade geometry, that is constituted by several blades placed in a row [13]. As can be seen from Figure 2-4, it is possible to define the cascade with several parameters; the most important are:

- *Flow inlet and outlet angles* (respectively, α_1 and α_2)
- *Blade inlet and outlet metal angles* (respectively, β_1 and β_2)
- *Incidence angle* ($i = \alpha_1 - \beta_1$), this is of primary importance, since the flow features will depend on this, affecting directly total pressure loss coefficient and deviation angle
- *Camber angle* ($\theta = \beta_1 - \beta_2$): assuming to be in design point conditions, with a deviation angle and incidence equal to 0, this will be the actual deflection that the blade will deliver to the flow. In an off-design condition, the flow will not be able to follow the blade shape, having a deflection angle different from the camber one.

- *Stagger angle* (γ): this is the angle between the blade chord and the reference axis. Assuming constant spacing, it will influence the throat area of the cascade
- *Blade chord* (c)
- *Blade spacing* (s)
- *Solidity* ($\sigma = c/s$): it is the non-dimensionalised parameter of the blade spacing, affecting the throat area and the cascade effect on the flow: much closer are the blades, more guided will be the flow (hence a lower deviation angle will occur); however, increasing the solidity, the throat area will be lower, with a higher flow velocity, and the surface area higher, with higher friction losses.
- *Blade thickness* (t)

All the angles defined in this way are referred to the z-axis of the compressor, thus to the axial direction [13].

2.2 Models for Total Pressure Loss Coefficient and Deviation Angle

In the following, the definition of both total pressure loss coefficient and deviation angle is provided, and a brief overview of the main models for total pressure loss coefficient and deviation angle is presented.

2.2.1 Total Pressure Loss Coefficient models

While in an ideal case, since the flow is assumed adiabatic and no losses are considered, the compressor efficiency will be equal to one, in a real case it will be around 85-90% [13]. The work absorbed by the compressor to deliver the same pressure ratio will then be higher, reducing the net energy available. The efficiency of a process is usually related to the increase in the flow entropy, that is a function of the total temperature and the total pressure, following the Gibb's equation [12]:

$$\mathrm{ds} = \mathrm{c_p}\frac{dT_0}{T_0} - R\frac{dP_0}{P_0} \qquad \textbf{(2-4)}$$

However, since in many cases the flow can be assumed to be adiabatic in the blade reference system (in both rotor and stator cases), the stagnation temperature can be assumed constant, leading to a direct dependence of the total pressure loss coefficient from the entropy increase. Thus, it is useful to define the total pressure loss coefficient to take into account the entropy increase and, hence, the process efficiency [14]:

$$\omega = \frac{\mathrm{P}_{0_1} - P_{0_2}}{P_{0_1} - p_1} = \frac{\mathrm{P}_{0_1} - P_{0_2}}{{}^{1}/_{2}\,\rho c_1^2} \qquad \textbf{(2-5)}$$

It is indeed simpler to measure the total pressure of the flow rather than finding indirectly through equations its entropy.

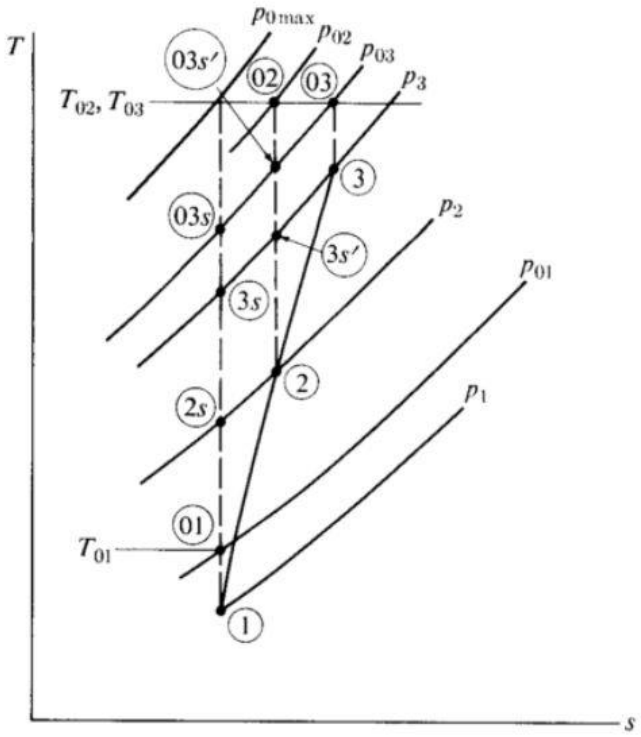

Figure 2-5: T-s Diagram for a compressor stage [12]

In a cascade, many sources of loss will be present. Usually, to take into account their effects, they are considered separately, with the overall total pressure loss coefficient that is the accumulation of them. However, they are usually interacting,

giving a non-linear effect. As stated in Dixon [7], they can be divided into 2D and 3D ones. About 2D ones, they derive from:

- *Boundary layer*: due to the viscous friction, a rise in entropy will be expected; it is dependent on the boundary layer characteristics and, hence, on the velocity profile on the blade, determined by its shape and by the blade surface finish.
- *Trailing edge mixing*: at the exit of the blade, the flow has different pressure and velocity; in order to reach the equilibrium, mixing losses will be expected between the two layers, depending on the blade trailing edge thickness and the difference of pressure and velocity [15].
- *Flow separation*: especially in off-design operation, the boundary layer will separate due to the adverse pressure gradient and the bigger wake will lead to very high turbulent processes; these are the losses that most likely occur in sub-idle operations, with the highest impact on the pressure loss coefficient [8]
- *Shock waves*: in case a sonic Mach number is reached in the blade passages, the occurring shock will lead to losses. These are not significant for the current project

It is important to notice that in sub-idle operating conditions, due to the high negative incidence flow, the pressure side flow separation is not occurring because of the negative pressure gradient, that still can be present, but because of the great efforts that the flow needs to do to overcome the blade leading edge from the stagnation point located on the suction side: the flow acceleration is such high that it can't remain attached to the blade surface [8][16].

About the 3D losses, they mainly come from:

- *End wall effects*: the interaction between the blade boundary layer and the inner and outer walls will lead to secondary flows
- *Tip leakages*: the flow that escapes from the blade tips will create secondary flows

In both the two 3D cases, the result is, in general, the formation of secondary flows that, going in another direction from the expected one, are preventing the delivery of the required pressure ratio.

However other sources of loss, not included in the previous ones, will occur, such as the effects of unsteadiness that bring to the vortex generation in the blade wake, causing high levels of turbulent kinetic energy and high viscous losses [15].

In the following are presented some of the total pressure loss coefficient models developed from the 50s in order to better analyse and predict the engine performance with the use of hand-made calculations, in the early phases, or computational methods in the most recent years.

Howell [17]

In his work, Howell tried to develop a fluid dynamic theory for flows through compressor blade passages, considering it in a perspective of performance estimation and design. The theory is based on the characteristics of the flow through a 2D blade cascade, considering then correction factors to give the mean stage condition in the compressor.

He related the total pressure loss coefficient $\bar{\omega}$ of the cascade to the drag coefficient of the blade c_D, through the equation:

$$c_D = \frac{s}{c}\frac{\bar{\omega}}{\frac{1}{2}\rho V_1^2}\frac{\cos^3 \alpha_m}{\cos^2 \alpha_1} \qquad \textbf{(2-6)}$$

In this way, it is easy to use the data from experimental tests to find the actual total pressure loss coefficient. As it is visible in Figure 2-6, both the drag coefficient and the total pressure loss coefficient have a flat range from $i = -10°$ to $i = 0°$ in which they are at their minimum value. Out of this range, towards both the choke and the stall conditions, their value increases rapidly due to the higher complexity of the flow.

In the paper, the drag coefficient is assumed to be composed of three main parts:

- c_{D_p}, defined as the profile drag coefficient, caused by the boundary layer development on the blades, determined through experimental tests;
- c_{D_a}, defined as the annulus drag coefficient, caused by the effects of friction on the annulus walls
- c_{D_s}, defined as the secondary drag coefficient, that comprises all the secondary losses effects, such as the effect of trailing edge vortices.

$$c_D = c_{D_p} + c_{D_a} + c_{D_s} \quad \textbf{(2-7)}$$

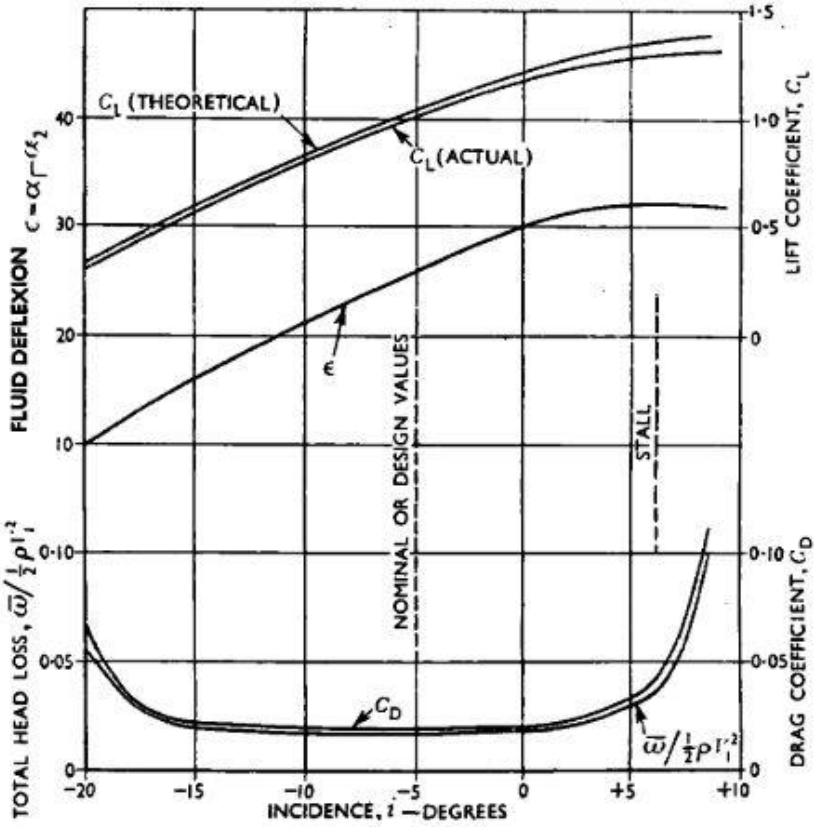

Figure 2-6: Typical low-speed cascade experimental test results [17]

Lieblein [18]

In this NACA report is presented a theoretical analysis in which the main assumption is that the total pressure loss coefficient is basically dependent on the boundary layer and the wake properties, considering then as a correction the

additional influence of the wake mixing and the 3D effects. The equations are found for both an arbitrary downstream plane and a far downstream plane to capture the complete mixing condition, assuming a 2D incompressible flow.

Considering the arbitrary downstream plane (at x position), the total pressure loss coefficient can be expressed as:

$$\bar{\omega}_x = f\left(\frac{\theta}{c}, \sigma, \frac{1}{\cos\alpha_2}, H\right) \quad \textbf{(2-8)}$$

Where θ is the blade momentum thickness and H is the boundary layer form factor, that affect the mixing process. Although this correlation has been validated against experimental data, it is valid only for unseparated flow and, hence, for conditions very close to the optimal ones in the design point. At high negative incidence, as it is considered in the current project, the assumptions of this theory are not valid anymore due to the flow separation. It has been shown that, for high values of the trailing edge thickness, its effect can be very significant on the losses due to the increased turbulence.

In case of the far downstream plane (at stage 2), the equation is simplified as:

$$\bar{\omega}_2 = f\left(\frac{\theta}{c}, \sigma, \frac{1}{\cos\alpha_2}\right) \quad \textbf{(2-9)}$$

Since the low value of H is not affecting it. For both cases, it is clear the influence of aerodynamic factors, such as the air outlet angle α_2 and the boundary layer momentum thickness θ, and geometric factors, like the chord length and the solidity.

Swan [19]

In this paper, a method for predicting the performance of transonic compressors is described. With this target, the behaviour of a 3D flow within the compressor is deduced from both theory and statistic data, assuming the real flow effects, such as the viscous losses and the shocks at the inlet, as a function of the blade

loading parameter. Indeed, it takes the Lieblein's 2D approach and tries to expand it to the 3D flows, considering experimental data as well.

The total pressure loss coefficient can hence be approximated as:

$$\bar{\omega} = \frac{\theta}{c}\frac{2\sigma}{\sin\alpha_2}\left(\frac{\sin\alpha_1}{\sin\alpha_2}\right)^2 \qquad \textbf{(2-10)}$$

The wake momentum thickness parameter θ/c is then related to the pressure losses, considering also the solidity and the air angles.

The analysis splits the losses into two different parts: the minimum loss, in which is considered the flow behaviour at conditions close to design point, and the off-minimum loss, in which are considered all the other effects occurring in off-design conditions.

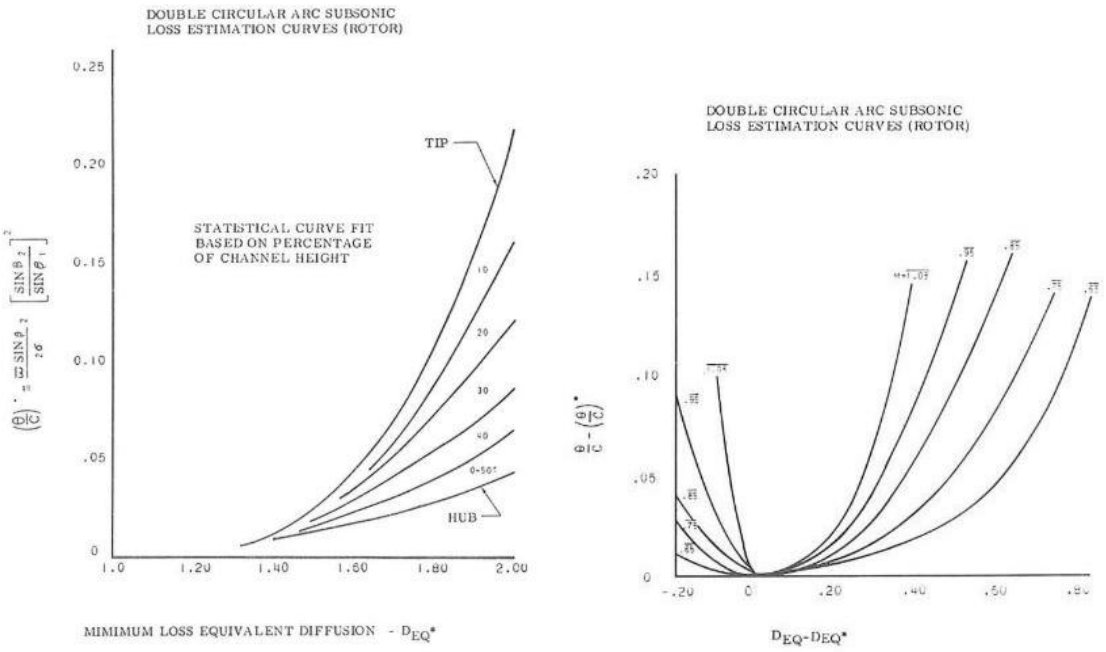

Figure 2-7: Momentum thickness parameter for minimum loss (on the left) and its correction for a diffusion factor shifted from optimal one (on the right) [19]

For the first part, the total pressure loss coefficient was defined as:

$$\bar{\omega}_T = \omega_{shock} + \omega_{viscous} + \omega_{wake} \qquad \textbf{(2-11)}$$

It is composed of three main parts: $\omega_{viscous}$ and ω_{wake}, that are the losses coming from a subsonic case, respectively from the boundary layer development and from the wake mixing, compatible with Lieblein's analysis [18], and ω_{shock} that is an estimated shock contribution to losses, considering a bow shock wave rising from the blade leading edge, solved through the appropriate theory.

The off-minimum loss is defined as a function of the equivalent diffusion factor (2-13), that can be seen as an index of the blade loading factor (Figure 2-7). It is delivering a correction of $\bar{\omega}_T$ when D_{eq} shifts from the optimal condition, considering effects like the spanwise location of the element or the inlet relative Mach number, incorporated in the coefficient K:

$$\left(\frac{\theta}{c}\right) - \left(\frac{\theta}{c}\right)^{*} = K\left(D_{eq} - D_{eq}^{*}\right)^{2} \quad \textbf{(2-12)}$$

However, for the analysis, the negative incidence range limit was established as the one in which $\bar{\omega}_{T_{off}}$ was two times the minimum loss, hence it is not wide enough to cover all the design space considered in the current project.

$$D_{eq} = \frac{V_{max}}{V_2} = \frac{V_{max}}{V_1}\frac{V_1}{V_2} \quad \textbf{(2-13)}$$

Creveling & Carmody [20]

In this research, the aim was to develop a computer program able to predict the off-design performance of a multistage axial-flow compressor. The method is based on both cascade experimental data from NACA, for the profile loss, and analytical relations, for the shock losses, from which reference values for the total pressure loss coefficient are found.

The adiabatic efficiency is calculated for each streamline by using an approach similar to Swan [19], correcting the reference values for the off-design conditions by adding a factor dependent on $\Delta i = i - i_{ref}$ and on the relative inlet Mach number (Figure 2-8), found from selected NASA data.

The reference values of incidence for the minimum loss can be obtained in different ways, such as from NASA incidence rules, from functions of the inlet flow angle and the Mach number, assuming the suction surface tangency or from tabulated input from experimental activities.

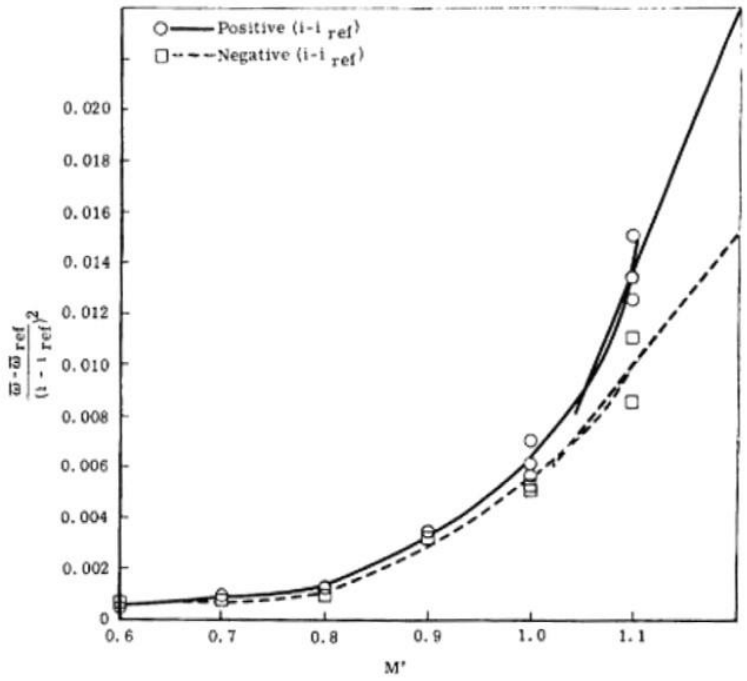

Figure 2-8: Off-minimum loss, function of Mach number and incidence [20]

Koch & Smith [21]

The aim of this research was to deliver a method for predicting the potential design point efficiency in a compressor preliminary design phase, without though considering the off-design operations. The outcome is that the design point efficiency is dependent on aerodynamical aspects, such as flow angles, blade loading and Mach and Reynolds numbers, and geometrical aspects, like the blade aspect ratio, the solidity, the tip clearances and the surface finish, as well as the presence of part-span shrouds.

The developed model is considering each source rationally and is trying to give it the right physical meaning and, where possible, instead of using empirical correlations, that can be dependent on many factors, using the fluid dynamic

theories. Nevertheless, the author is highlighting that the real flow process is “exceedingly complex” and the proposed loss elements will be oversimplified compared to those real flow features. Since some loss sources are neglected, when compared to experimental test data, the model is giving a peak potential efficiency higher than the corresponding experimental data.

The method is assuming the final compressor efficiency to be influenced by four different sources of loss: the blade profile loss, the shock loss, the end wall loss and the part-span shroud loss.

In the case of the blade profile loss, a compressible boundary layer theory is employed with the attempt to extend the 2D Lieblein’s theory[18] to the Mach number and the Reynolds numbers of interest for compressors design, considering as well the stream tube contraction due to the boundary layer growth. However, unlike in Lieblein’s theory [18], it is assumed that the boundary layer is turbulent everywhere. The laminar boundary layer regions that are present at low Reynolds numbers will be then neglected, with an overestimation of the loss.

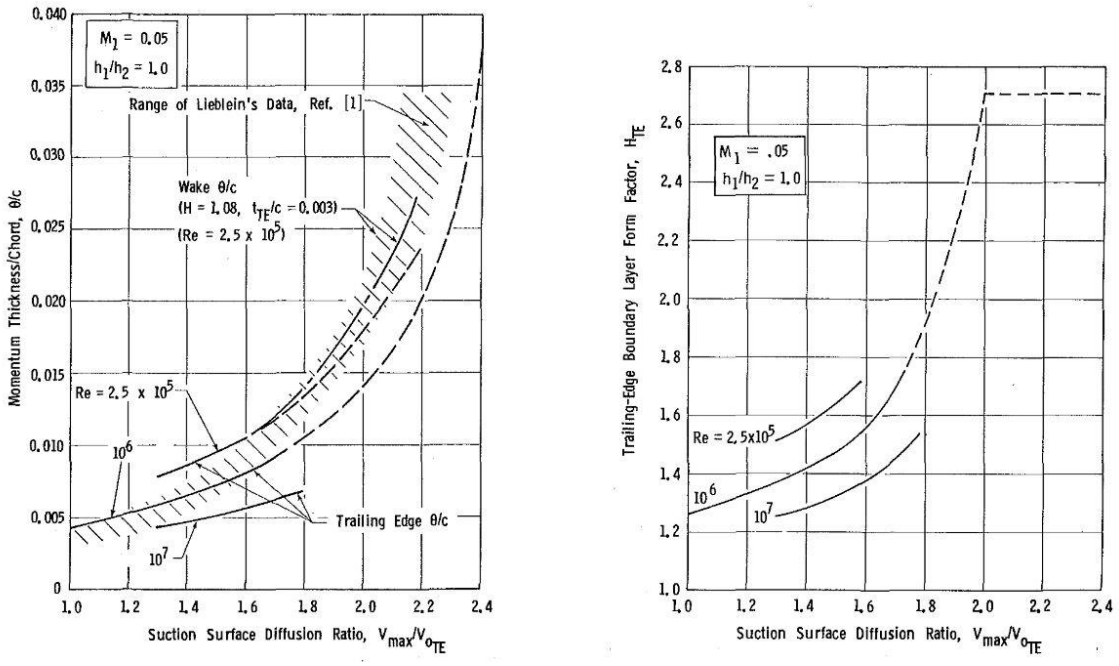

Figure 2-9: Momentum thickness (on the left) and form factor (on the right) function of the suction surface diffusion factor[21]

The data are presented in terms of momentum thickness and form factor of the boundary layer that can be then applied to (2-8) to get the corresponding loss. These quantities will be assumed as a main function of the blade diffusion factor, corrected then for the inlet Mach number effect, stream tube contraction, Reynolds number and surface finish effects.

However, the model is not giving a method to predict these quantities in off-design conditions, hence is not suitable for the current project.

Çetin et al. [22]

In this investigation, the target was to develop modified loss and deviation correlations to be applied in through-flow programs for the spanwise prediction of the flow variables in both design point condition and off-design conditions. From the flow variables, it is then possible to predict the expected overall efficiency and machine performance.

The existing loss correlations were reviewed and compared with test data coming from the NASA Lewis Test Centre and the Pratt & Whitney Aircraft Company, considering the effects of the main geometric and aerodynamic design parameters of the blades, analysing them in the whole operating range from stall to choke conditions.

The outcome is a correlation in which the design total pressure loss coefficient ω_T^* is corrected for the off-design condition with a term dependent on the deviation from the minimum loss incidence i^*(Figure 2-10):

$$\bar{\omega}_T = \omega_T^* + c_m(i - i^*)^2 \qquad \textbf{(2-14)}$$

As the minimum total pressure loss coefficient, ω_T^* is found near $i = 0°$, in a range of $\Delta i = \pm 8°$. It is suggested that the most suitable method for finding its value is the one proposed by Koch and Smith [21].The coefficient c_m will be dependent on whether the incidence is positive or negative, from the Mach number and from the type of blade profile.

However, the overall loss correlations are depending on several factors not independent from each other, hence the effects will not be linear and then not summable.

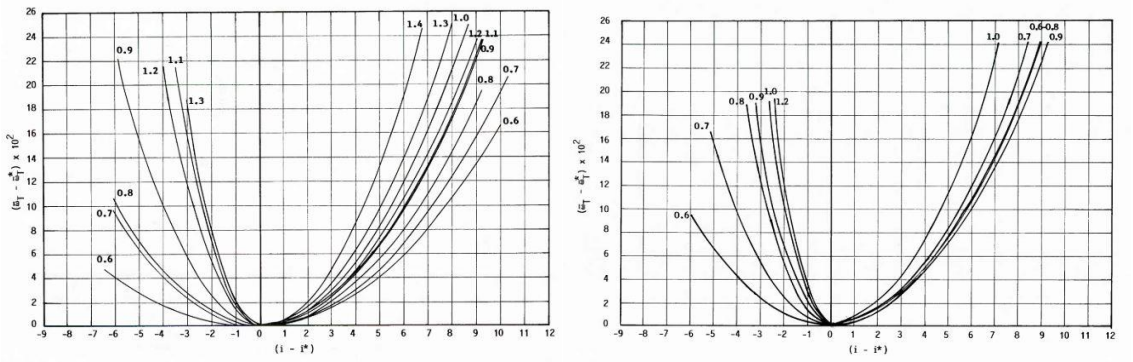

Figure 2-10: Off-design total loss deviation against incidence deviation, for MCA type blade profile (on the left) and DCA type blade profile (on the right)

Denton [15]

This analysis is not providing a method for predicting systematically the total pressure loss coefficient but is giving an overview of the loss sources in turbomachinery, trying to give a physical meaning. In order to take into account the effects of the flow characteristics and the geometry on the losses, it is suggested to have a definition of efficiency based on the flow entropy.

However, in the author opinion, it is unlikely to have an accuracy better than about $\pm 20\%$ in the loss prediction due to the high complexity and the difficult understanding of the loss phenomena. The suggestion is then to build a strong understanding of each source of loss to make qualitative improvements to new designs, and where possible make use of the available empirical and analytical correlations, although they come from oversimplified models.

König [23]

In this paper is presented a new model for the calculation of the total pressure loss coefficient based on a set of eight cascade experimental data, starting from the considerations of the previous loss models. As in Swan's model [19], the analysis is divided into two different parts, comprising the minimum loss

prediction and the off-design one, expressed in terms of wake momentum thickness and equivalent diffusion ratio. To be noticed that this model has been developed for new blading concepts used in transonic axial-flow compressors.

For the minimum losses, a set of correlations has been found, with the coefficient depending on the value of D_{eq}^* and, hence, different flow conditions on the blade:

$$\left(\frac{\theta}{c}\right)^* = a\, {D_{eq}^*}^2 + b\, D_{eq}^* + c \qquad \textbf{(2-15)}$$

For the off-design losses an approach similar to Swan's one [19] has been considered, with the equation in the same form as (2-12), with the coefficient K dependent on the inlet Mach number and on the blade shape (suction side curvature): for lower Mach number and lower camber angle, the coefficient K is decreasing.

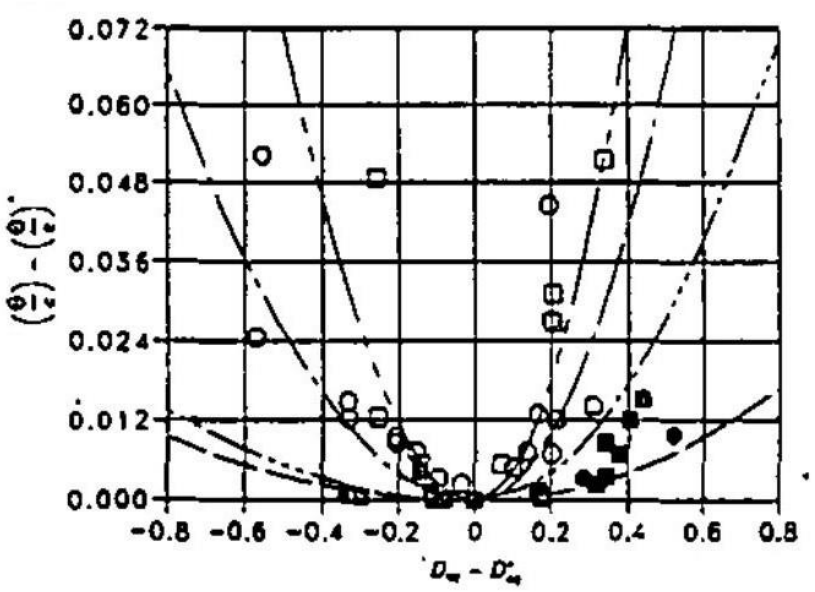

Figure 2-11: Deviation in wake momentum thickness against deviation in equivalent diffusion factor for one of the test cascade considered in König model [23]

Concluding this paragraph on total pressure loss coefficient models, it is clear that some of these methods are based on experimental results whilst some other just on analytical correlations, but each of them is taking strong assumptions or

using a limited base of experimental data. It is the author opinion that none of these models is suitable for the aim of this project since the validity range is not wide enough to cover the research range: the maximum negative incidence considered is $i \sim -20°$ (e.g. Howell [17]) whilst in sub idle conditions incidences of about $-60°$ can be reached: the model accuracy cannot be trusted anymore. Thus, there is the necessity to build a new model capable to predict with a higher fidelity the total pressure loss coefficient.

2.2.2 Deviation Angle models

When a real flow is considered, it is unlikely to have a flow exit direction parallel to the blade trailing edge one due to the boundary layer and the wake mixing effects. Hence, a deviation angle will always be present, with an outlet flow angle different from the blade one. Considering the positive values as under-turning of the flow, the deviation angle can be defined as:

$$\delta = \alpha_2 - \beta_2 \tag{2-16}$$

This parameter will be dependent on many factors and, according to Carter, they are mainly due to the blade geometry, hence camber angle (θ), solidity (σ) thickness (t) and stagger angle (γ). They define the way in which the flow is guided and, then, the characteristics of the blade boundary layer and the flow deflection.

Other factors that can influence the deviation angle are the Reynolds number, that is a measure of the turbulence level occurring in the flow, and the Mach number, that is a measure of the flow compressibility effects.

The flow deviation is an important parameter for compressor performance. In fact, as can be seen from Euler's Equation (2-2), a flow under-turning leads to a lower Δc_θ, a lower work transferred to the flow and, hence, a lower capacity to deliver the required pressure ratio. This effect will be emphasised even more considering the higher losses in off-design conditions.

As has been done for the total pressure loss coefficient, also for the deviation angle the models developed from the 50s are presented, giving an overview on how deviation angle can be modelled to be applied to the prediction of the turbomachinery performance.

Howell [17]

In this work, in order to calculate the performance of the cascade in terms of work done, it is important to define the deviation. This allows then to calculate the flow exit angle α_2 and, hence, knowing the inlet flow angle, the flow deflection.

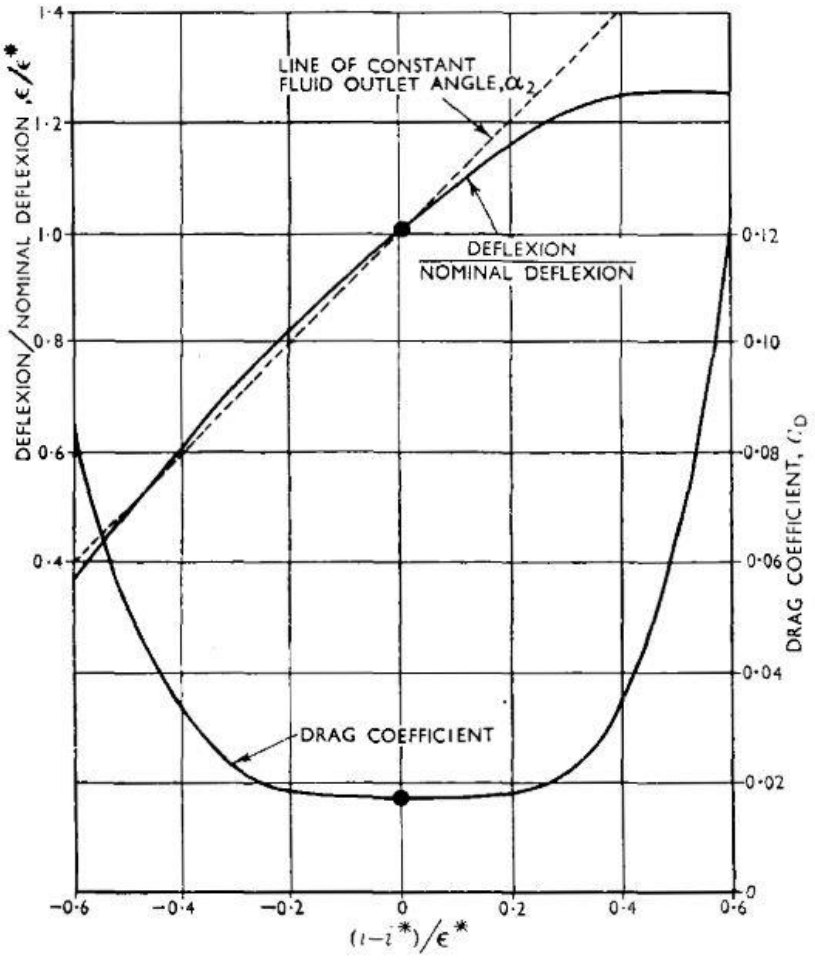

Figure 2-12: Deflection and drag coefficient for incidence shifted from optimal one [17]

This quantity will be determined through the graph in Figure 2-12, by evaluating directly the flow deflection based on the $\Delta i = i - i^*$. However, in this research a simple empirical rule for the deviation at nominal conditions is deduced from both experimental and theoretical considerations:

$$\delta^* = m\,\theta\,\sqrt{\frac{s}{c}} \tag{2-17}$$

Where m is a function of the maximum camber position and the nominal flow exit angle α_2^*.

Carter [24]

In this report, experimental data from cascade tests are analysed and, by considering the performance characteristics in both design point and off-design, the main factors influencing it are provided.

The analysis method is based on two different steps. Firstly, analytical expressions are found by considering a model constituted by only one blade, assuming the interaction of adjacent blades by replacing them with vortices concentrated at the centre of pressure of each of them. Afterwards, corrections are applied to take into account the pitch/chord ratio, the blade thickness, the stagger angle and the scale effect on the Reynolds number, basing them on empirical correlations.

The method starts by estimating the optimum incidence of the blade, defined as the one at which the maximum value of lift to drag ratio occurs, hence maximising the deflection and minimising the pressure loss. Once established this, in order to get the actual flow deflection, it is useful to estimate the flow deviation as well, assumed to be dependent on the flow around the aerofoil. The assumed relation is then:

$$\delta = m\,\theta\sqrt{\frac{s}{c}} \tag{2-18}$$

Where m is dependent on the maximum camber position and the stagger angle of the cascade. It has been observed a discrepancy of this relation with the tests due to the 3D effects of a real flow.

Lieblein [25]

In this research, a set of experimental data from test cascades has been considered, with blade profiles as NACA 65-Series and British C-4 and C-7. From a qualitative point of view, it is suggested that, since the deviation angle is an index of the cascade capacity to guide the flow, then it will be mainly dependent on the geometric cascade factors, such as the camber angle, the solidity and the stagger angle, decreasing when the solidity increases and increasing when the stagger angle increases. Moreover, for an increasing incidence angle, it has been observed that the deviation angle slightly increases as well.

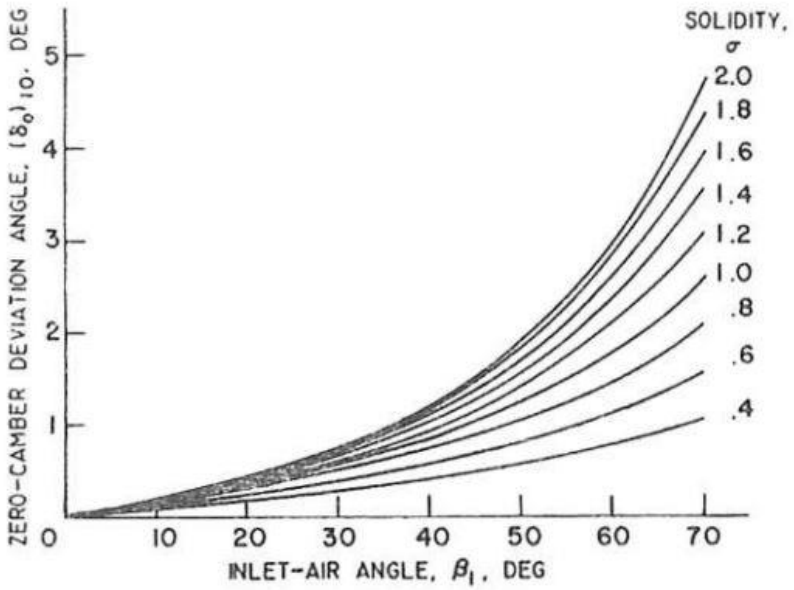

Figure 2-13: δ_0, function of inlet flow angle and solidity [25]

Trying to quantify these effects, the reference deviation at the minimum loss incidence can be defined using the following equation:

$$\delta^* = \delta_0 + \theta \frac{m_{\sigma=1}}{\sigma^b} \qquad \textbf{(2-19)}$$

Where $m_{\sigma=1}/\sigma^b$ is a term that takes into considerations the solidity effects, through its value, and the incidence angle effect through the coefficient b. The term δ_0 is the deviation angle for a zero-camber angle profile, function of the blade thickness and the blade shape, as well as solidity and inlet flow angle (Figure 2-13).

In a second phase, the effects of the incidence angle on the deviation angle were considered, developing a relationship in which the slope for deviation against incidence is a function of solidity and stagger angle, determined experimentally:

$$\delta = \delta_{ref} + \left(i - i_{ref}\right)\left(\frac{d\delta}{di}\right)_{ref} \quad \textbf{(2-20)}$$

However, this relation is valid only for regions of low loss, hence for incidence angles close to the optimal one and attached flows.

Swan [19]

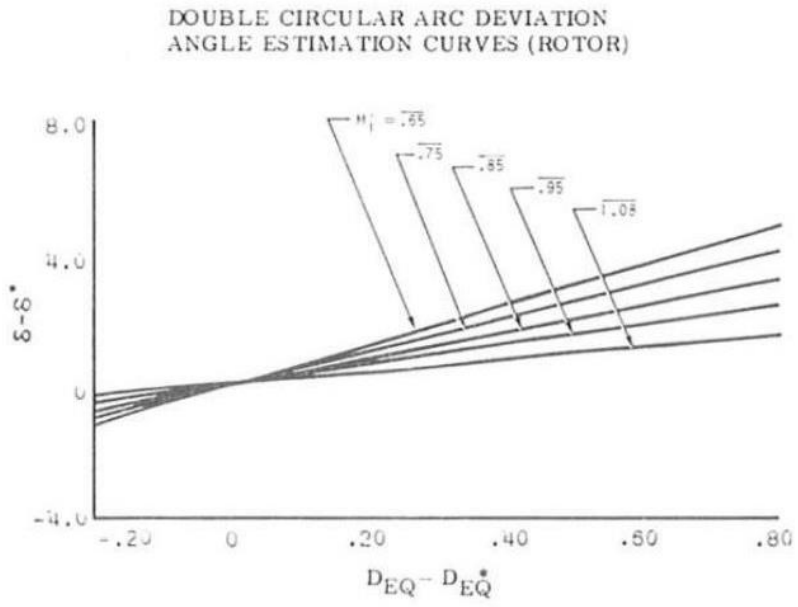

Figure 2-14: Variation of deviation angle in off-design conditions against variation of equivalent diffusion factor[19]

In this work, in order to calculate the compressor performance with the computer program developed by the author, the deviation from the optimal case is calculated throughout the following equation:

$$\delta - \delta^* = K\,(D_{eq} - D_{eq}^*) \tag{2-21}$$

Where K is a coefficient dependent on the inlet Mach number, as visible from Figure 2-14.

Creveling and Carmody [20]

In their analysis, they considered the deviation angle to be composed by two different terms: a reference deviation angle, corresponding to the reference incidence angle, found using the NASA deviation rules, and a correction for off-design conditions based on correlations of selected NASA data:

$$\delta = \delta_{ref} + \Delta\delta \tag{2-22}$$

The trend of the variation of deviation against the Δi parameter is visible in Figure 2-15, with a much higher range in the positive incidence side compared to the negative one, of interest in the current project.

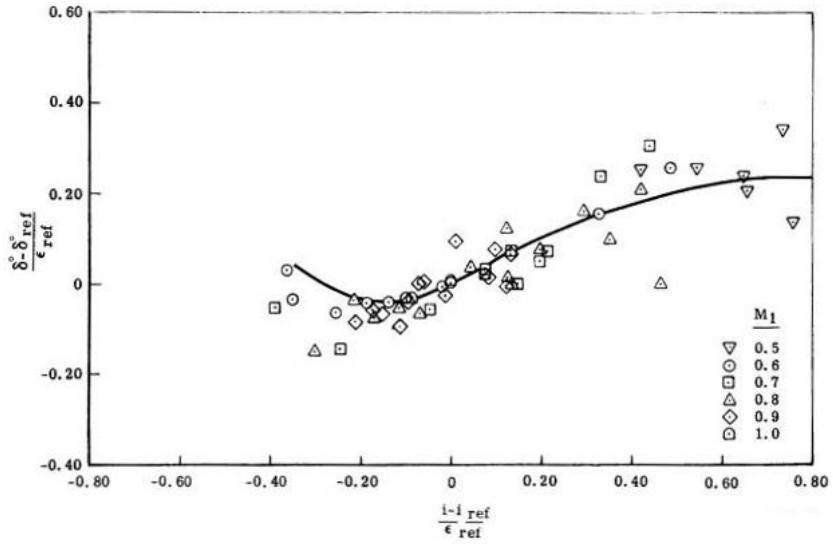

Figure 2-15: Variation of deviation from reference point against incidence variation[20]

Çetin et al. [22]

In this research, like in Creveling and Carmody's one [20], the deviation occurring in the flow is split in the reference one and in a correction due to off-design conditions. Although analysing the experimental data available it resulted that there was not really a consistent trend of the measured deviations for incidence variations, it has been decided to proceed using this model.

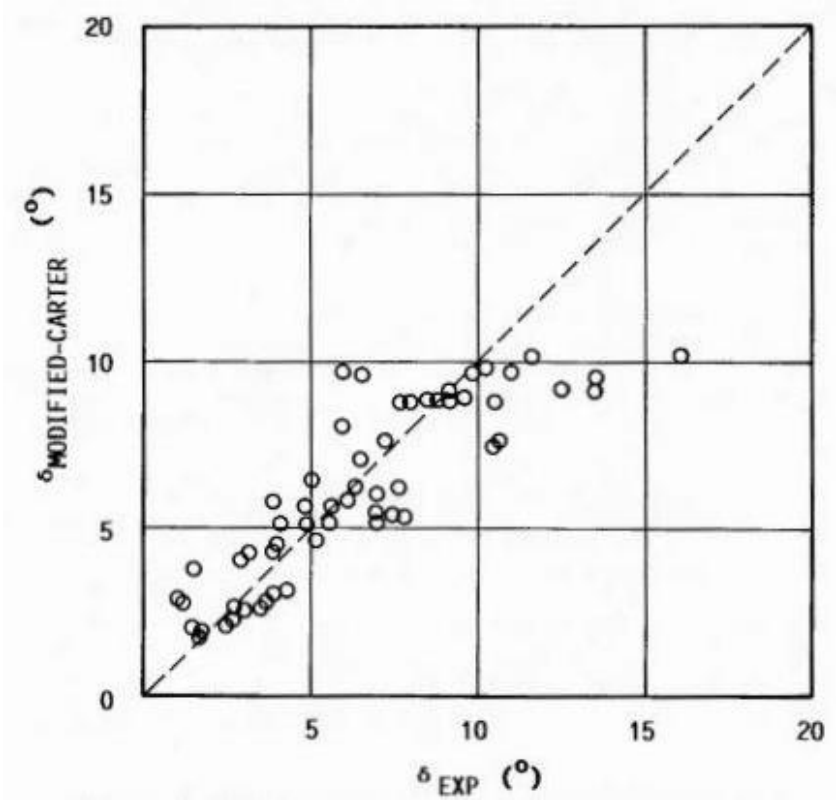

Figure 2-16: Comparison of modified Carter's model and experimental data for deviation angle[22]

The reference deviation can be calculated using a corrected Carter's rule [24], starting from the values found with that model through the Equation (2-18), defined here as δ^*_{CAR}:

$$\delta^* = -1.099379 + 3.0186\ \delta^*_{CAR} - 0.1988\ {\delta^*_{CAR}}^2 \qquad \textbf{(2-23)}$$

The needed correction can be attributed to the transonic and 3D effects present in the experimental activity. The accuracy of the correction can be appreciated in Figure 2-16, with a close trend between the two data sets.

Since the off-design data for the deviation angle were not appropriate to extract any possible consistent information, it was then decided to use the Creveling and Carmody's method [20].

In order to analyse the deviation angle, many models have been found as well. It is directly connected, through the deflection and the Euler's equation, to the power introduced by the compressor in the flow and, hence, it is an important parameter to assess the capacity to compress the flow. However, as for loss correlations, also these correlations are not accurate for high negative incidence angles and hence not suitable for sub-idle performance simulation.

Since for both the total pressure loss and the deviation angle there are not models or empirical correlations valid for high negative incidence angles, such as the ones that occur in sub-idle conditions, it is then necessary to develop more accurate correlations. In the current project, the previous work done on these models by Allegretti [8] will be carried on, extending the correlation to more blade geometries. Afterwards, their limitations will be assessed, since they are based on steady-state 2D RANS simulations and some corrections may be necessary for unsteady effects.

2.2.3 Previous work done in Cranfield University

Regarding the analysis and prediction of compressor behaviour in sub-idle conditions, a significant effort has been done in the Cranfield University UTC since the early 2000s. In fact, starting from 2003, Howard [6], Zachos [10] and Grech [5] studied these particular conditions with many different approaches, conducting to the present research project.

From the start, it was clear that the map extrapolation methods to find the compressor behaviour in the sub-idle range were not accurate enough. Hence, starting with Howard and continuing with Zachos, the approach to find the sub-

idle characteristics shifted to the interpolation methods. To be able to interpolate from the idle region towards the low shaft-speed region, a compressor line at zero-speed, also called locked-rotor speed line, is necessary. Whilst Howard used a 3D CFD approach to find it, Zachos developed a software able to compute it starting from a database of experimental results coming from a test rig in Cranfield University. The experimental results were found by Rülke [26] during her MSc thesis to validate the 3D analysis. The design space approach was similar to the one of the current project, taking multiple stagger angles, solidities and incidence angles, but considering a lower range of the parameters (e.g., $i_{min} = -60°$).

In Grech's work, the software created by Zachos has been enhanced, using both experimental and numerical data. The numerical data were coming from 3D CFD simulations, too much expensive and, hence, not suitable to cover the desired parameters range. However, a simple expression to fit the deviation angle derived with the Creveling and Carmody's correlations applied to high negative incidence flows, has been used:

$$\frac{\delta - \delta^*}{\epsilon_{ref}} = a\left(\frac{i - i^*}{\epsilon_{ref}}\right)^3 + b\left(\frac{i - i^*}{\epsilon_{ref}}\right)^2 + c\left(\frac{i - i^*}{\epsilon_{ref}}\right) + d \qquad \textbf{(2-24)}$$

Finally, the approach of the current project has been introduced by Schneider [16] and continued by Allegretti [8] in the past two years. In both the research projects the aim was to investigate the sub-idle flow behaviour by considering the dependence from the geometric and aerodynamic parameters, developing a surrogate model for the total pressure loss coefficient and the deviation angle. In order to have a wide enough database without having a too heavy computational time, a 2D CFD parametric model has been developed by Schneider.

The parameters range of Schneider's research has been then expanded in Allegretti's one, reaching the following range:

Table 2-1: Allegretti's 2D model parameters range[8]

Parameter	Lower Boundary	Upper Boundary
Stagger Angle (γ)	$15°$	$55°$
Solidity (σ)	0.5	2.5
Incidence (i)	$-90°$	$20°$
Mach Number (M)	0.04	0.3
Reynolds Number (Re)	$1 \cdot 10^4$	$1.5 \cdot 10^6$
Camber Angle (θ)	$15°$	$28°$

The data fitting has been conducted with different methods: polynomial regression, Gaussian regression and neural networks, with the latter one having the greatest accuracy. To be directly available for the computation, the correlations have been then translated in tables and implemented in the mean-line code developed by Ferrer-Vidal, considering the effects of stagger angle, solidity and incidence angle, and neglecting the effects of Reynolds and Mach number, resulted to have a negligible effect in such distorted conditions of the flow and low velocity. This code has been successfully validated against the available experimental data.

3 METHODOLOGY

In the following section, the numerical model developed to generate the database for the total pressure loss coefficient and deviation angle analysis is described. The following characteristics will be provided:

- Geometry domain
- Main geometric and aerodynamic parameters
- Mesh characteristics
- Solver set-up
- Choice of the turbulence model

Afterwards, the main process to post-process the results will be described, highlighting the main features that need to be analysed.

3.1 Numerical Model

In this section, the main characteristics of the numerical model will be presented. It has to be noticed that the model approach for the current project is the same as the two previous MSc Schneider [16] and Allegretti [8]. This choice has been made to maintain the consistency with the results obtained until now, and eventually deliver the necessary corrections to the baseline results using the same criteria.

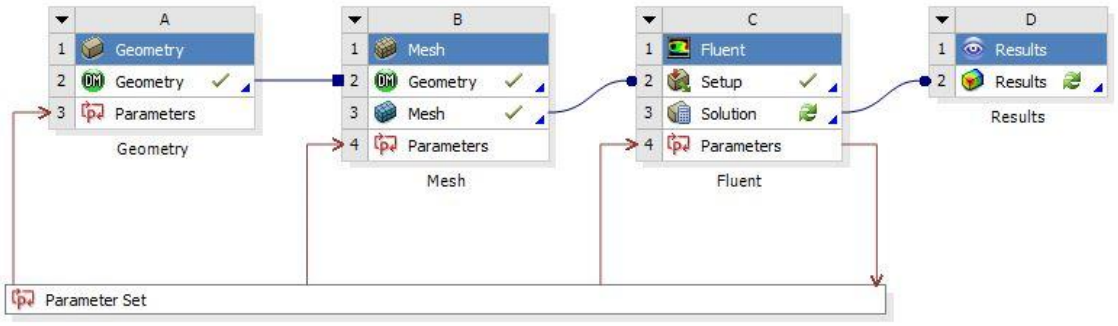

Figure 3-1: Workbench flowchart, showing the interconnections between the different tools

The decision to use a CFD model to generate the database from which derive the total pressure loss coefficient and deviation angle model comes from the lack of data in the previous experimental or CFD work on compressor performance. In fact, due to the particular conditions occurring in the sub-idle regime, its testing needs dedicated rigs and sensors that make it very expensive. Furthermore, by using a CFD model, it is possible to get the flow properties in every position without using real sensors, avoiding then the flow distortion due to their presence.

In order to do this, as in the previous years, the ANSYS Workbench software (Release 19.1) has been used. It has been chosen for its capability to have simple management of parametric studies like the current one. It allows indeed to integrate the tools necessary to proceed with a CFD analysis, such as CAD software, meshing software and Fluent. The integration of the tools in only one platform allowed to perform the parametric study by setting easily the input parameters for each case, changing geometry and boundary condition ones in a systematic way. Furthermore, it allows to define the output parameters of interest for the research.

3.1.1 Geometry

The geometry selected for the current project comes from the need to simulate parametrically through a CFD model the behaviour of a compressor blade test cascade, considering only a 2D case.

The choice to have only a 2D geometry has been made since a 3D geometry would have been too expensive to simulate the desired number of cases. Nevertheless, it must be taken into consideration that having such a simple geometry does not allow to capture totally the features of the 3D flows. However, this is an acceptable compromise considering the low computation time needed for each case and the application of the model in a mean-line performance code, that should not be affected by the end-wall and tip clearance losses. The 3D effects that occur in these conditions can be taken into consideration with a set of corrections to be applied to the final surrogate model.

3.1.1.1 Blade geometry

The blade geometries considered for the current project, as well as for the previous ones, were supplied by Rolls-Royce and are rotor blades of both an intermediate- and a high-pressure compressor of a modern multi-spool high by-pass turbofan. The choice of the blades has been done considering a reasonable range of camber angles, consistent with the modern geometries for compressor blades, described later in this section. The upper limitation for camber is in fact due to the capability of the boundary layer to remain attached with an adverse pressure gradient. With an excessively large camber angle, the pressure gradient on the suction side would be too high to have an attached flow and the losses would be too big even in a design condition.

The choice of the blades has been made by considering the blade length as well since the results should not have been affected by the other geometrical parameters of the blade.

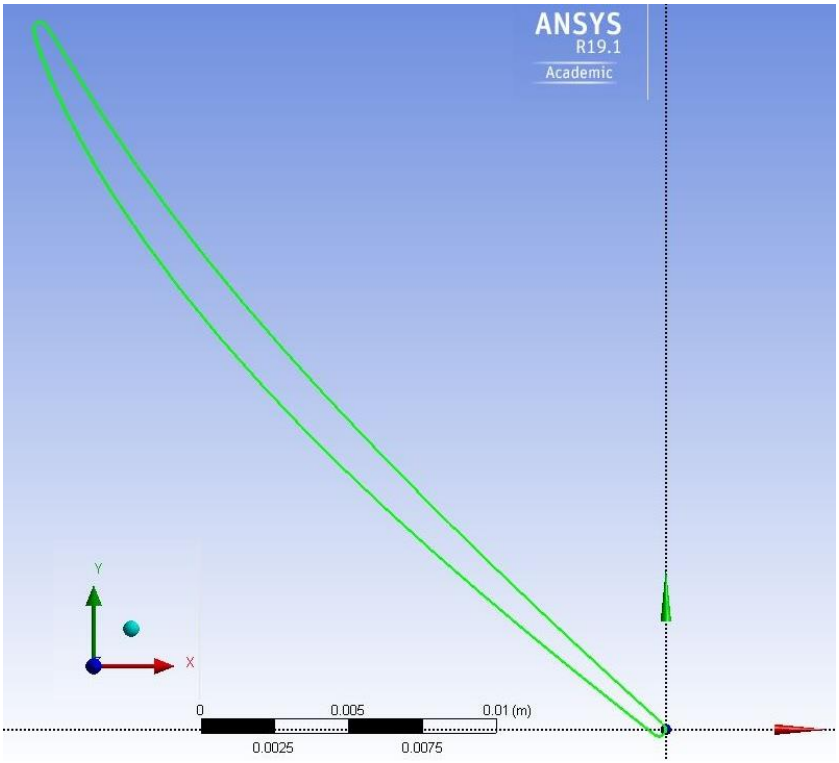

Figure 3-2: Typical compressor blade geometry

The blade definition was provided in terms of point coordinates, then connected with a spline. Attached to the blade definition file, the blade metal angles have been provided as well. The blade length and the original stagger angle of the blade were instead extrapolated from the blade geometry itself.

3.1.1.2 Domain Geometry

The geometry domain considered is representative of a compressor cascade. In order to capture the characteristics of the blade interaction, very significant in the sub-idle cases due to the high flow separation, a three blades passage has been designed. This allows, in fact, to clearly visualise the flow field between the blades and to capture the effects of their presence.

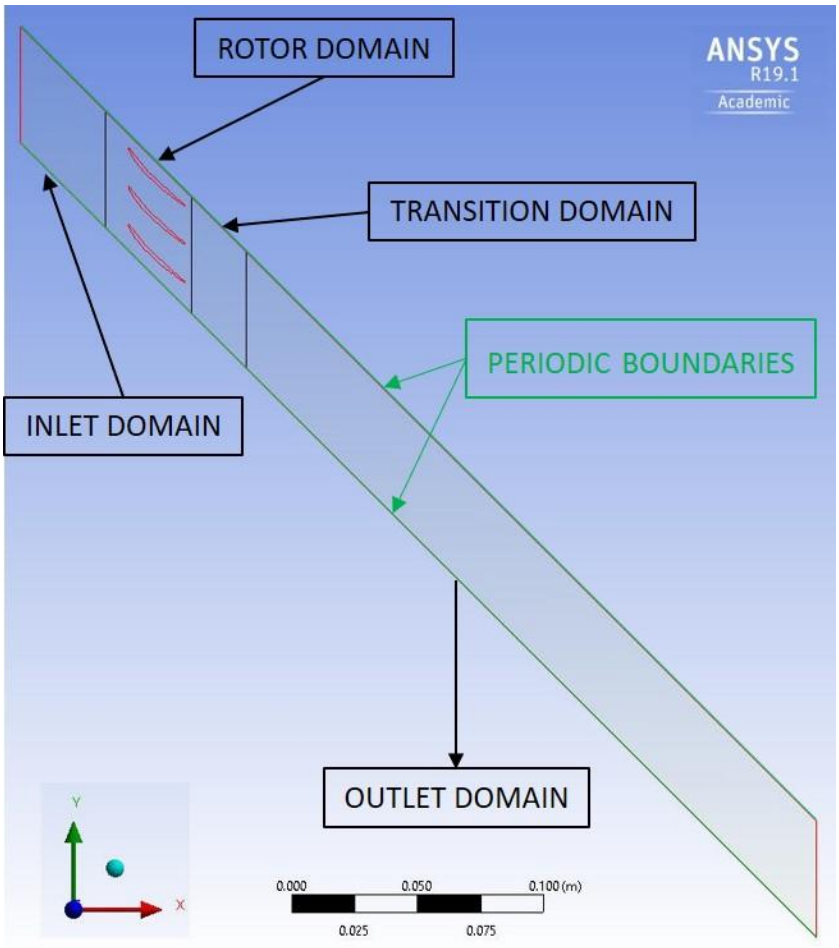

Figure 3-3: Domain geometry in ANSYS Design Modeler, with the detail of the fluid zones

The orientation of the domain has been chosen to be directed in the same direction of the blade stagger angle, one of the parameters that could be decided for each simulation case. This choice has been made in order to guarantee the flow to be directed as much as possible in the same direction as the structured mesh present in the inflation layer, avoiding numerical errors. However, it should be noticed that in sub-idle conditions it is unlikely that the flow will have this direction, especially for the very high negative incidence cases in which a big deviation is present.

The distance between the upper and the lower domain boundaries is set through the definition of the parameters in order to contain the three blades. The domain width will be then dependent on the blade chord and on the chosen solidity

The whole domain is composed of four different parts:

- *Inlet domain*: it is the zone in which the inlet boundary conditions are defined. It is set to be 1.5 chords upstream the blade leading edges, in order to guarantee that the flow is not affected by numerical issues due to the boundary condition setting.
- *Blade domain*: it is the zone that contains the blades.
- *Transition domain*: since the mesh needs to be more detailed in the blade domain, where the flow characteristics are developed, rather than in the outlet domain, where it can be coarser to limit the computational time, a zone of transition between the two different meshes is included to avoid an excess in the mesh growth rate.
- *Outlet domain*: the outlet domain is the zone in which the cascade wake is developed and where most of the losses take place. In order to model the wake mixing process and take into account for its losses, a mixed-out condition is needed in the sample location. To satisfy this requirement, the outlet boundary, where the flow is sampled, is located 10 chords downstream the trailing edge of the blades, as suggested by [27].

3.1.1.3 Geometric Parameters

As introduced before, the model geometry for the current project needed to be flexible and to provide for a wide number of parameter changes. As specified previously, the capability of ANSYS Workbench allowed to design and simulate the different geometry changes by simply changing the parameter set. Having all the tools linked, it was then easy to generate the new geometry, the new mesh and to update the new solution, starting from the former one. Here are described the geometric parameters taken into consideration:

Stagger Angle

The stagger angle is defined as the angle between the blade chord and the compressor axial direction. As the stagger angle is varying, then the blade relative position will vary, determining the variation of the throat area between the blades. A decreasing throat area will affect the flow velocity, increasing it. This implies two main effects significant for the project. The first one is on losses, since the viscous friction is directly proportional to the square of velocity: for an increasing velocity, there will be an increased value of the total pressure loss coefficient. The second one will affect the deviation angle: acquiring velocity, the flow inertia will be higher and it will have more difficulty to follow the blade shape.

Unlike the previous years, in which this parameter has been changed, in the current project it has been assumed as fixed to the value of $\gamma = 45°$ since its effects on the researched parameters were already clear.

The domain orientation has been set to vary in agreement with the stagger angle change in order to maintain the flow within the upper and lower boundaries.

Solidity

The solidity is the parameter that identifies the transversal distance between the blades. For higher solidity, the blades will be then closer to each other and the resulted flow will have a higher velocity. This will affect the total pressure loss coefficient since it is connected to the velocity of the flow. The total pressure loss coefficient will be affected as well from the wider wetted surface that the blades

will present. On the other hand, the flow will be more guided and hence will present a lower deviation, at least in conditions close to design point.

The range of solidity chosen for the current project is the following, with three values among it:

$$\sigma = [0.7, 1.4, 2.1]$$

This choice has been made since his results suggested that the solidity influence was significant just for $\sigma < 2.0$. The lower limit of solidity has been chosen since in modern compressor geometries it is unlikely to have a solidity below 1.

Camber angle

The camber angle is the main blade parameter taken into account in this project. For different camber angles, different blades will be considered. Then, for each of them, the blade geometry, and the model geometry, will change. To the change of blade will correspond not only a change in the camber but also a change in the length. Although it is suggested that this parameter is not relevant for the current purposes, the blade geometries have been chosen to have similar dimensions.

In order to explore accurately the design space, an investigation on the available blade camber angles has been conducted. It resulted that, due to the intrinsic difficulty of compressing the flow for the presence of an adverse pressure gradient on the blades and in the compressor duct, it is unlikely to have a camber angle above $30°$. In fact, as it is concluded in [28], between a camber angle of $\theta = 20°$ and $\theta = 35°$, there is a big difference in the performance of blades. It is suggested then to avoid $\theta > 30°$ to limit the total pressure losses due to separation issues. Of course, it is not recommended to have too low camber angles, since the work done on the flow would not be enough to meet the typical design requirements. As the camber angle is getting higher, we can expect a higher deviation angle due to the more aggressive blade profile that the flow cannot follow completely, but also a better capacity to compress.

Hence, four different blade geometries have been chosen for the current project. Their camber angle is listed in Table 3-1, referred to the baseline model which has the camber named θ_{bl}, the maximum value among the four available.

Table 3-1: Geometric characteristic of the four chosen blades

Blade Designation	Camber Angle [deg]	$\Delta\theta$ [deg]
IR8	$\theta_{bl} - 11.65°$	$-11.65°$
HR1	$\theta_{bl} - 8.83°$	$-8.83°$
HR6	$\theta_{bl} - 1.50°$	$-1.50°$
HR3 (Baseline)	$\theta_{bl}.$	$0°$

The HR3 blade, since is the baseline one, will be the one to which all the corrections will refer.

3.1.1.4 Aerodynamic Parameters

The main aerodynamic parameter used in this research was the flow incidence angle. As can be found in Allegretti's work, the incidence is the main parameter that affects the total pressure loss coefficient and the deviation angle, since it is the main influence on the flow field characteristics. As it is discussed later, the incidence angle will affect the width of the separation zone on the pressure side, affecting both the total pressure loss coefficient, due to the wider wake that includes a higher presence of vortices, and the deviation angle, affected by the capacity of the flow to follow the blade shape.

In the current project it has been considered the same range incidence as Allegretti's research [8]:

$$i = [-90° : 1° : 20°]$$

The incidence parameter can be set together with the inlet boundary conditions.

3.1.1.5 Boundary Conditions

The boundary conditions of the model can be set as all the other parameters through the dedicated tab in the ANSYS Workbench software. From here, all the settings will be imported to the Fluent tool.

On the upper and lower domain boundaries, the translational periodic boundary condition has been set to have the correct periodicity on the blade cascade and avoid the wall effects. The blade surface is set as a wall boundary condition, since the non-slip condition ($U_{wall} = 0$) needs to be satisfied.

Table 3-2: Inlet boundary conditions

Variable	Value	Units
Gauge Total Pressure	800000	$[Pa]$
Temperature	300	$[K]$
Flow Direction	$f\ (i)$	$[-]$
Turbulent Intensity	0.05	$[-]$
Turbulent Length Scale	$\frac{pitch_{domain}}{3}$	$[m]$

The inlet is a pressure-inlet boundary condition, with the possibility to set the Gauge Total Pressure and the flow direction, having a homogeneous condition. The turbulence properties were specified through the Intensity and Length Scale method. The quantities are specified in Table 3-2.

The outlet is a pressure-outlet boundary condition, in which the static pressure is set and the Target Mass Flow Rate option is enabled. The solver will then attempt to reach the targeted mass flow rate, calculated from a non-dimensional mass flow rate set in the workbench parameters set. In this way, the outlet total pressure will be set to reach the target mass flow and the total pressure loss coefficient will be calculated from the resulting total pressure drop. The values are specified in Table 3-3.

Table 3-3: Outlet boundary conditions

Variable	Value	Units
Gauge Static Pressure	101325	$[Pa]$
Temperature	300	$[K]$
Target Mass Flow Rate [m/s]	$f\ (i)$	$[-]$
Turbulent Intensity	0.05	$[-]$
Turbulent Length Scale	$\frac{pitch_{domain}}{3}$	$[m]$

All the pressure conditions were referred to the Reference Pressure of $p = 0\ Pa$. The non-dimensional mass flow through which the Output Target Mass Flow Rate has been calculated was kept constant to the value of:

$$FlowFunction = \frac{W\sqrt{RT}}{PA} = 0.1$$

3.1.2 Meshing

The meshing of the CFD geometry has been performed with ANSYS Meshing, since it is suitable to be integrated with the Workbench tool, allowing the importation of the desired parameters, such as the first cell height of the inflation layer to control the y^+ value on the blade walls.

3.1.2.1 Mesh Topology

The mesh topology decided for the current model is an unstructured mesh in the whole domain, except for the region near the blade walls in which a structured one is implemented in order to capture properly the boundary layer characteristics. The choice of building an unstructured mesh comes from the numerical issue that can arise when the flow is not directed in the same direction as the cells. Hence, since the flow direction can be very different depending on the flow incidence set in the boundary conditions, the mesh is built with the All

Triangles Method [29]. Moreover, an unstructured mesh is suitable for the frequent changes in the model geometry necessary to explore the whole design space, as described in the parameters section.

The mesh size is different depending on the considered domain zone:

- In the inlet and blade domain, the mesh size is reduced since it is useful to model the flow in the most accurate way and to avoid a too rough transition from the wall inflation layer to the freestream mesh.
- In the outlet domain, the mesh size is around 70% higher since the flow field does not need to be modelled in extreme details as near the blades. However, it cannot be too big since the mixing phenomena need to be modelled as well in this zone.
- On the blade walls, the boundary layer needs to be modelled, hence a structured mesh is used in this region to avoid the numerical errors that can arise from the flow directed in a direction different from the cells one.

3.1.2.2 Mesh Quality

An important issue when it comes to deal with CFD modelling is the quality of the mesh. In order to guarantee reliable and accurate results, it is crucial to have a good quality mesh to avoid the onset of numerical diffusion. The overall quality of the mesh (Figure 3-4a) can be assessed basing the judgement on the recommended value for ANSYS Fluent [30]. In the following, the definition of the main factors:

- **Orthogonal quality**: it is a numerical index of the cell quality that considers the relationships between a vector orthogonal to the cell's surface and the vectors pointing from each cell's central point towards the cell's faces or other cell's central points. In order to have a good quality, it is recommended to have a value as close to 1 as possible and not lower than 0.01. For the current case, most of the elements have a value above 0.95 and, overall, no more than 0.30, as visible in Figure 3-4b.
- **Aspect ratio**: it is a measure of the cell's stretching in one direction. It is recommended to have aspect ratios as close to 1 as possible, hence to

have more square cells as possible. The presence of high values of aspect ratio is only acceptable in case the flow has a strong prevalent direction, aligned to the cell's direction, as it happens in the inflation layers near the walls. Moreover, quick changes in its value between adjacent cells is not advisable. In the current case, although some cells present high values of aspect ratio, as shown in Figure 3-4c the majority has a value below 100, that is the recommended value.

- **Skewness**: the mesh skewness is a measure for the cell deformation. High values of skewness, hence close to 1, are not recommended since they can introduce instabilities in the convergence behaviour and in the solution accuracy. In the current model, a value below 0.1 for most of the cells has been achieved, as shown in Figure 3-4d.
- **Smoothness**: it is important for a good quality mesh to avoid sudden changes in the cells' size and, hence, to have gradual changes between the regions with a different mesh size. Having an unstructured mesh is helping to avoid this issue. However, a mesh transition zone has been added between the blade and the outlet domains to allow the meshing software to create a smoother transition.

Finally, it is important to limit the presence of sharp changes in the mesh cells. It is then advisable to check the mesh near the leading and trailing edges of the blades to avoid rough changing in the mesh around them.

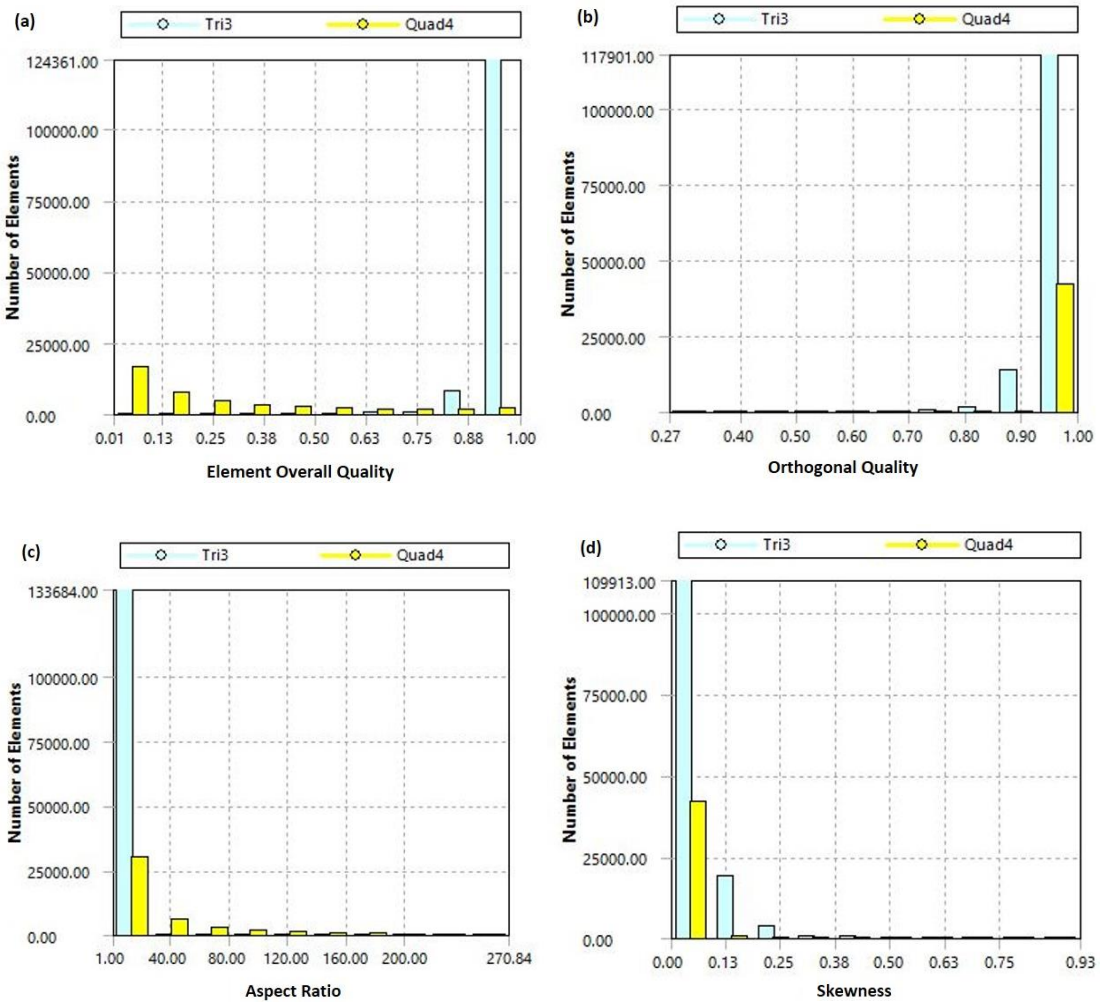

Figure 3-4: Mesh quality metrics: (a) Overall Quality, (b) Orthogonal quality, (c) Aspect Ratio and (d) Skewness

3.1.2.3 Y+ Distribution

In order to model the boundary layer, it is important to capture its properties in the most accurate way possible. In order to do this, it is useful to define the capacity of the solver to handle the boundary layer through the wall y^+, hence the non-dimensional value of the first cell layer height from the blade wall. For the CFD analysis, it is defined as [31]:

$$y^+ = \frac{U_\tau \, y}{\nu} = \frac{\rho \, U_\tau \, y}{\mu} \qquad \textbf{(3-1)}$$

Where $U_\tau = \sqrt{\tau_w/\rho}$ is the boundary layer stress velocity. The wall stress can be then defined as:

$$\tau_w = \frac{1}{2} c_f \rho U_\infty^2 \tag{3-2}$$

In which the friction coefficient can be calculated, assuming a turbulent boundary layer, as $c_f = 0.027\, Re^{-\frac{1}{7}}$.

In the RANS k-ω SST turbulence model, there are two different approaches that can be used to model the boundary layer, with two different y^+ requirements [31]. In the first case, which requires $30 < y^+ < 300$, the velocity profile of the viscous sub-layer can be assumed as given by a wall-function. In the second case, which requires $y^+ \leq 1$, the viscous sub-layer will be solved. For the current model, the second approach has been chosen, hence the requirement for the mesh is $y^+ \leq 1$.

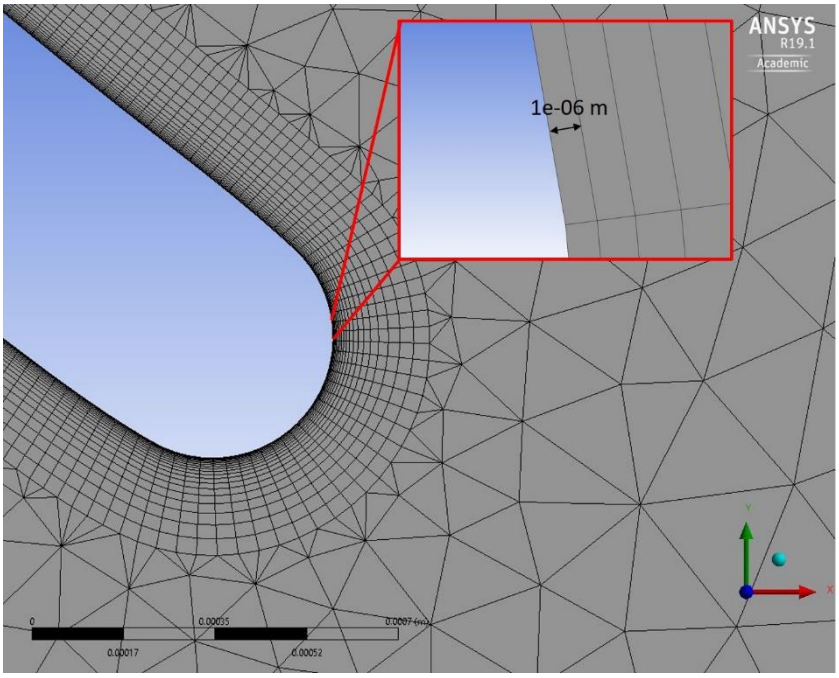

Figure 3-5: Inflation layer on the blade walls

Following the preliminary definition of Equation (3-1) and checking the actual y^+ value on the blade walls, a value of the first cell height of $h_{wall} = 1 \cdot 10^{-6}\, m$ has

been selected (Figure 3-5), with a growth ratio of 1.2. All over the blade surface and for all the four geometries, a $y^+ \leq 1$ is registered. In Figure 3-6 is shown the y^+ distribution of the HR6 geometry for $i = -82°$, hence with the highest possible velocity. Just on the leading edge it is slightly above 1, but this is an acceptable value considered the flow characteristics in this point.

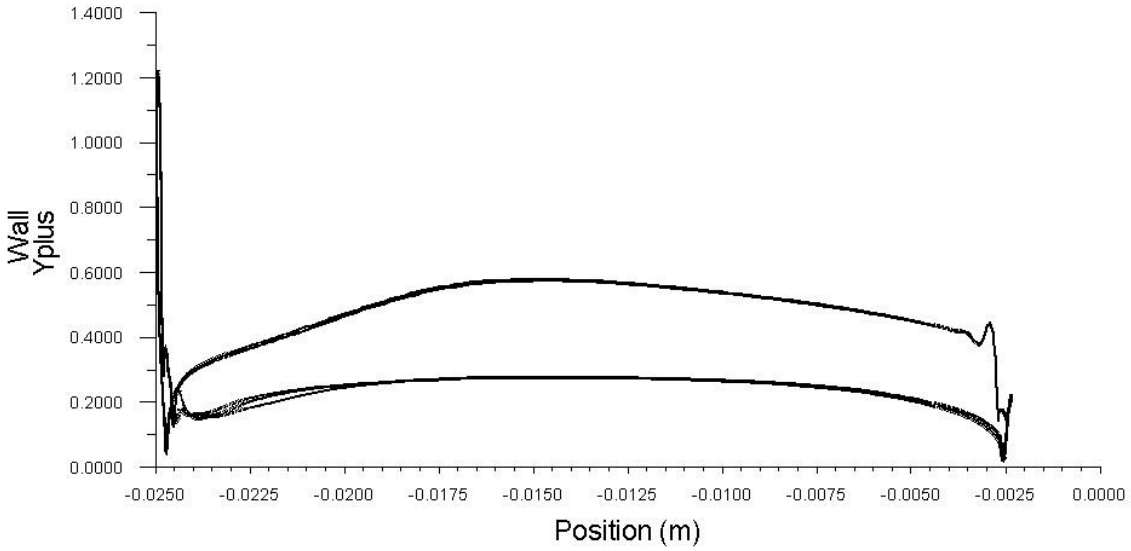

Figure 3-6: y^+ distribution along the blade surface

3.1.2.4 Mesh Sensitivity Study

When a CFD model is built, a mesh sensitivity study is needed to check whether the solution is depending on the mesh or not. Of course, in a CFD model, the continuous fluid domain is discretised in a grid, which density should not affect the effective solution. In the case this happens, the mesh size should be reduced in order to avoid this effect. However, it is important to optimise its density since the mesh should be fine enough to avoid the dependency of the results from it, but not too fine to avoid a useless computational effort, that is giving the same result as a coarser mesh.

In order to perform the mesh sensitivity study, a single geometry has been chosen and tested. This choice has been made to avoid the repetition of the study for the four different geometries. The reason for which this is possible is that all the four blades have a similar geometry, thickness and angles and, hence, it is possible

to apply this. For the study, the HR6 blade with the solidity $\sigma = 2.1$ has been chosen since it is the one with the lowest length and, hence, with the lowest Reynolds number. In fact, for this characteristic, this is the one that more can be affected by the mesh size since the flow will be more subjected to viscous effects rather than inertial ones. Nonetheless, all the flow structures, like the wake and the vortices, will be rising from the blade geometry and, hence, their size will be proportional to the characteristic dimension of the geometry, that for this case will be the blade leading edge.

To perform the study, three different independent flow variables have been taken into consideration: the inlet flow velocity, the deflection angle and the total pressure loss coefficient, that are also the variables in which the research is focused. To consider the number of elements, in order to have a good range of values, three different meshes have been selected, each with the double of the "linear nodes" of the previous one. As number of "linear nodes", since it is a 2D case, has been considered the square root of the total number of nodes. The values of the three different meshes are presented in Table 3-4.

Table 3-4: Mesh sensitivity study results

#Nodes	#Linear Nodes	ω $[-]$	ϵ $[deg]$	V_{in} $[m/s]$	#Iterations	Wall-time [s]
23362	153	1.8229	47.379	121.35	627	26.8
76348	276	1.8762	47.543	120.91	637	113.5
219092	468	1.8762	47.543	120.91	1243	867.8

The results are then shown in Figure 3-7. As it is clear, above the number of nodes of the second mesh they are not changing anymore. Hence, above this value, the results are independent from the mesh density.

For the project, a mesh of around 110000 nodes has been used for each geometry since, although a slightly higher computational effort, a safe margin due to the changing geometry has been used.

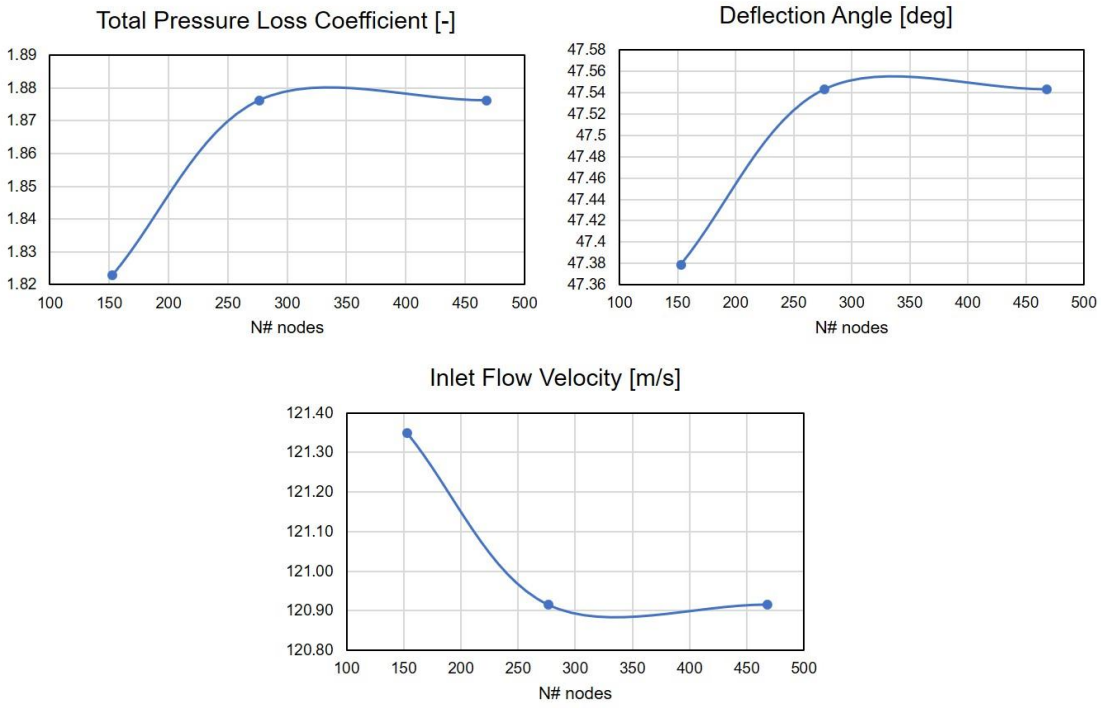

Figure 3-7: Mesh sensitivity study results

3.1.3 Solver Set-up

Since the model has been run for both steady-state and unsteady-state cases, the solver used for the solution, as well as the solution methods and controls, will be dependent on the particular case. The turbulent model will be changed as well between the two approaches to the simulations, as explained in the next section. However, the mesh will not need to change since the two considered turbulence models are deriving from the same two equations approach, with a similar method to deal with the turbulence.

Here are briefly described the fluid properties chosen for the considered model

3.1.3.1 Fluid Properties

For the current model, an incompressible fluid has been chosen. This is possible since testing the model with a compressible fluid, it resulted to have a maximum Mach number of about 0.16 (Figure 3-8). Thus, an incompressible flow can be assumed without having excessive errors. This choice is supported by the

previous work as well, which demonstrated that there is no difference between the two approaches. Moreover, a separate Mach number correction was created using compressible models but, due to the low Mach numbers encountered in typical sub-idle conditions, it was deemed to have a negligible effect on the final correlations. The assumed flow properties are listed in Table 3-5.

Table 3-5: Flow properties

Property	Value	Units
Gas Model	$Incompressible$	$[-]$
Density	1.225	$[kg/m^3]$
Specific Heat	1006.43	$[J/kg\ K]$
Thermal Conductivity	0.0242	$[W/m\ K]$
Viscosity	$Sutherland\ Law$ $(Three\ Coefficient\ Method)$	$[kg/m\ s]$

As it is described in Allegretti's thesis [8], the validation of the model has been performed comparing the data to Lieblein's [25] and Howell's [17] work based on experimental data. It will be furthermore validated in the final stage since it is implemented in the mean-line code developed by Luis Ferrer-Vidal and compared to the experimental results of the compressor test rig run in Cranfield University for these purposes.

The validation resulted in a slight difference from the values of the current model to the ones cited before. It is thought that the discrepancy in the dataset can be due to the different geometry of the blades: the ones of Lieblein's and Howell's studies are from the 50s and 60s, while for the current geometry they come from a modern engine, in which a better understanding of the flow is reached. Despite this difference, the current model can be considered accurate enough. Moreover, the validation of the mean line code against the experimental data is successful.

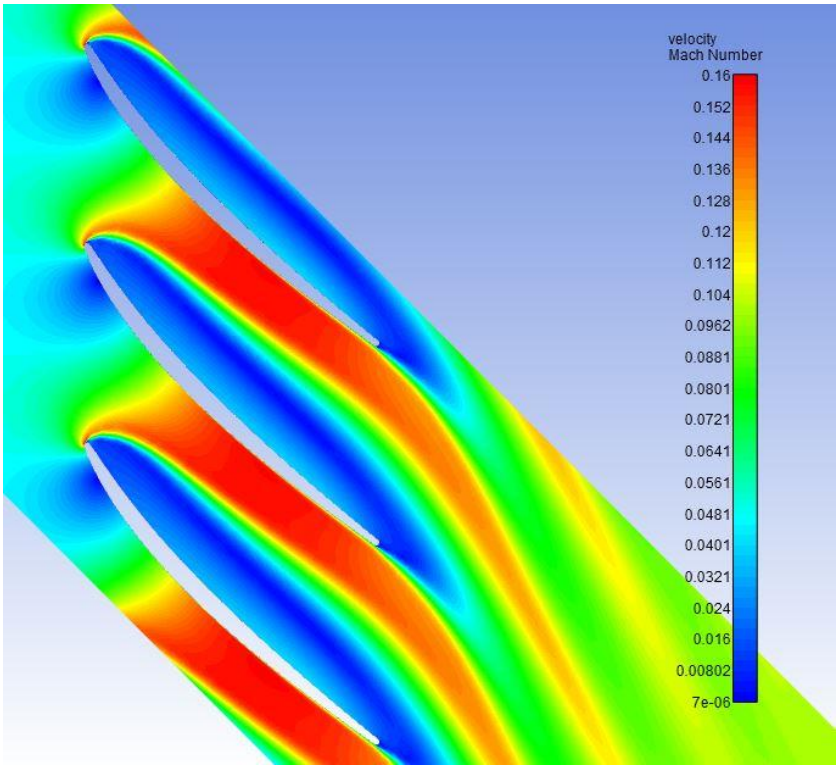

Figure 3-8: Mach number contour in case of compressible flow

3.1.4 Turbulence Model

As any other flow occurring in nature, a high level of turbulence will be present in the current flow field. As shown in Camp's research [32], usually the level of turbulence, defined in Equation (3-3), will be between 6% and 8%. Hence, as specified in the boundary conditions, an inlet one of 5% has been assumed.

$$I = \frac{u'}{u_{avg}} \tag{3-3}$$

At low incidence, for an unseparated flow, the boundary layer will be present and eventually, it will always end in turbulent structures. The wake will be present as well, with the characteristic mixing between the pressure and suction side flows taking place. Moreover, considering separated flows, such as the ones occurring at high negative incidence, a wide separation zone will be present, bringing to further turbulence structures such as recirculation and vortices. In order to solve these flow characteristics, the turbulence needs to be modelled in the most

accurate way possible. Nonetheless, each method needs to take into consideration the computational effort necessary to solve the desired structures. Because of this, not all the length scales can be solved through the flow equations and, from a certain size downwards, the behaviour needs to be modelled to avoid infinite computational time.

Indeed, the stochastic characteristic of these phenomena and the high non-linearity of the process make it very difficult to model and predict it. It is then impossible to have a deterministic approach to turbulent flows, and since now what has been tried is to develop the most accurate possible statistical description to capture the overall effects of the turbulence on the flow.

The turbulence can be then considered as the superimposition of multiple sizes of fluctuating swirling structures, called eddies. Their size starts from the characteristic dimensions of the considered geometry and, through the vortex stretching, it is brought down to the smallest scales, close to the molecular dimension. The largest eddies are responsible for the introduction of the kinetic energy from the streamflow to the turbulent structures. Then, in a process called energy cascade decay, the turbulent kinetic energy is redistributed to the smaller scales. In this process, since the vorticity of an incompressible flow will be constant, and the size of the eddies is reducing, the velocity gradient will continuously increase. Close to the molecular scales, it will be such high that the viscous shear stress dissipates the kinetic energy of the fluid into heat (Figure 3-9), with a high level of diffusivity. The energy introduced and the one dissipated will be in equilibrium, with the need for modelling additional shear stresses (the Reynolds ones) to control it.

As it is known, the entity with which the energy is redistributed among the vortices will be express with the power-law described in Equation (3-4), in which κ is the wavelength. As it is plotted in a logarithmic graph, it will be a line with the slope coefficient of $-5/3$ (Figure 3-10).

$$E(\kappa) \propto \kappa^{-\frac{5}{3}} \quad \textbf{(3-4)}$$

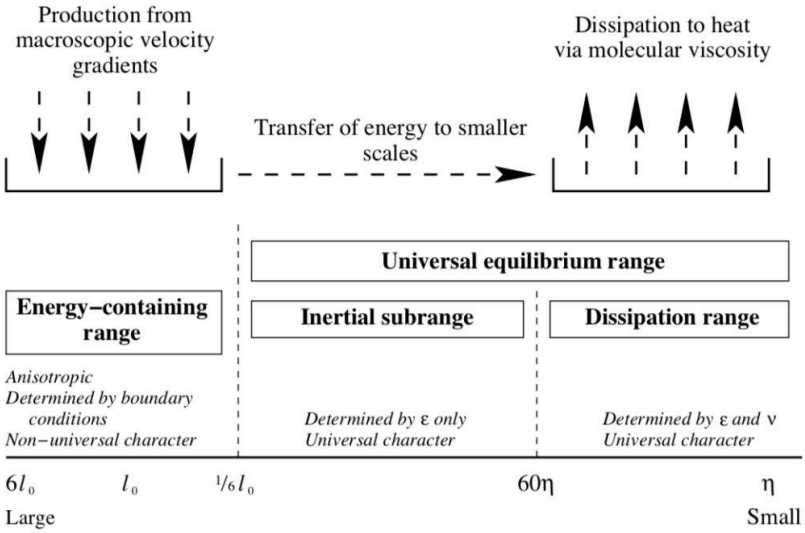

Figure 3-9: Schematic of the length scales involved in turbulence, with the physical processes dominant in each range [33]

In order to model the flow through the numerical analysis, as it happens for a CFD simulation, the Navier-Stokes equations are used. In a general 3D case, there will be one mass conservation equation, three momentum conservation equations, specified in the three directions, and one energy equation, neglected in case of isothermal flow. In the current case, since a 2D geometry and an isothermal case is considered, there will be three equations: one for the mass flow and two for the momentum, in the x- and y- directions.

The analytical solution for these equations can be found only for flows which allow strong assumptions. In real cases, due to the high non-linearity of the equations, an analytical solution cannot be found. Instead, the expedient in these cases is to discretise the problem with the finite volume approach, bringing the partial differential equations to assume an algebraic form that can be solved iteratively. This is done in ANSYS Fluent through the creation of the grid, or mesh, based on the geometry shape.

The discretisation and turbulence modelling process can be done in multiple ways. The less computationally expensive, but also less accurate, is the RANS approach, that will be described further later. The SAS, i.e. Scale-Adaptive

Simulation, is as well based on the RANS approach but it can consider a slightly wider turbulence length scale range, giving higher accuracy with a computational effort higher but still acceptable. The further approaches, like the DES, LES and DNS, can solve the turbulence in much smaller length scales, giving high accuracy. However, they are much more expensive and will not be considered in the current project. Hence, the approaches analysed will be the steady-state RANS one and the URANS one, in both regular and SAS versions.

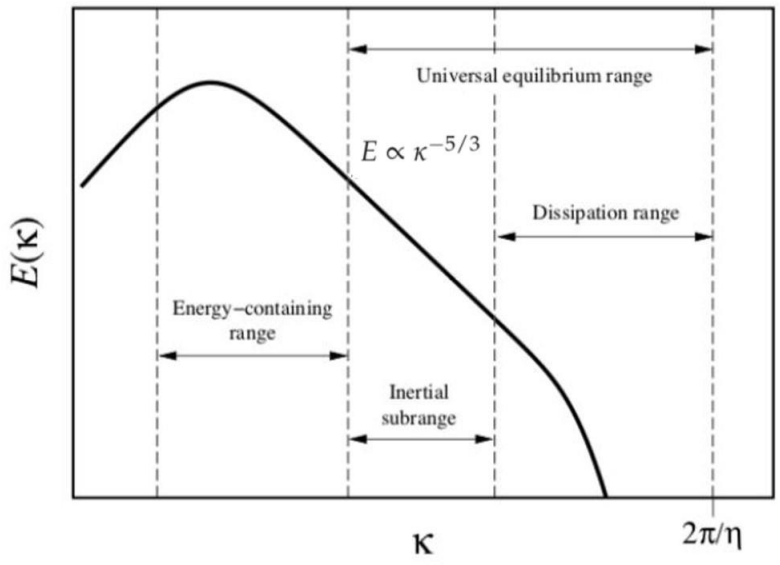

Figure 3-10: Energy cascade spectrum [33]

These approaches, for both steady and unsteady simulations, are based on the consideration that the flow, since it follows stochastic processes, cannot be deterministic and can only be handled through the statistical analysis. In order to implement this, the physical quantities are decomposed in an averaged component, that is the one that gives the characteristics of the general flow field, and a fluctuating component, that contains all the perturbations present in the flow due to turbulence:

$$f(\boldsymbol{x}, t) = \bar{F}(\boldsymbol{x}) + f'(\boldsymbol{x}, t) \qquad \textbf{(3-5)}$$

With f as the generic flow property. The effect of the turbulence, hence the nonlinearity of the equations, on the large-scale motion can be then modelled

through f'. After the decomposition, the equations are averaged in both space and time, in case of steady flow, or just in space, in case of unsteady flow assumption [34].

Considering the incompressible flow assumption as well, the resulting equations are the following, with both the mean and fluctuating terms [35]:

$$\frac{\partial \rho}{\partial t} + \frac{\partial}{\partial x_i}(\rho \bar{u}_i) = 0 \tag{3-6}$$

$$\frac{\partial}{\partial t}(\rho \bar{u}_i) + \frac{\partial}{\partial x_i}(\rho \bar{u}_i \bar{u}_j) = -\frac{\partial \bar{p}}{\partial x_i} + \frac{\partial}{\partial x_j}(\bar{\tau}_{ij}) - \frac{\partial}{\partial x_j}(\rho \overline{u_i' u_j'}) \tag{3-7}$$

Where $\bar{\tau}_{ij}$ is the viscous stress tensor, which for a Newtonian fluid has the form:

$$\bar{\tau}_{ij} = \mu \left(\frac{\partial \bar{u}_i}{\partial x_j} + \frac{\partial \bar{u}_j}{\partial x_i} - \frac{2}{3} \delta_{\mathrm{ij}} \frac{\partial \bar{u}_k}{\partial x_k} \right) \tag{3-8}$$

The effect of the turbulent fluctuations on the main flow properties is then described from the Reynolds stress tensor $\rho \overline{u_i' u_j'}$. Using the Boussinesq's approach, in which this term is related to the mean velocity gradients, it can be defined as:

$$\tau_{ij}^{RS} = -\frac{\partial}{\partial x_j}(\rho \overline{u_i' u_j'}) = \mu_t \left(\frac{\partial \bar{u}_i}{\partial x_j} + \frac{\partial \bar{u}_j}{\partial x_i} \right) - \frac{2}{3} \left(\rho k + \mu_t \frac{\partial \bar{u}_k}{\partial x_k} \right) \delta_{\mathrm{ij}} \tag{3-9}$$

In which are contained a term connected to the eddy or turbulent viscosity (μ_t) and another one connected to the turbulent kinetic energy (k). The way in which these two terms are determined to close the system of equations will be dependent on the chosen turbulence model. For the current case, the models used are based on two-equations: one to model the turbulent kinetic energy transport (then, the k equation) and one to model the energy dissipation term, in which can be used the turbulent dissipation rate (then, the ϵ equation) or the specific dissipation rate (then, the ω equation).

For the steady-state flow assumption, the solution will not be dependent on the time and, hence, the time derivatives will be null.

3.1.4.1 Steady-State Analysis

For the steady-state case, the RANS k-ω SST (i.e. Shear Stress Transport) model has been chosen. This choice has been made since, as supported by Zachos [36] experimental results, this model was the most accurate for predicting the flows through a compressor cascade. This model was developed by Menter [37] in 1994 to merge the capabilities of two main models:

- The k- ω model, that is more performing in the viscous sub-layer and log-layer, but can be too sensitive in the freestream flow, leading to numerical instabilities, and will be then used close to the walls;
- The k-ε model, that is less sensible, and then more stable, in the freestream region, but also less accurate in the boundary layer, that will be used for the freestream region.

The switching of the two models is controlled by a blending function within the energy dissipation equation. In this way, it will be more able to correctly predict the separation point, as it is demonstrated by Zachos [36].

In the following, the settings of the solver for this model are specified, providing the sensitivity studies that led to these choices. The studies have been conducted on the same geometry of the mesh sensitivity study, hence the HR6 one.

Iterative Convergence Residual Sensitivity Study

In Fluent, the convergence of the solution can be controlled by checking both the iterative convergence residuals and the solution monitors. For the first case, a check on the level of accuracy for each value of the residuals is needed in order to choose the right ones to have a completely converged solution with the lowest possible computational time. Since the continuity residual, related to the mass-flow rate, was the one with the more difficult convergence, the check is done on its value. Three output parameters have been chosen to proceed: the total pressure loss coefficient, the deflection angle and the inlet velocity.

As it can be visible in Figure 3-11, for the residual value below $1e-04$ the results are not changing anymore. Hence, this value has been set for the continuity

residual, as specified in the solution controls section. The behaviour on the main residuals is shown in Figure 3-12 and, as it is visible, all the other are well below the continuity one. The convergence is reached for around 350 iterations.

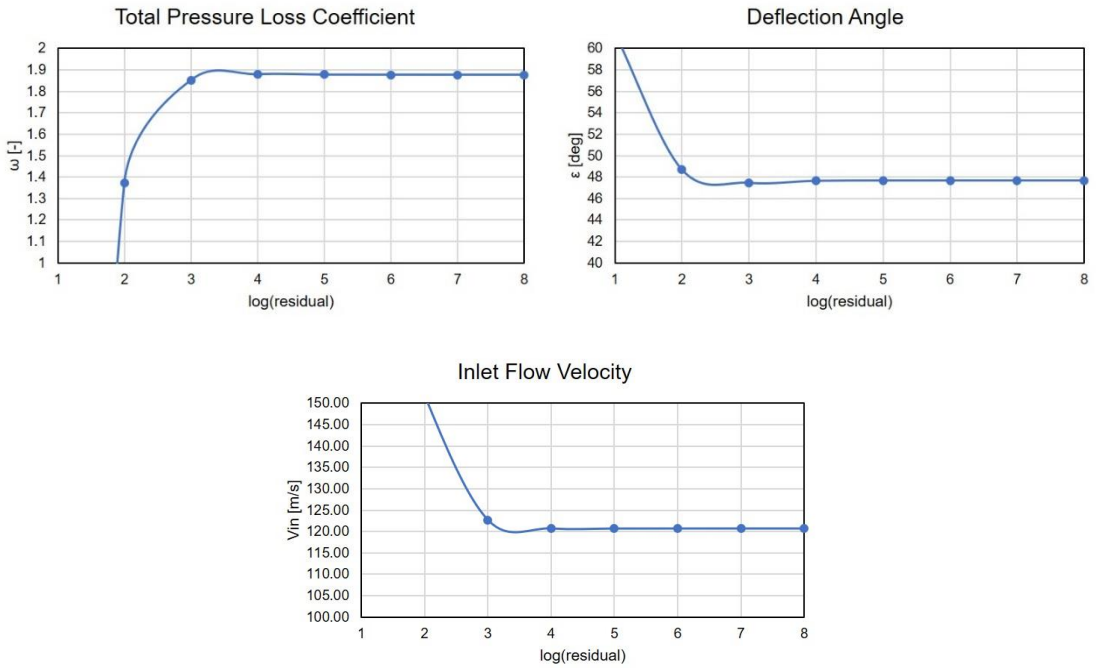

Figure 3-11: Results for the iterative convergence residual sensitivity study

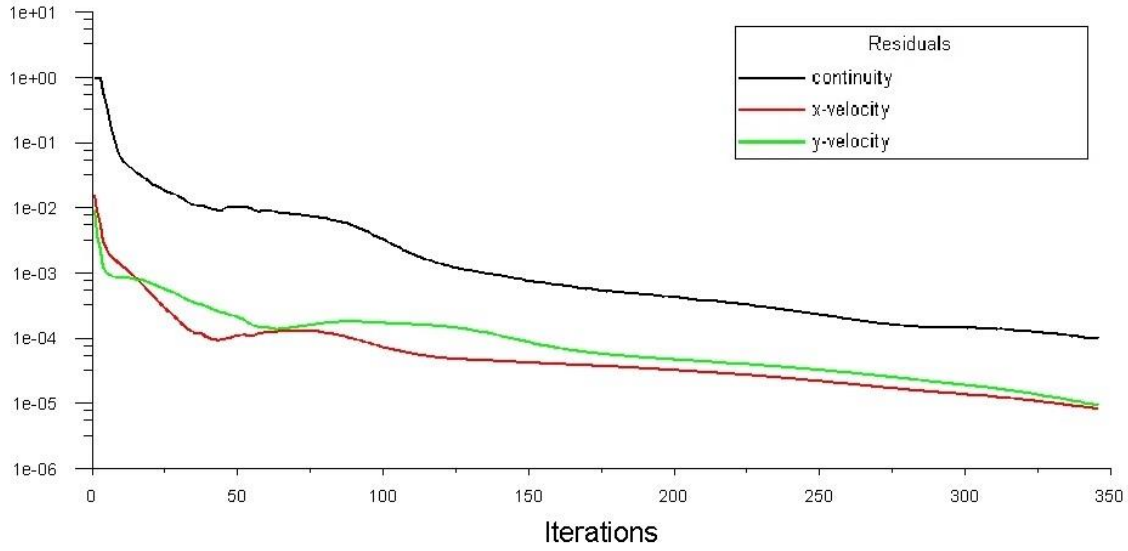

Figure 3-12: Typical behaviour of the residuals for continuity and the velocity along x and y

Inlet Turbulence Sensitivity Study

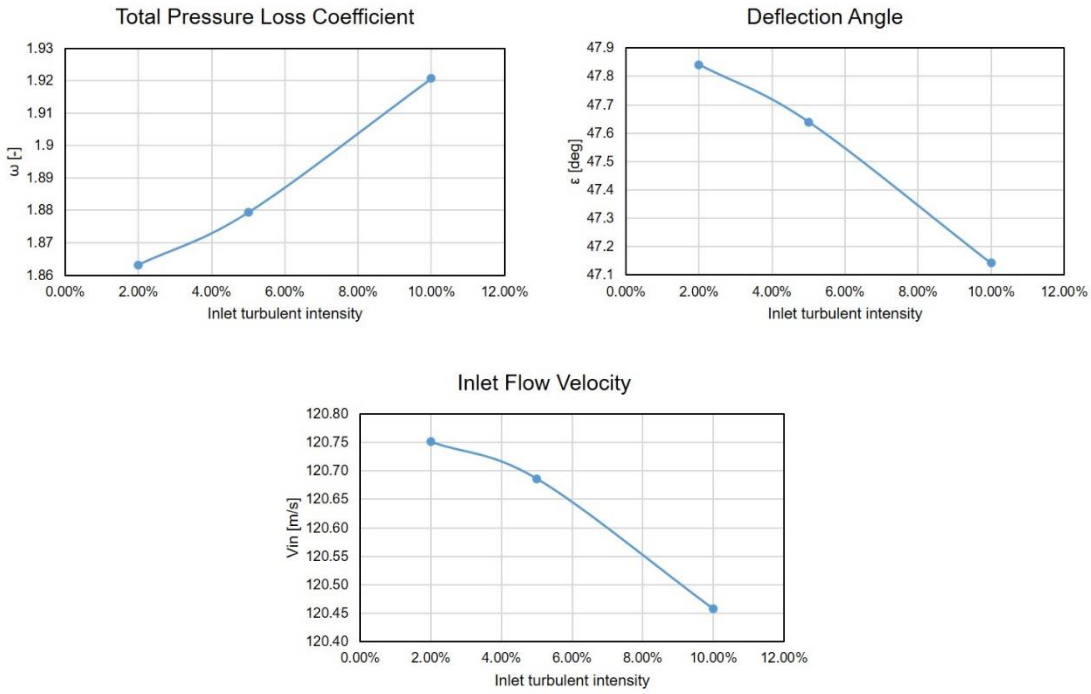

Figure 3-13: Inlet turbulent intensity sensitivity study results

It is important to assess the effect of the inlet turbulence. As specified in the boundary condition settings, a value of $I = 5\%$ has been chosen considering the usual values occurring in turbomachinery. However, the effect of turbulence on total pressure loss coefficient, deflection angle and inlet velocity has been evaluated, considering three values: 2%, 5% and 10%. It is then visible from Figure 3-13 that the effects are not relevant, with deviations lower than 2%.

Solution Monitors

The solution monitors taken into account to check the convergence, together with the residuals value, were the outlet total pressure, from which the loss coefficient is calculated, and the outlet flow angle. Their behaviour is shown in Figure 3-14, with the asymptotic behaviour that implies the convergence of the solution.

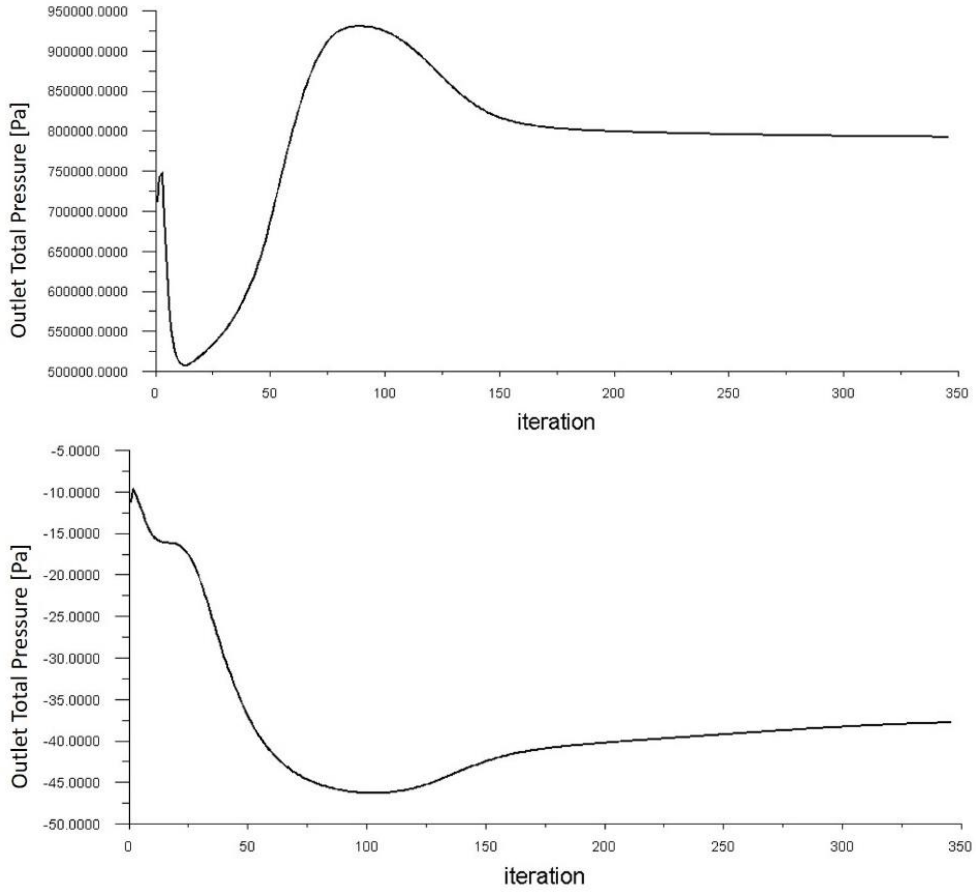

Figure 3-14: Asymptotic behaviour of the considered monitors: total pressure on top, flow angle on the bottom

Solution Methods and Controls

Here are listed the solution methods and control. For all the equations, a second-order resolution has been set to have the highest possible accuracy in the solution.

Table 3-6: Solution methods and controls for the steady-state case

General Settings	Solver	Pressure-based, Steady
	Solution method	Coupled
Spatial Discretisation	Gradient	Least squares cell based
	Pressure	Second order

	Density	Second order upwind
	Momentum	Second order upwind
	Turbulent kinetic energy	Second order upwind
	Specific dissipation rate	Second order upwind
	Energy	Second order upwind
Solution Controls	Flow Courant Number	150
Explicit Relaxation Factors	Momentum	0.5
	Pressure	0.5
Under-Relaxation Factors	Density	1
	Body Forces	1
	Turbulent Kinetic Energy	0.8
	Specific Dissipation Rate	0.8
	Turbulent Viscosity	1
	Energy	1
Residuals	Continuity	1e-04
	x-velocity	1e-04
	y-velocity	1e-04

Concerns about the Steady-state Analysis

The main concern about the steady-state approach is that the flow, particularly at high negative incidence angles, will be highly separated and unsteady processes, such as the vortex shedding and the mixing, will occur, giving rise to an unsteady wake. In the current model, the effect of these is visible is some difficult cases, in which, as shown in Figure 3-15, nor the residuals neither the monitors are

converging, due to the inability to capture the flow field, that is continuously changing.

In CFD, this can influence the final results since using a RANS steady formulation these structures will be averaged as any other turbulent structure and the output parameters, such as the total pressure loss coefficient or the deviation angle, can include an error. Because of this, for some of the points within the design space, unsteady simulations have been run and the possible error assessed.

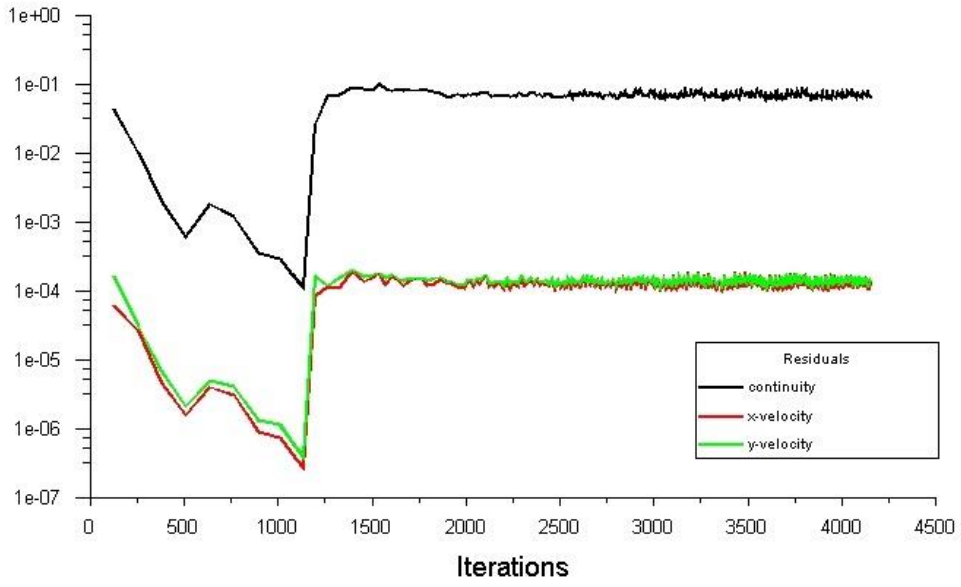

Figure 3-15: Example of high negative incidence case, in which convergence is not reached

3.1.4.2 Transient Analysis

For the transient analysis, two different models have been considered for their capabilities. The first one is the URANS (i.e. Unsteady RANS) k-ω SST model, in which the turbulence is modelled in the same way as the steady-state one, with the difference that the time dependency term is not neglected and, hence, the flow motion is captured. This model is not able to capture all the turbulent length scales (and frequencies) present in the flow field. In fact, it can predict only the frequencies much larger than those of turbulence, without providing any spectral

content of the flow. The results will be then also dependent on the chosen timestep since only some of the turbulence processes will be triggered.

The second one is the SST-SAS (i.e. Scale-Adaptive Simulation) model, introduced by Menter & Egorov [38] in 2005 to deal with the deficiencies of the regular URANS formulation. In fact, although it is based on a RANS approach, it uses an exact transport equation for the turbulent kinetic energy that is able to represent both the large scales of the flow and the dissipative ones.

Compared to the k-ω SST k-equation, the new kinetic energy transport equation has an additional term, called Q_{SAS}, that is responsible for this behaviour. Through this term, derived from the Rotta's kL equation [39], the Von Karman length scale is introduced in the formulation, affecting the turbulence scale equation. The SAS model will then adjust dynamically to the resolved scales, allowing the development of a turbulent spectrum in the separated regions. It will then be able to capture a wider range of turbulence length scales, having possibly higher accuracy. However, it is not possible to control the actual size of the length scale that is solved and the one that is modelled. As it is explained in Section 4.5, this is a problem when parametric studies are conducted, since slightly different geometries can be treated in different ways.

Transient Analysis Geometry and Parameters

For the transient analysis, the four different geometries have been tested for $\sigma = 2.1$ to understand whether the steady-state results were accurate enough or if a correction was necessary. Since the simulations are taking more time than the steady ones, only discrete incidences were taken into account: for the HR6 geometry, $i = [-12°, -22°, -42°, -82°]$, while for the other three geometries, only $i = [-42°, -82°]$ since they are the most challenging cases for the convergence.

Iterative Convergence Residual and Time-step Size Sensitivity Study

For the unsteady case, to check the iterative convergence residual value it is important to consider also the time-step size since it will influence how much the

flow is changing after each step. This has been done in the current case, considering the total pressure loss coefficient for three different simulation cases:

- $R = 1e-04$ and $\Delta t = 1e-07s$
- $R = 1e-04$ and $\Delta t = 1e-08s$
- $R = 1e-05$ and $\Delta t = 1e-08s$

It resulted, as shown in Figure 3-16, that the first one is accurate enough to deliver the results, since the pattern and the average value of the considered output parameter, although a slight difference, have the same pattern. Moreover, it has a considerably lower computational time.

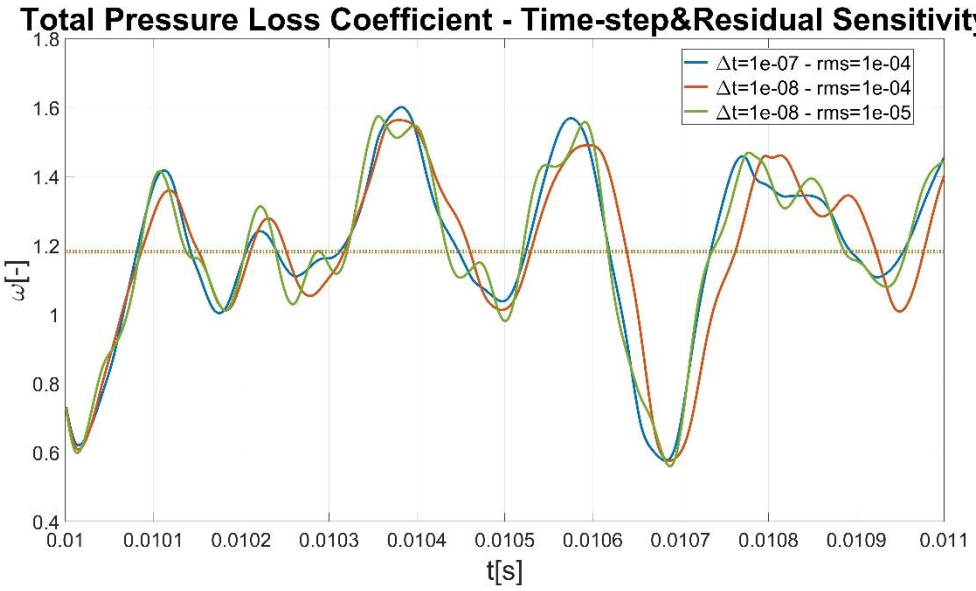

Figure 3-16: Iterative convergence residual and time-step size sensitivity study results

Solution Monitors

For this case, four solution monitors have been considered searching in them the characteristic periodicity predicted by Zachos [36] for this kind of flows. Hence, in addition to the outlet mass-flow rate and the outlet flow angle, the total pressure loss coefficient and the velocity of the freestream jet have been considered.

Solution controls and Methods

Here are listed the solution controls and methods adopted for the transient analysis.

Table 3-7: Solution methods and controls for the transient case

General Settings	Solver	Pressure-based, Transient
	Solution method	Coupled
Spatial Discretisation	Gradient	Least squares cell based
	Pressure	Second order
	Momentum	Bounded Central Differencing
	Turbulent kinetic energy	Second order upwind
	Specific dissipation rate	Second order upwind
	Energy	Second order upwind
Solution Controls	Flow Courant Number	150
Explicit Relaxation Factors	Momentum	0.75
	Pressure	0.75
Under-Relaxation Factors	Density	1
	Body Forces	1
	Turbulent Kinetic Energy	0.8
	Specific Dissipation Rate	0.8
	Turbulent Viscosity	1
	Energy	1
Residuals	Continuity	1e-04

	x-velocity	1e-04
	y-velocity	1e-04
Time Stepping Method		Fixed
Time-Step Size		1e-07 s

3.2 Post Processing

In the post-processing, phase, the software employed have been both ANSYS CFD-Post (Release 19.1) and MATLAB (Release 2018b). As it is defined in the previous sections, two different analysis were carried on in the post-processing. The first part was focused on the steady-state results and will be carried on by comparing the present results with the ones coming from the last year in terms of trends and by considering the actual effect of the camber angle on the correlations.

The second part will focus on the transient results, assessing whether the steady-state results are accurate enough.

3.2.1 Steady-State Analysis

Regarding the steady-state analysis, the data coming from the parametric analysis in ANSYS Workbench have been processed in order to have a simple representation and to draw the conclusions about the dependence of the flow variables from the parameters.

Deflection Angle

The deflection angle is an index of the force applied from the blades on the flow since it is directly connected with the flow momentum change, that can then be decomposed in an axial factor, responsible for the drag and, hence, the losses attributed to the blade profile, and a tangential factor, connected to the lift, and, hence, the force that is actually applied. The main point here was to evaluate the camber effect. However, the solidity effect should be taken into consideration as well to provide a better overview. Hence, the analysis has been conducted by

looking at the curves of deflection against incidence, taking the camber angle and the solidity as parameters.

The first step is to consider the point in which the flow deflection is zero and, hence, the lift on the blade is zero. This will be dependent on both the solidity and the camber angle. Afterwards, starting from these points, the whole curves can be approximated as a line by considering the slope coefficient dependent just on the solidity.

From here, it is then possible to calculate the variation of deflection referred to the baseline set of correlations through the Equation (3-10).

$$\Delta\epsilon = \epsilon - \epsilon_{bl} \tag{3-10}$$

Deviation Angle

Starting from the deflection angle and using the blade metal angles, it is then possible to calculate the deviation angle as:

$$\delta = \epsilon + i + \beta_1 - \beta_2 \tag{3-11}$$

Starting from here, it is possible to analyse this quantity with the same parameters as for the deflection angle. Looking at the deviation angle is useful since it is directly correlated to the capacity of the blade cascade to guide the flow, even in such difficult conditions like this. In fact, as the camber angle is increasing, it will be more challenging for the flow to remain attached due to the more aggressive profile and the deviation angle will increase.

Since the objective of the current project was to develop possible corrections to the baseline model, the considered quantity was again the variation of deviation from the baseline model, through the Equation (3-12).

$$\Delta\delta = \delta - \delta_{bl} \tag{3-12}$$

In this case, it was useful to consider this quantity and plot it as a surface, as a function of both incidence and camber angle, to have a complete overview of its behaviour.

Total Pressure Loss Coefficient

Regarding the total pressure loss coefficient, the data will be considered as a function of incidence, with the camber angle and the solidity as parameters. The total pressure loss coefficient will be calculated using the definition (2-5), taking the following quantities:

- P_{0_1} and p_{dyn}, respectively the mass-averaged total pressure and the mass-averaged dynamic head in the inlet boundary
- P_{0_2} the mass-averaged total pressure in the outlet boundary

To be noticed that, although theoretically it can be assumed that in both the boundaries the flow should be uniform, a mass-averaged approach has been used. This choice has been made since the mixed-out conditions will not be reached until the infinite, so a slight difference along the transversal direction is present and, with this expedient, it can be dumped.

It is important in this phase to bias the total pressure loss coefficient to its lower value. For simplicity, the incidence at which this is assumed to occur was $i = 0°$. This consideration needs to be done since with the CFD the losses due to the surface finish and roughness are not modelled properly. Then, in the final model there will be a term due to surface losses, constant, and a term due to profile and wake mixing ones, that is the term modelled through the CFD analysis:

$$\omega_{biased} = \omega - \omega_{min} \tag{3-13}$$

3.2.2 Transient Analysis

For the analysis of the unsteady results, the first step is to understand whether the initial transient is terminated or the results are still affected by that. In order to do this, two different quantities have been monitored:

- **Velocity Time-history:** the velocity has been measured locating a velocity probe in the blade wake. Due to the geometry features, as suggested by Zachos in [36], it is expected here a periodic behaviour of the flow when the initial transient is finished. Hence, it will be possible to visualize a

sinusoid function with a well-determined frequency and amplitude, dependent on the incidence and camber angle.

- **Total Pressure Loss Coefficient Time-average:** the total pressure loss coefficient will be instead calculated from the overall quantities of total and dynamic pressure, hence with terms that are considering the whole domain. The initial transient is considered terminated when the time-average and the standard deviation of this quantity can be assumed constant. Since this quantity is dependent on the mixing characteristics, that are due to turbulent structures, a slightly more irregular time-history has been found compared to the velocity one.
- **Deflection Angle Time-average:** the deflection angle, as the total pressure loss coefficient, will be calculated using the flow angles calculated as mass flow average at the inlet and the outlet of the fluid domain.

The first two quantities have been calculated for each chunk of data and it resulted that for $t > 0.008\ s$ the initial transient can be considered concluded for every geometry. Once determined the range of reliable and accurate data, the time-averaged quantities from the transient analysis have been plotted against the same quantities found through the steady-state analysis and the error evaluated.

The difference between the two different considered turbulent models has been assessed as well, trying to explain the behaviour of the different results.

4 RESULTS and DISCUSSION

In this section, the result of the project will be presented. First, the general flow features will be discussed, showing the flow field characteristics and giving the means to explain the subsequent outcomes. After this introductory part, the quantitative results will be provided.

Simplified correlations for the zero-lift incidence and for the deflection angle will be presented, discussing the validity and the approximation error from the CFD data. Afterwards, the effects of the camber angle on the total pressure loss coefficient and on the deviation angle will be examined.

In the last part, the differences between the steady-state and the transient results will be discussed, focusing on the applicability of the steady-state approach for this kind of flow fields. A brief analysis about the modality with which the different unsteady approaches are dealing with turbulence and instabilities will then be provided, mentioning the limits of using the SST-SAS formulation in a parametric case with different geometries like the one considered.

4.1 General Flow field Characteristics

In this subchapter, a brief description of the typical flow field occurring in sub-idle conditions is provided. As it is mentioned in the introduction, these are the most extreme ones in which the compressor can operate. In fact, analysing the velocity triangles, the very low shaft rotational speed leads the compressor blades to experience high negative incidence angles. This characteristic will have important consequences on the flow field since wide separation zones and high levels of turbulence with related unsteadiness will be encountered.

As expressed in the Section 3.1.1.4, the range of incidences considered in the current project is between $+20°$, which is an off-design condition towards the blade stall, and $-90°$, the opposite condition in which the stall will be on the pressure side of the blades. Although the extreme off-design conditions, in this case the blade passages will not reach the choked condition. Unlike in a normal operating point, in which they would be surely choked due to the high mass flow,

in the current case it is too low to reach the choking. Moreover, the mass flow rate will be such low that the compressibility effects are negligible. This logic is confirmed by the CFD results: for the HR6 geometry, the model has been run in steady-state for $i = -82°$, that should have the higher velocity, and with the compressible fluid assumption. The Mach contour, shown in Figure 4-1, suggests that the Mach number reached in the throat of the blade passage is well below 1 (around 0.16), so neither choking nor compressible effects will need to be modelled.

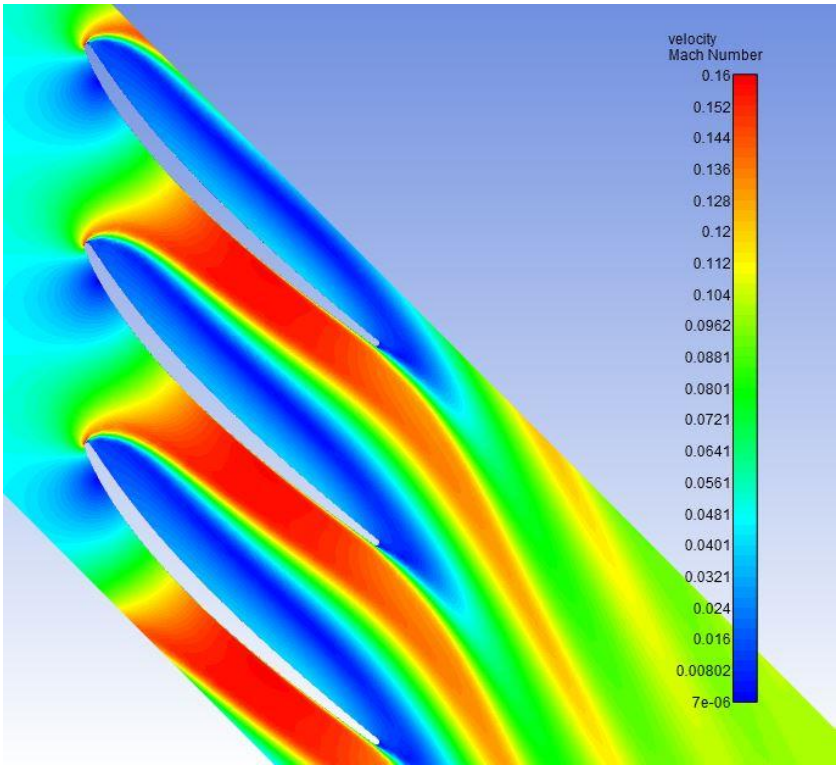

Figure 4-1: Mach number contour for HR6 geometry, $i = -82°$, and compressible flow

Analysing the flow field for the highest negative incidences, it is visible that the stagnation point will be located on the suction side of the blade. This means that the flow, in order to go around the leading edge and reach the pressure side, will accelerate reaching very high velocities. The flow turning will be then almost $180°$. Since the flow has significant inertia due to the high velocity (i.e. the local Reynolds number will be very high) then it will not be able to complete this

process and it will end up with a big separation zone detaching from the leading edge. It is the author's view that, since the separation is occurring in this way, the results are not highly dependent on the flow Reynolds number, unless it is very low or low incidence is considered. In fact, it only affects the boundary layer separation on the blade walls and, since for the high incidence cases the boundary layer is already detached, its influence should not be considered. However, in case the flow is attached to the blades, hence for small incidence angles, the Reynolds number will have an effect on the results.

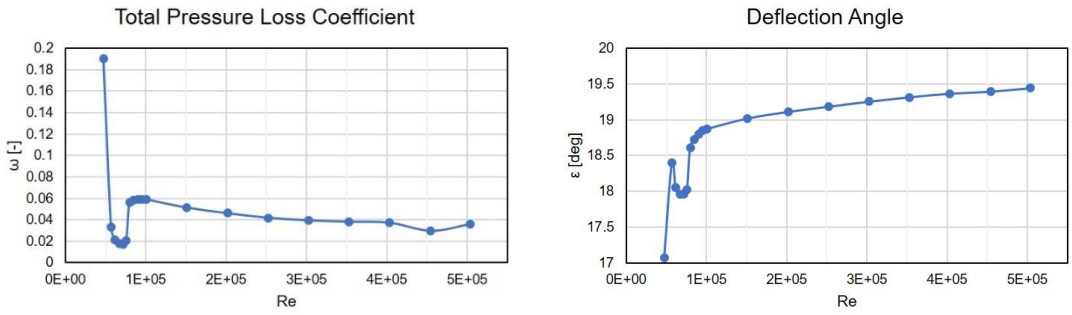

Figure 4-2: Reynolds number sensitivity study results, for $i = -2.7°$

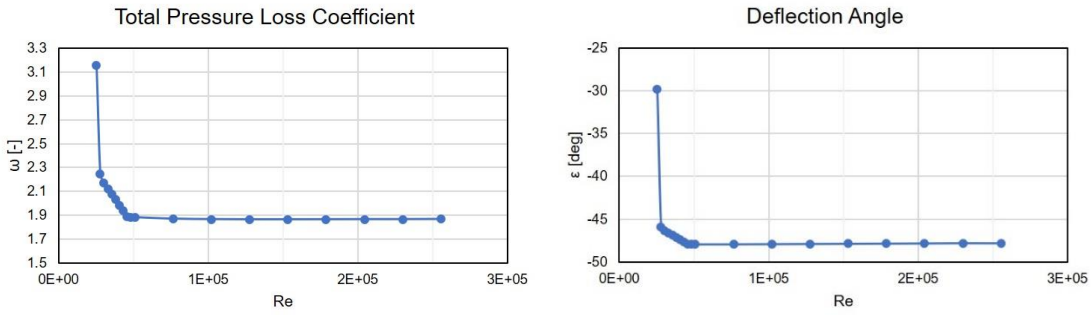

Figure 4-3: Reynolds number sensitivity study results, for $i = -52.7°$

To demonstrate this logic, a set of parametric simulations has been run for the HR6 and with $\sigma = 2.1$ geometry, changing the outlet target non-dimensional mass flow from 0.01 to 0.1. The Reynolds number was changing because of the velocity change, dependent on the mass flow rate and on the chosen incidence. The order of the minimum registered value is $Re \sim 10^4$. As it is shown in Figure 4-2, at incidence close to design one (i.e. $i = -2.7°$) and hence an attached boundary layer, the Reynolds number is affecting both total pressure loss coefficient and

deflection angle, due to the different characteristics that the boundary layer will develop. However, at the high negative incidence cases, of particular interest in the current research for the highly detached flow, Figure 4-3 (at $i = -52.7°$) is showing that the Reynolds number is affecting the results only at very low values (for $Re \sim 10^4$), and, hence, in a very restricted range for which there is no necessity for a further investigation due to the high levels of turbulence present in the real flow, that will muffle its effects.

In the following subsections, the main flow features will be described.

4.1.1 High Separation Zones

As it is mentioned previously, at high negative incidence the flow on the pressure side of the blades will be totally separated. This characteristic depends exclusively from the incidence angle, although some differences are present due to solidity or camber effects.

Incidence Effect

The description is starting from an incidence close to $0°$ (exactly, $i = -2°$), which has a flow field like the one in Figure 4-4a. There, it is visible that the flow is attached along the whole blade wall extension of both the pressure and the suction side, with a very low deviation since it is very well guided. In this case, whilst the total pressure is decreasing due to the profile and trailing edge losses, the static pressure is rising, and the compression is taking place. Increasing the incidence to positive values (e.g., in Figure 4-4b, $i = 3°$) leads the flow to separate on the blade suction side near the trailing edge due to the adverse pressure gradient developed there. The wake width will then be slightly higher, with consequent higher total pressure losses.

Moving towards negative incidence values (in Figure 4-4c, $i = -7°$), the flow stagnation point shifts down to the suction side. To follow the blade shape, the flow will then need to accelerate round the leading edge. Since the acceleration is still not excessively big, there is no separation in this case. Keeping lowering the incidence, the stagnation point will keep moving down the suction side. The

flow will then need a higher acceleration to overcome the leading edge and, hence, it will struggle more to remain attached. Indeed, from $i = -12°$ (Figure 4-4d), the pressure side boundary layer starts to thicken, generating a wider wake as well. It has a direct effect on the total pressure loss coefficient (Figure 4-19): from this incidence downwards, it starts rising from the minimum value around $i = 0°$. The flow separation is not already occurring, but the thicker boundary layer is anticipating the incoming separation. The recirculation bubble present on the blades, and located in different positions, is a sign that the flow holds an unsteady component, for which the model predicts the bubble position in different points.

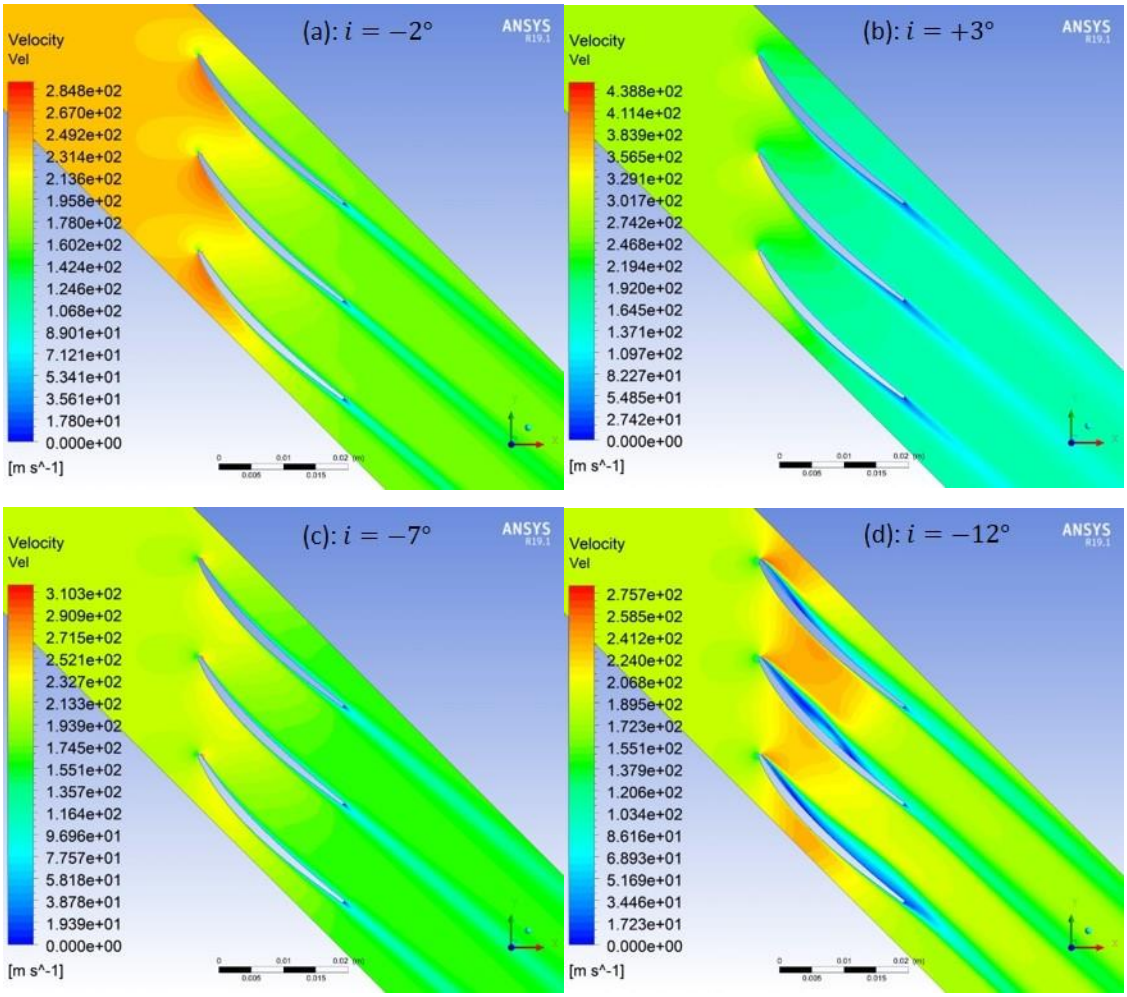

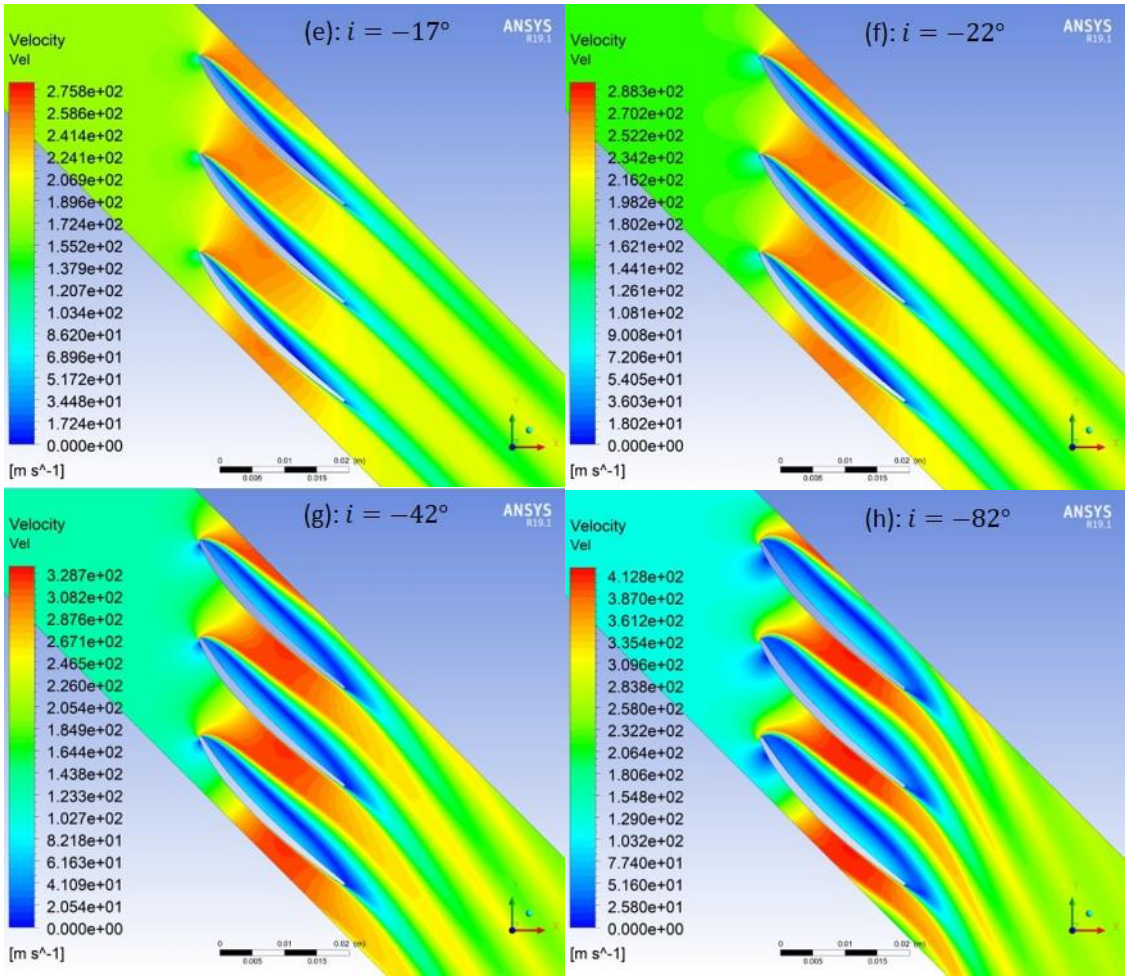

Figure 4-4: Flow field for the analysed incidence range

From $i = -17°$ downwards (from Figure 4-4e to Figure 4-4h), the flow is clearly fully detached from the leading edge, and the separation bubble is involving the whole pressure side of the blades. The wake is, of course, getting wider, with consequent higher total pressure loss, given by the more powerful mixing process encountered. With the lowering of the negative incidence, the centre of the separation bubble point is moving downstream, with a separated zone that can be such wide to be extended over the trailing edge. The bigger recirculating zone is having a blocking effect on the flow as well(Figure 4-4h): since the available passage area is reducing, the velocity of the freestream jet will increase, with consequent higher total pressure loss due to shear stresses for the velocity gradient.

In these conditions the losses arise mainly due to the wake generated by the wide separation, with significant velocity gradient between the freestream jet and the stagnation zone.

Solidity Effect

The solidity has a big effect on the flow field, that needs to be considered as well. In fact, the transversal distance of the blades is highly affecting the separation zone width and the incidence at which the detachment is occurring. Analysing the flow for the three different solidities, the presence of the cascade effect is clear, especially between $\sigma = 0.7$ and $\sigma = 1.4$.

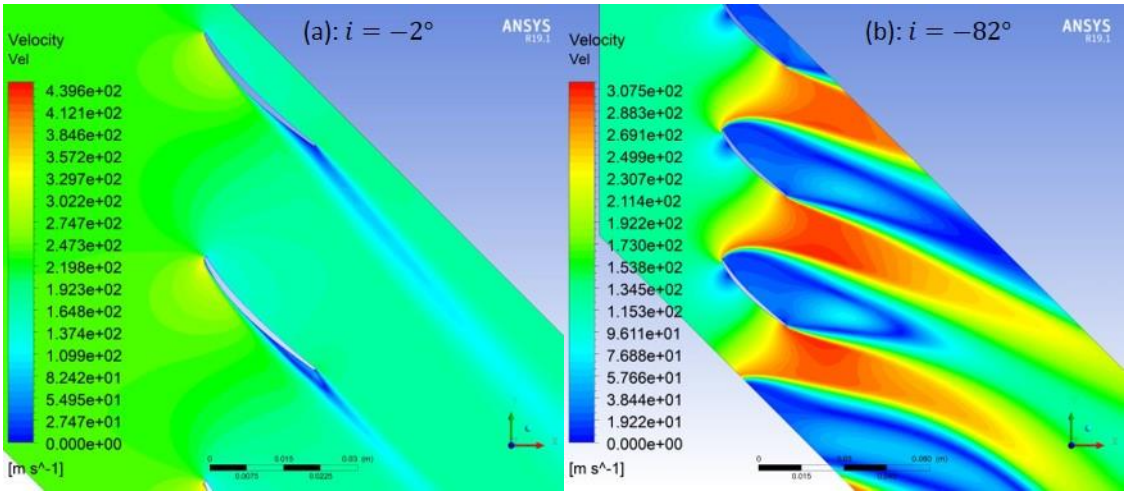

Figure 4-5: Flow field at $\sigma = 0.7$

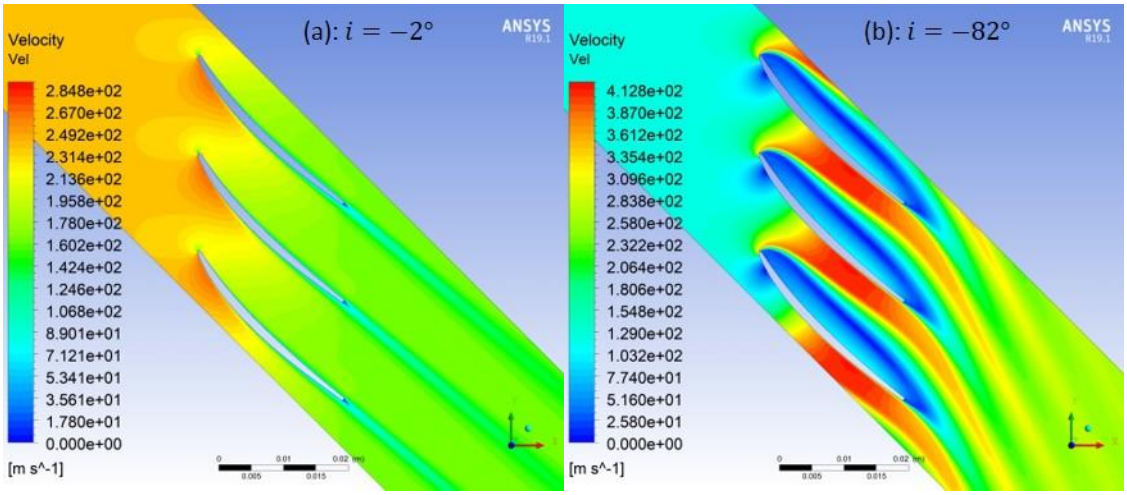

Figure 4-6: Flow field at $\sigma = 2.1$

In fact, independently from the chosen blade geometry, the flow is more guided for $\sigma > 1.4$. As shown in Figure 4-5 and Figure 4-6, for $\sigma = 0.7$ the effect of the adjacent blades is neglectable, with a behaviour very similar to an isolated blade. Therefore, the separation occurring at negative incidence will be much wider in this case rather than for $\sigma = 2.1$.

The effect will be present at both low incidences (in (a), $i = -2°$) and high ones (in (b), $i = -82°$). Lower solidities are always producing a wider wake, but, of course, the blockage effect will not be as significant as in the higher solidity cases, reducing the velocity as well as the velocity gradient, and hence the losses. Lower solidities will affect the flow deflection as well: compared to higher solidities, it will have a lower absolute value for both positive and negative incidences.

4.1.2 Unsteady Flow Features

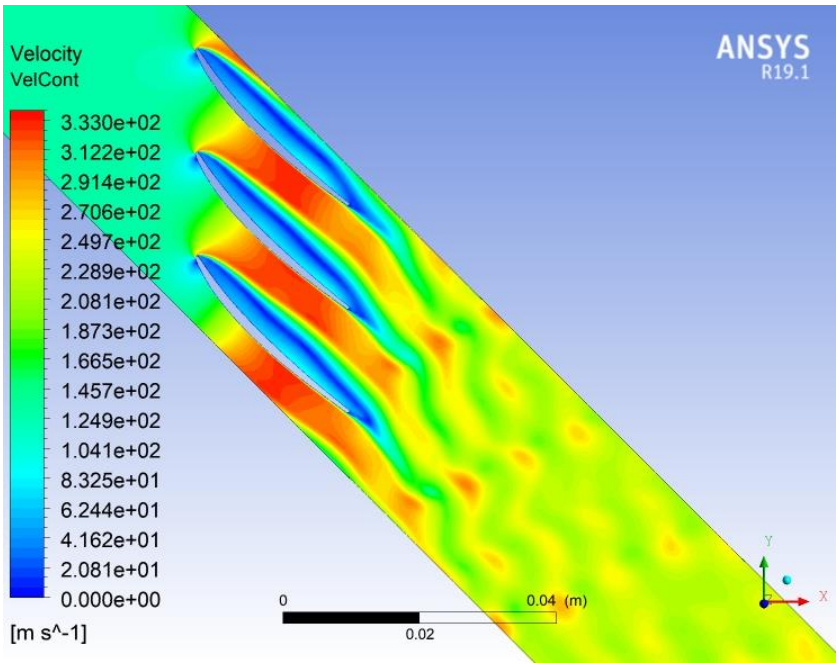

Figure 4-7: Velocity contour for HR6 blade ($\Delta\theta = -1.50°$) at $i = 42°$ for SST-SAS model

As it is mentioned before, when the flow starts to separate a high component of unsteadiness is likely to be present. Hence, it is important to consider its characteristics. To be noticed that in the current case only a 2D analysis has been

performed and, hence, a simplistic approach was chosen, not considering that, in reality, the turbulence involves a highly three-dimensional flow field. However, this choice allowed to explore the necessary range of incidences and geometries to understand the general behaviour of the flow, that can still be captured.

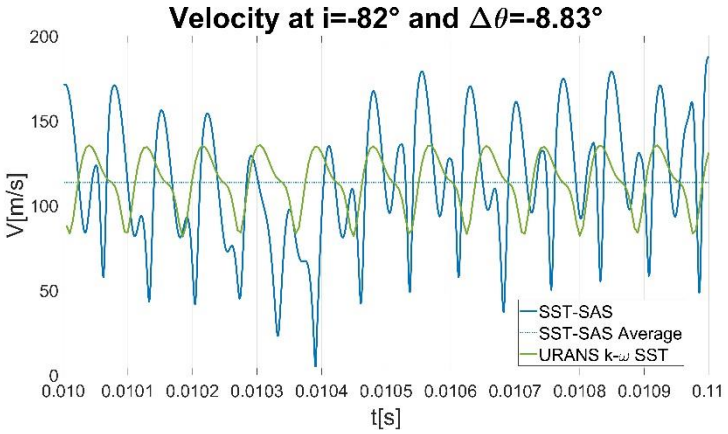

Figure 4-8: Velocity time-history for HR1 geometry and $i = -82°$

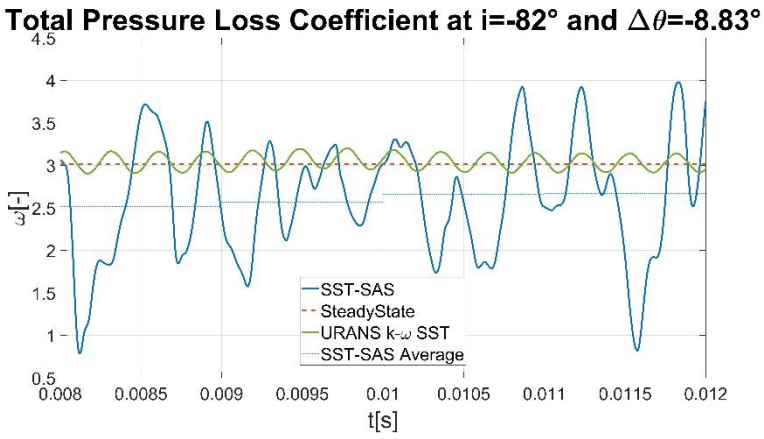

Figure 4-9: Total pressure loss coefficient time-history for HR1 geometry and $i = -82°$

As it is shown in Figure 4-7, the analysis of the cascade geometry for the unsteady case can give important hints. First, the structures generated downstream the blades will be periodic, with vortices that are detaching from the separation zone. The periodicity of the process is also visible in the time-history of the wake velocity, shown in Figure 4-8. Although the flow field is periodic around the blades and just downstream them, its features in the mixing plane are

more complex. In fact, it is impossible to clearly identify one frequency in the total pressure loss coefficient since the diffusion process will dump or emphasise some of them. Moreover, the modelled viscous process and the dissipation rate will stretch the vortices due to the energy cascade, redistributing the kinetic energy along the whole length scale. As it is shown in Figure 4-9, this complexity is well captured in the SST-SAS approach, that has a great standard deviation on the pressure loss coefficient values. The RANS k-ω SST one is instead capturing the average characteristics of the flow, dumping most of the turbulence structures

Having described the general features of the flow field, it is now important to discuss the phenomena from a quantitative point of view.

4.2 Simplified Correlation for Zero-lift Incidence and Deflection

In this section, the simplified correlations for approximating the zero-lift incidence and the deflection angle will be presented, considering their accuracy as well.

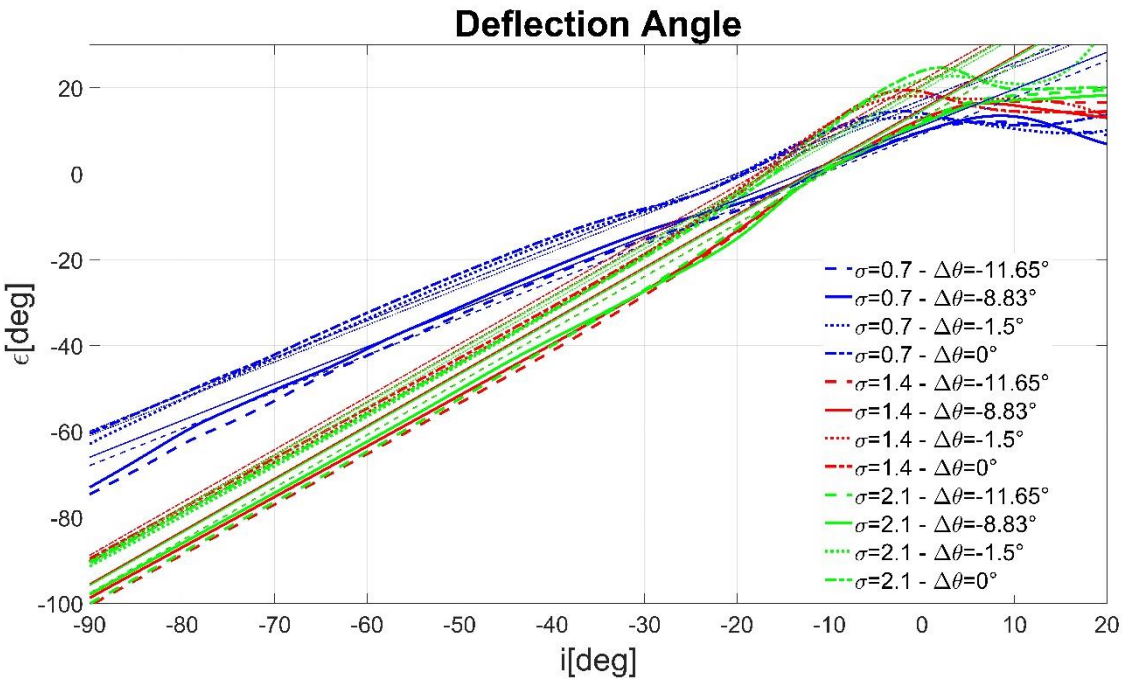

Figure 4-10: Deflection angle, plotted with solidity and camber angle parameters

Looking at the plot of the deflection as a function of incidence in Figure 4-10, the most significant parameters that affect its behaviour are the solidity and the camber angle. The relationship between deflection and incidence, as it can be expected for general blades, can be approximated as linear up to a point close to the stall. The slope coefficient will be only dependent on the solidity considered, while the effect of the camber is to shift the function: at a fixed incidence and solidity, as it increases, the deflection will be higher. Of course, it is also going to affect the stall point of the blades: as the camber angle increases, the blades will offer a more aggressive profile to the flow, with consequent higher adverse pressure gradient. The stall will be then more likely to occur at lower incidence.

The zero-lift incidence, that can be also considered the zero-deflection one, will change as well due to this effect in the same way: as the camber increases, the zero-deflection incidence will decrease. It is also dependent on the solidity since the blade proximity will affect the way the flow behaves around the walls. Since it has these characteristics, in order to get the whole deflection approximation, it is appropriate to start from its analysis, and then find the correlations for the whole function.

4.2.1 Zero-Lift Incidence Correlation

For the zero-lift incidence, it can be considered as a function of two main geometric parameters: the camber angle and the solidity. As can be seen from Figure 4-12, the dependence of this quantity from the camber angle can be assumed as linear. Nonetheless, since the lines are scattered for different solidities, the linear slope coefficient of each of them is assumed as a function of the solidity. In the following, the correlations are presented.

The slope coefficient of the linear functions m_σ is fitted through a power function with two terms, of the type:

$$m_\sigma = a_m \, \sigma^{b_m} + c_m \qquad \textbf{(4-1)}$$

The three coefficients are specified in Table 4-1. The value of m_σ along the considered solidity range is plotted in Figure 4-11.

Table 4-1: Coefficients of Equation ((4-1)

a_m	-0.9912
b_m	-0.2675
c_m	0.7505

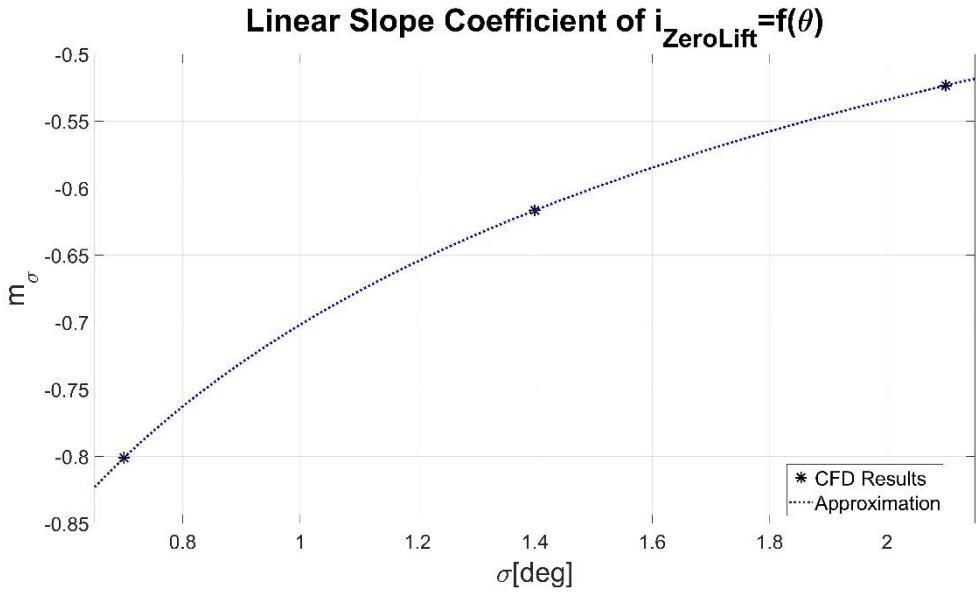

Figure 4-11: Value of m_σ for the determination of the zero-lift incidence

As the slope coefficient is found, it is then possible to calculate the actual linear function for the zero-lift incidence as:

$$i_{ZeroLift} = m_\sigma \, \Delta\theta + i_0 \qquad \textbf{(4-2)}$$

In which m_σ is the coefficient calculated before and $\Delta\theta = \theta - \theta_0$. The coefficients for this equation are specified in Table 4-2.

Table 4-2: Coefficients of Equation (4-2)

i_0	$-10°$
θ_0	$14.5°$

The behaviour of this linear approximation is plotted in Figure 4-12: it is catching the main characteristics, with a maximum error of around $1°$.

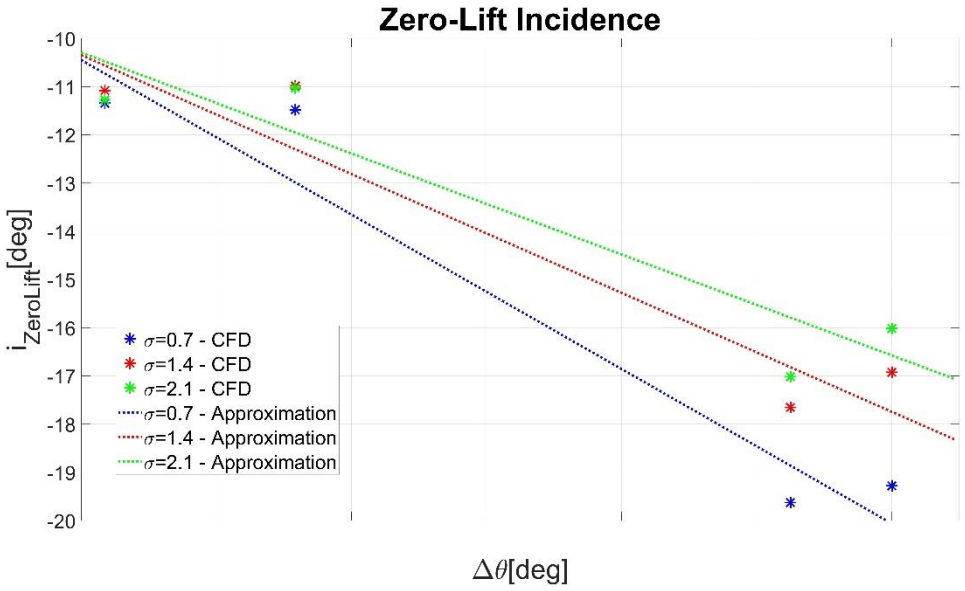

Figure 4-12: Zero-lift incidence, with the comparison between the CFD data and approximated ones

4.2.2 Deflection Correlation

Once the zero-lift incidence is calculated, it is then possible to approximate the deflection behaviour as a function of incidence. As mentioned before, it will be considered as linear, with lines passing through the zero-lift incidence points. This constraint will express the dependence of the deflection from the camber angle.

The linear slope coefficient, called n_σ, will be a function of the solidity. In order to have a more accurate fitting, the data from Allegretti's [8] project have been taken, since more points are available in the chosen solidity range. Hence, the data have been divided into two different behaviours, as shown in Figure 4-13:

- For $0.7 < \sigma < 1.4$, a cubic function is assumed to be the best for fitting the linear slope coefficient of the deflection function, as expressed by this equation, with the coefficients expressed in Table 4-3:

$$n_\sigma = a_n\,\sigma^3 + b_n\,\sigma^2 + c_n\,\sigma + d_n \qquad \textbf{(4-3)}$$

- For $1.4 < \sigma < 2.1$, the linear slope coefficient has been considered independent from solidity, with the value of $n_\sigma = 1.2281$.

Table 4-3: Coefficients of Equation (4-3)

a_n	0.5107
b_n	-2.4969
c_n	4.0585
d_n	-0.9613

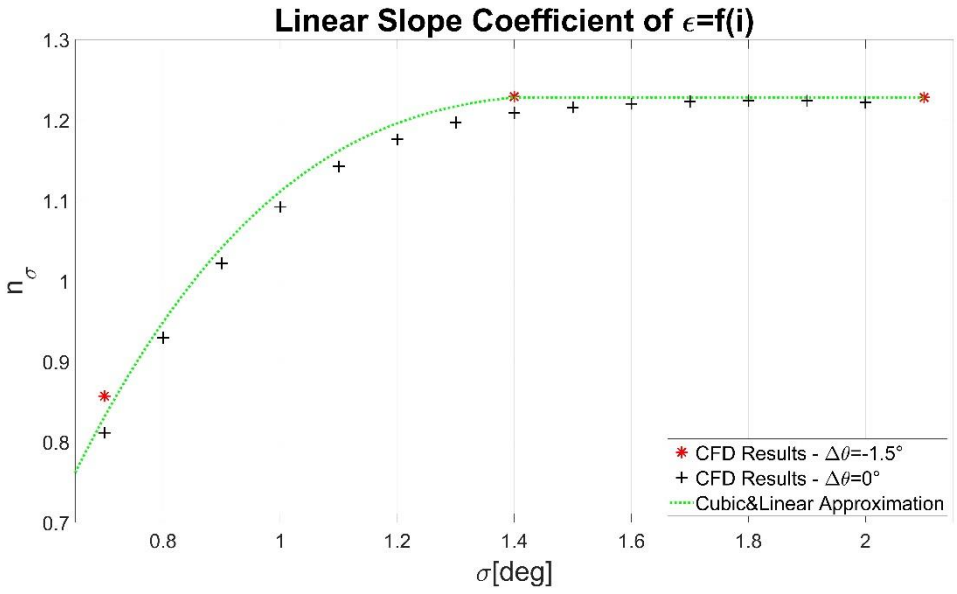

Figure 4-13: Value of n_σ for the approximation of the deflection

The deflection will be then calculated through the following equation:

$$\epsilon_{approx} = n_\sigma (i - i_{ZeroLift}) \quad \textbf{(4-4)}$$

In Figure 4-10 both the approximated functions and the CFD results are plotted (the approximated data are the thinner lines). Although in the deflection figure the trend is well followed, the error between them is higher than expected (Figure 4-14). Observing this plot, it suggests that, although the error is acceptable for the two lower camber angles, it is too big for the two higher camber angles. As

expected, where the stall starts affecting the deflection characteristics, they cannot be assumed as linear anymore and the error starts since the fitting is not suitable anymore.

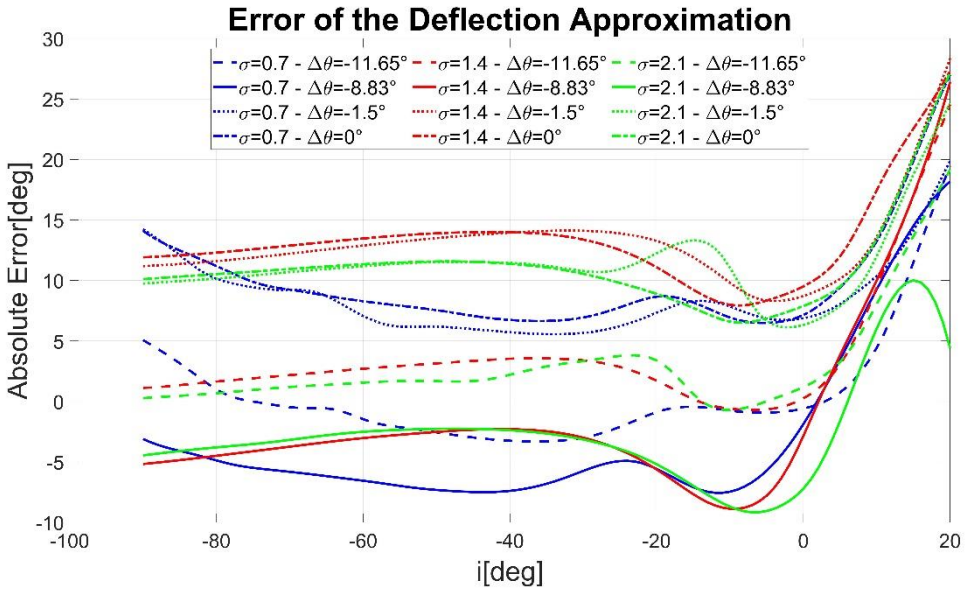

Figure 4-14: Error of the deflection approximation, for the different solidities and camber angles

4.3 Effect of Camber on Loss & Deviation

In this section, the main results regarding the camber effect on the correlations will be presented. As explained before, the camber angle of the blades will influence the way the flow field and the boundary layer will develop around the walls. In fact, a higher camber is leading to a higher theoretical deflection of the flow due to its more aggressive profile. However, it will develop higher acceleration on the suction side and higher adverse pressure gradients, with a boundary layer that will be more prone to separate. A higher camber will then lead to a higher deviation of the flow due to the difficulty to maintain the flow attached and to guide it. This is shown in Figure 4-15: for the same incidence angle, the HR6 geometry, with a higher camber angle, is developing a much thicker boundary layer than the IR8 one, with a lower camber angle. The effect is also visible in the exit flow angle, parallel to the wake direction: the HR6 geometry has a more deviated flow that the IR8 one. Nevertheless, the absolute deflection

of the HR6 geometry will be higher, with the possibility of a more significant compression. To be considered that, as mentioned before, in compressors the cascade effect is relevant, hence the separation of the flow, and the consequent higher deviation angle, will be affected by the solidity parameter as well.

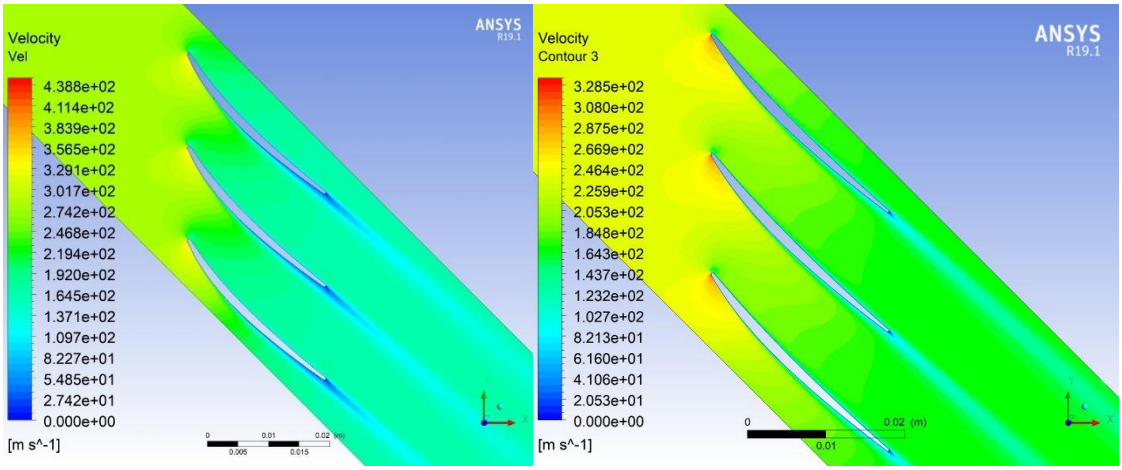

Figure 4-15: Velocity contours for two different geometries: on the left, the more cambered HR6 ($\Delta\theta = -1.50°$), on the right the less cambered IR8 ($\Delta\theta = -11.65°$)

However, in the conditions analysed in the present project, it would be inappropriate to explain the occurring phenomena in this way. In fact, as the incidence angle is decreasing (i.e., for $i < -15°$), the flow will be detached from the blade pressure side and it will not follow its curvature. Despite that, the freestream jet, passing through the cascade passage, will be guided by the blade suction side as well as the fictitious wall of the separation bubble. Since the interaction between these two effects is difficult to predict, the CFD results are taken into account. The consequent results are plotted in Figure 4-10. As discussed before, the effect of the camber angle at these high negative incidences is to lower the absolute value of the deflection all over the considered incidence range, from $i = -90°$ to $i = 0°$. The approximation of this behaviour is however not accurate enough, as discussed before. Another approach has then been considered.

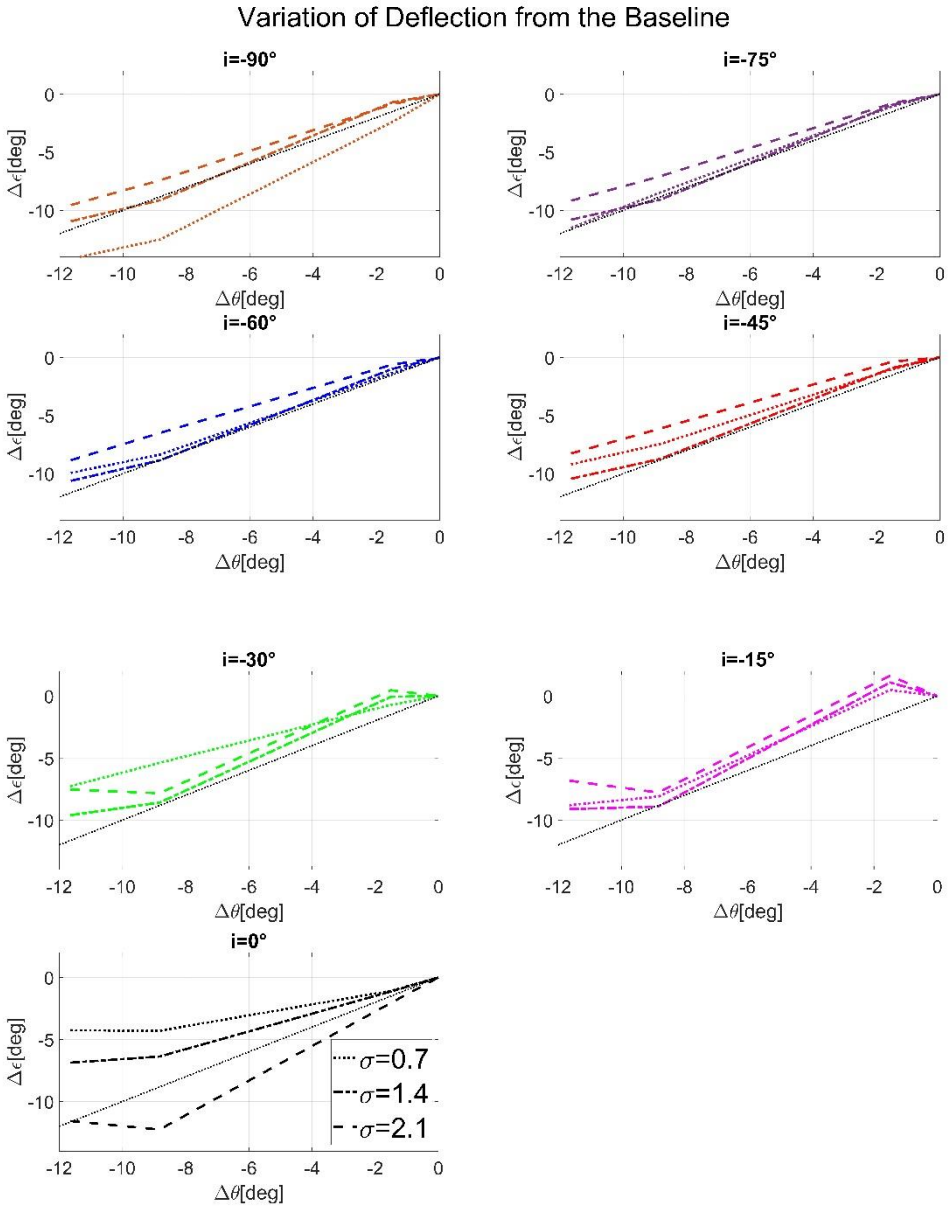

Figure 4-16: Variation of deflection from the baseline model, with the black dotted line to show the 1:1 ratio

The alternative approach was to consider the variation of the deflection from the baseline as a function of the camber. In this case, has been shown that, for the incidences below $-15°$, the data will follow a 1:1 ratio between the two considered variables, as shown in Figure 4-16. Hence the effect of the camber angle on the deflection angle can be considered only the camber itself, without any other

factor. This effect is better understandable by analysing the deviation angle, as discussed in the next subchapter.

4.3.1 Effect on Deviation Angle

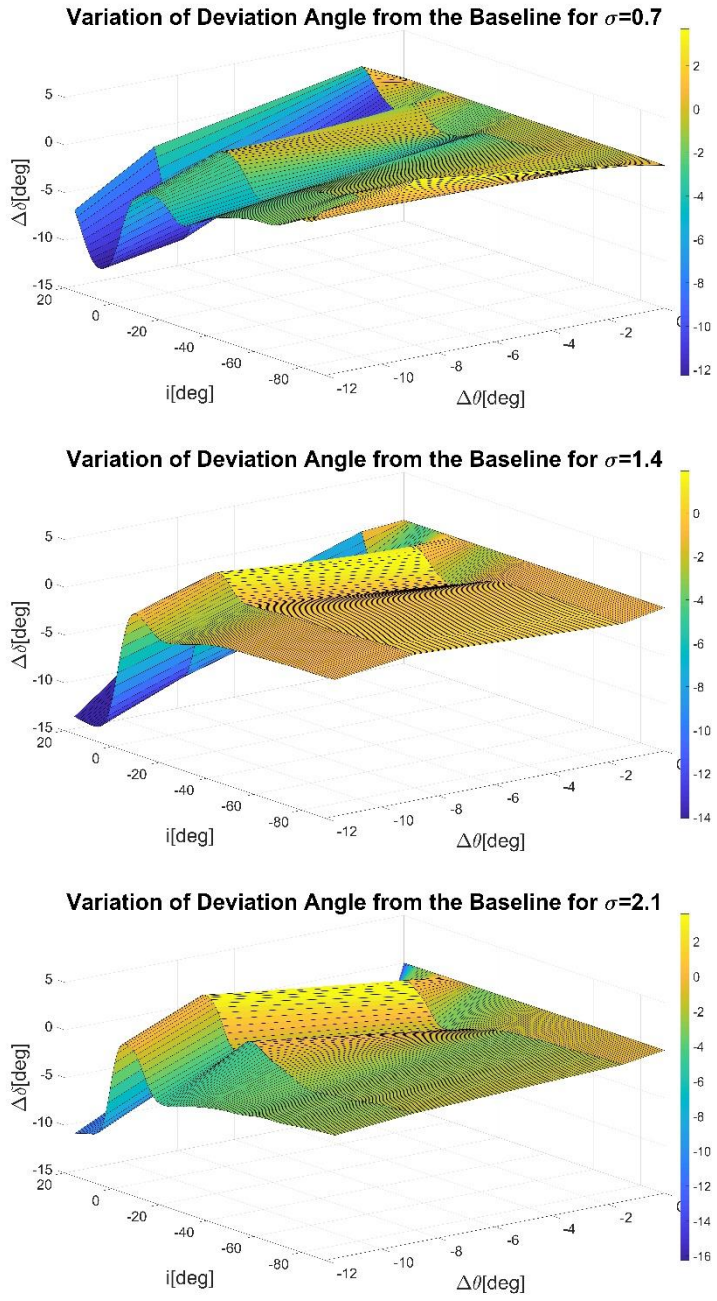

Figure 4-17: Variation of deviation from the baseline, for the three considered solidities

Since the correlations found for the deflection angle were not giving the right accuracy needed for the current model, then the focus has been shifted on the deviation angle characteristics. In fact, it is a more appropriate variable to check since the camber angle dependence is already contained in it, giving a simpler approach.

The quantity analysed has not been the deviation for each geometry but the difference of its value from the baseline one. In fact, while the deviation is a function as well of the incidence angle, analysing its change from the baseline allows to decouple it, giving a simpler understanding. Analysing then the difference from the baseline, it resulted that, as shown in Figure 4-17, for $i < -15°$, hence from the cases in which the flow is detached from the pressure side, this quantity is very small, of the order of $\pm 2°$. Considering the very high values of deviation occurring here (i.e. around $30°$), it means that the effect of the camber angle on the deviation angle can be considered negligible. This result confirms what stated in the previous subchapter: it can be assumed that, for a detached flow, the effect on the deflection angle is only the camber variation itself. No more effects of flow deviation need to be taken in account.

This outcome is valid for all the three tested solidities: from the three plots of Figure 4-17, it's visible that when the incidence is well below the separation incidence, no effect is encountered on the deviation.

The behaviour above $-15°$, hence for attached flow, is more complex. In fact, by looking at the variation of deviation with the camber angle, the trend is not monotone. It is the author's opinion that the behaviour for the different geometries at $i \sim -15°$ (Figure 4-18) is due to the different incidence at which the separation is occurring caused by the different camber angle. While the more cambered blade (i.e. the baseline, with $\Delta\theta = 0°$) has a separated flow, the second blade (i.e., $\Delta\theta = -1.50°$) has still an attached flow. This means that despite the small difference, for the second blade the deviation will be lower. This is suggesting that the camber angle has still an effect at the incidences in which the flow is

attached, and it is the normal effect described in the previous section and already known.

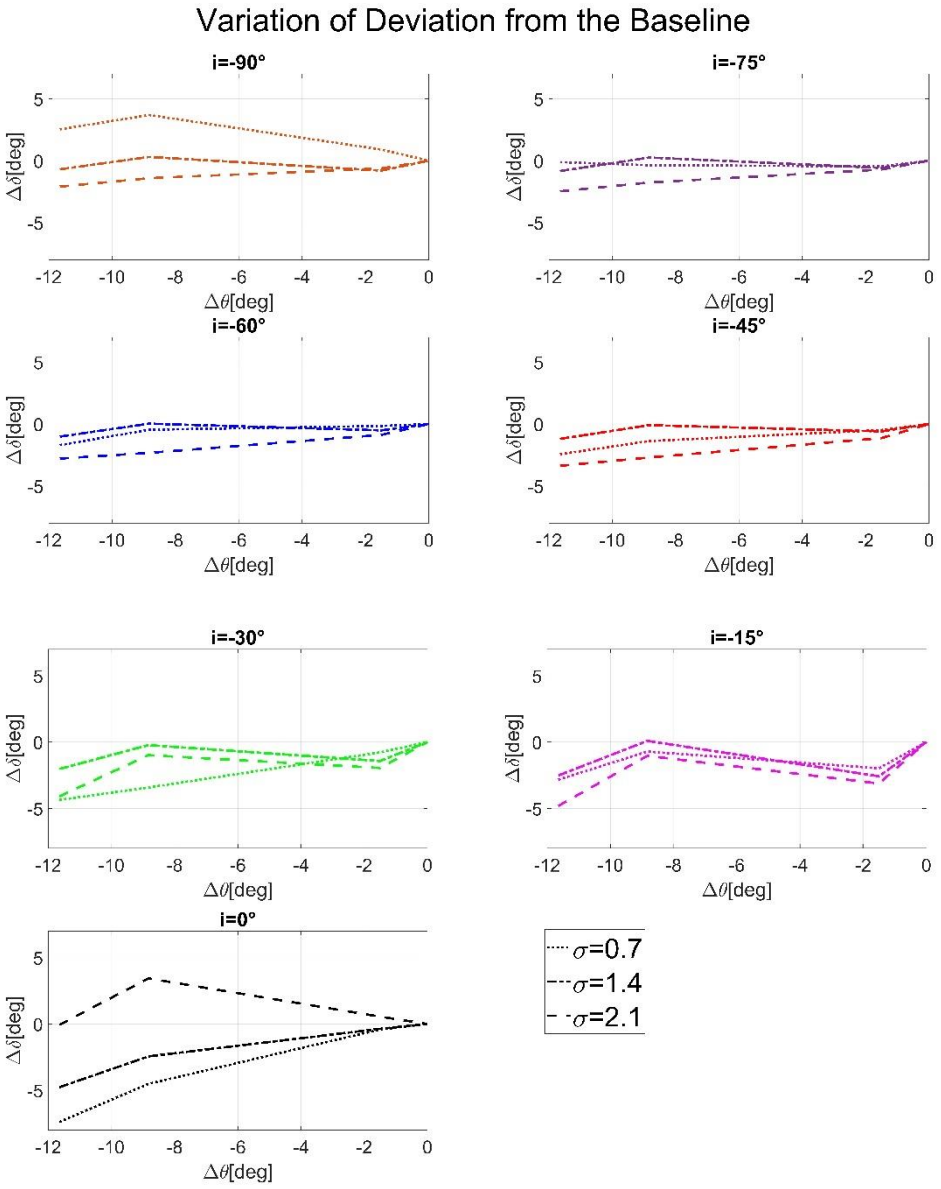

Figure 4-18: Variation of deviation from the baseline, shown for the different incidences

4.3.2 Effect on Total Pressure Loss Coefficient

The total pressure loss coefficient, plotted as a function of the incidence angle, is shown in Figure 4-19. It is visible that the effect of solidity is much more significant than the one of the camber angle since the data are grouped for solidities. For

the highest solidity, hence for $\sigma = 2.1$, the total pressure loss coefficient is the highest, among the three configurations. This happens because of two main factors. First, although the blades are closer to each other with a more significant cascade effect and a higher compression performance, there will be a proportionally higher wetted surface compared to the lower solidities. Hence, a higher portion of mass-flow will be involved in the boundary layer and more losses will be encountered due to friction losses within it. The second reason is that, since the blockage effect of the separation bubble will be more considerable on the smaller passage, then higher maximum velocity and higher velocity gradients will occur, leading to bigger shear stresses and losses due to the viscous effects. At the lowest solidity (e.g. $\sigma = 0.7$) the losses are limited by due to the lower velocity of the flow and the consequent lower viscous friction, even though the wake is much thicker due to the lower cascade effect.

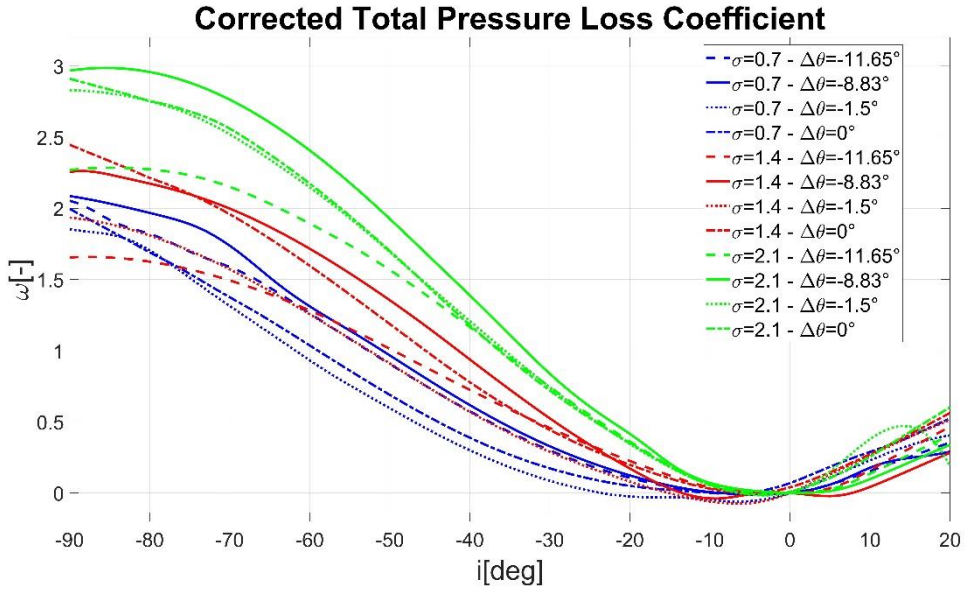

Figure 4-19: Corrected (biased) total pressure loss coefficient

The effect of the camber angle on the total pressure loss coefficient is showed in Figure 4-20. As can be seen from there, a trend cannot be detected at any of the considered incidences. The variation of loss is, in fact, showing to be fluctuating around a mean value. It is the author's view that, as mentioned before, this behaviour can be due to the intrinsic unsteadiness present in the flow, that cannot

be detected properly by the steady-state solver. It would be then more appropriate to analyse the behaviour of the flow using a transient approach, able to capture the unsteadiness typical of this kind of flow. It is important to proceed in this direction not only because of this outcome for the total pressure loss but also to check if the steady-state results can be considered reliable in all the incidence range.

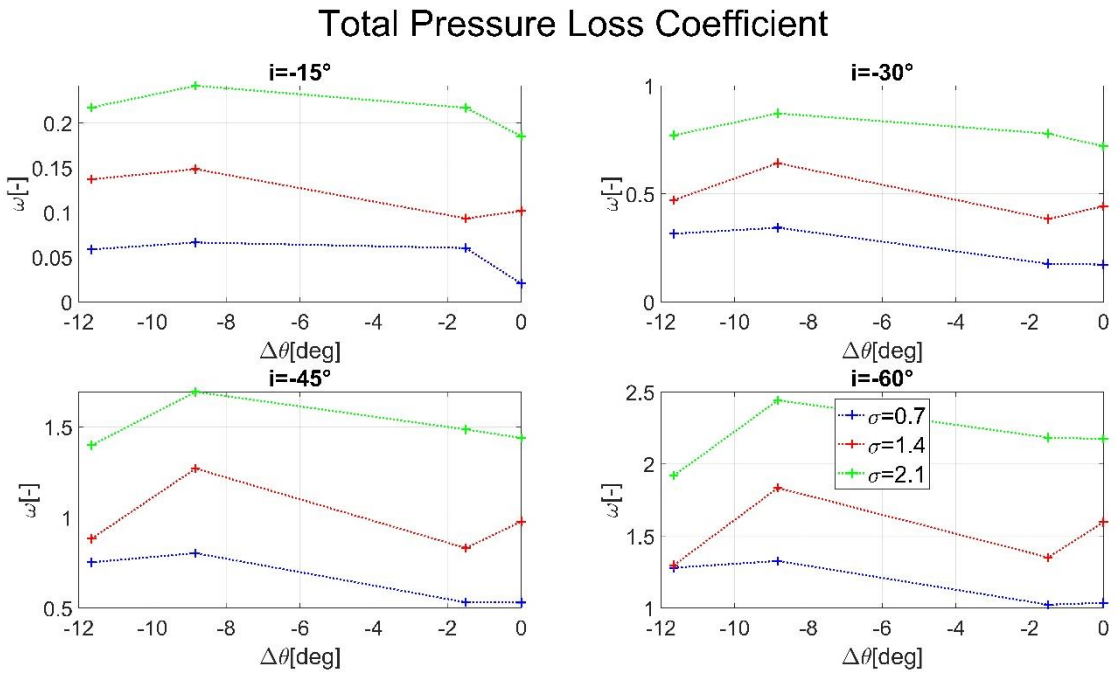

Figure 4-20: Total pressure loss coefficient trend, plotted as function of camber variation

4.4 Applicability of the Steady-State Approach

In this section, the validity of the steady-state results will be assessed, comparing them with the transient results. The discrepancy between the two approaches will be discussed by comparing both the time-average and the standard deviation of the data coming from the two models described in Section 3.1.4 with the steady-state ones. Checking the outcomes, while the URANS k-ω SST model is giving consistent results, for the SST-SAS more differences between the results are present and some considerations need to be done. This will be discussed in

Section 4.5. However, the comparison will consider the results of both the models.

4.4.1 Total Pressure Loss Coefficient

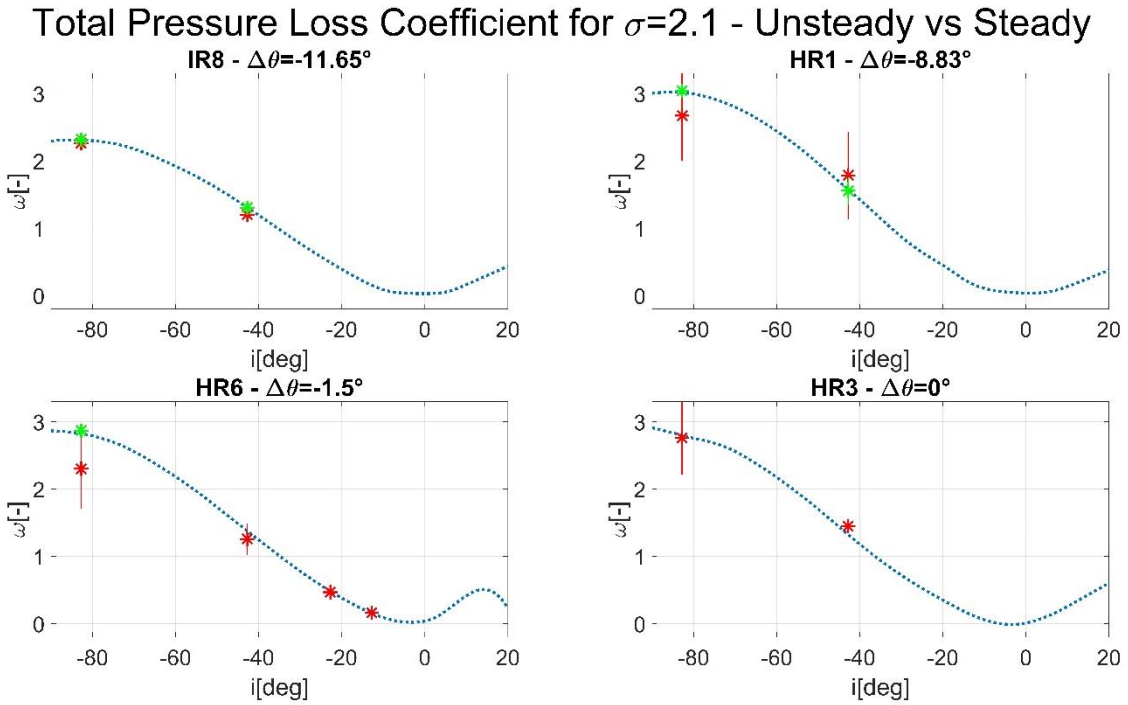

Figure 4-21: Summary of average and standard deviation of the total pressure loss coefficient; in red the SST-SAS model results, in green the URANS model ones.

Regarding the total pressure loss coefficient, depending on the turbulence model there will be two slightly different behaviours. In Figure 4-21 is shown the comparison between the steady-state results and the transient ones. The same values are presented in Table 4-4. Analysing both the data, it is clear that the URANS k-ω SST model is agreeing with the steady-state results since for each case the time-average has a negligible error.

Regarding the results of the SST-SAS model, they are different depending on the considered geometry. For most of the cases, the steady-state results fall within the standard deviation range. However, for the HR6 geometry, this doesn't happen: it has a much bigger error, that seems to be dependent on the incidence. Moreover, this model is giving a much bigger standard deviation in the results,

compared to the URANS k-ω SST one. Moreover, the standard deviation is not uniform for each case, but it is changing with the geometry considered. Hence, this suggests that, for different cases, it is modelled in different ways.

Table 4-4: Values of average and standard deviation of the total pressure loss coefficient

Geometry	i [deg]	Steady State	URANS k-ω SST		SST-SAS	
		ω [-]	ω_{Avg} [-]	ω_{StdDvt} [%]	ω_{Avg} [-]	ω_{StdDvt} [%]
IR8	$-42°$	1.307	1.303	0.94	1.202	0.80
($\Delta\theta = -11.65°$)	$-82°$	2.310	2.316	0.0014	2.316	0.048
HR1	$-42°$	1.572	1.556	13.17	1.333	48.72
($\Delta\theta = -8.83°$)	$-82°$	3.015	3.044	2.80	2.603	25.94
HR6 ($\Delta\theta = -1.50°$)	$-82°$	2.822	2.868	0.00046	1.784	33.47

In conclusion, whilst the URANS k-ω SST model can be trusted since it gives the same outcomes for each geometry, the SST-SAS model is not reliable when it comes to parametric studies. This is probably due to the different way in which the turbulence is modelled in the two approaches, as it is discussed in further details in Section 4.5. However, further work should be done in this direction in order to understand which of the two models is more appropriate for the current study, analysing the ways in which the turbulence is modelled. In fact, it is also possible that the RANS k-ω SST model is overestimating this quantity.

4.4.2 Deflection Angle

Regarding the deflection angle, as for the total pressure loss coefficient, the URANS k-ω SST model results totally agree with the steady-state ones, giving a negligible error. In Table 4-5 are provided the numerical values for each geometry and incidence. Furthermore, a summary of all the four geometries is provided in Figure 4-22. However, unlike the pressure loss coefficient, in this case the SST-

SAS model gives almost the same results, without the great discrepancy seen before. Hence, the steady-state formulation for the deflection angle can be considered reliable since all the transient results are very close to it.

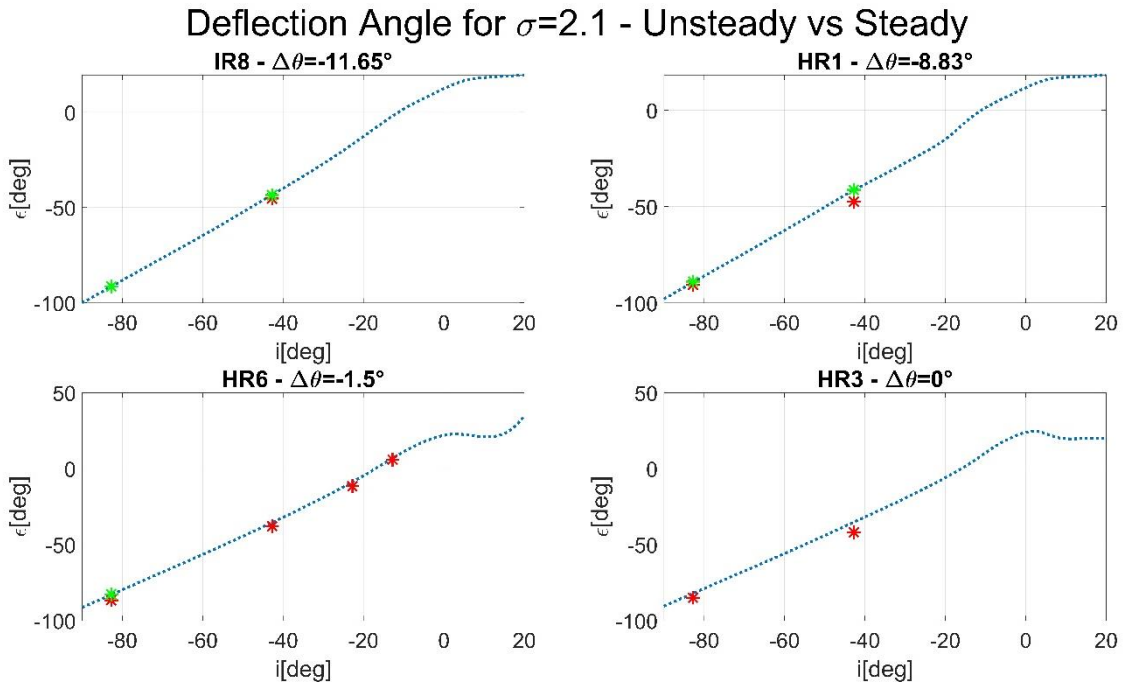

Figure 4-22: Summary of average and standard deviation of the deflection angle; in red the SST-SAS model results, in green the URANS model ones.

Table 4-5: Values of average and standard deviation of the deflection angle

Geometry	i [deg]	Steady State	URANS k-ω SST		SST-SAS	
		ϵ [deg]	ϵ_{Avg} [deg]	ϵ_{StdDvt} [%]	ϵ_{Avg} [deg]	ϵ_{StdDvt} [%]
IR8	$-42°$	-43.44	-43.48	0.0069	-45.29	0.034
($\Delta\theta = -11.65°$)	$-82°$	-91.51	-91.48	0.0000069	-91.48	0.00031
HR1	$-42°$	-41.49	-41.32	0.23	-47.45	5.07
($\Delta\theta = -8.83°$)	$-82°$	-89.32	-88.97	0.015	-90.60	3.43
HR6 ($\Delta\theta = -1.50°$)	$-82°$	-82.99	-82.71	0.0000056	-86.62	1.48

However, due to the different behaviour of the SST-SAS model for the two different flow variables, it is the author's opinion that a further analysis should be conducted to understand the ways the turbulence is modelled. In the last subchapter, some considerations are discussed for giving an explanation to these discrepancies.

4.5 Turbulence Resolution

As mentioned before, the SST-SAS model is giving controversial results dependent on the considered geometry. In fact, as it is shown in Figure 4-21, both the deviation of the time-averaged values from the steady-state model and the standard deviations cannot be classified in a trend: they are different for each geometry considered. It is the author's opinion that the cause for this is in the implicit nature of the SST-SAS model: since it is a Scale-Adaptive Simulation model, then it is capturing a different level of turbulence for each geometry.

This happens because in ANSYS Fluent this process is not possible to control: the final user cannot decide the level of turbulence that is solved and the one that is modelled. In fact, as explained in Section 3.1.4.2, the turbulence length scale is calculated by the model itself, auto-adapting to the different flow features and structures, possibly ending converging to the URANS k-ω SST model from which it is derived. Due to slight differences in the geometry, such as the leading or trailing edge thickness or a small change in the blade angles, a different range of turbulent length scales is then considered, with the different outcomes showed previously.

In the current project, in which a parametric study is performed with different geometries, this characteristic can be a big problem, since without controlling the actual turbulence modelled it is then impossible to make direct comparisons between the results. To be noticed that this is happening even though the mesh size is the same and, hence, the model should solve the same structures and model the rest of them.

The discrepancy between the URANS k-ω SST model and the SST-SAS one is visible in the following figures. In Figure 4-23, it is shown the difference in the level of turbulence that the SST-SAS model is capturing and solving, compared to the k-ω SST one. As it is clear, the power of the turbulence captured is much higher for the SST-SAS, meaning that it is more resolved through the flow structures than modelled. Moreover, the slopes of the spectrum are different: while for the URANS k-ω SST model the spectrum presents a flat trend, in the SST-SAS model there is a descending slope, meaning that a part of the energy decay is modelled. However, a singularity is present in this plot: in the IR8 case (hence the lowest cambered blade), both the turbulence models have a similar spectrum. This means that, in this case, the SST-SAS model is converging to the URANS k-ω SST one.

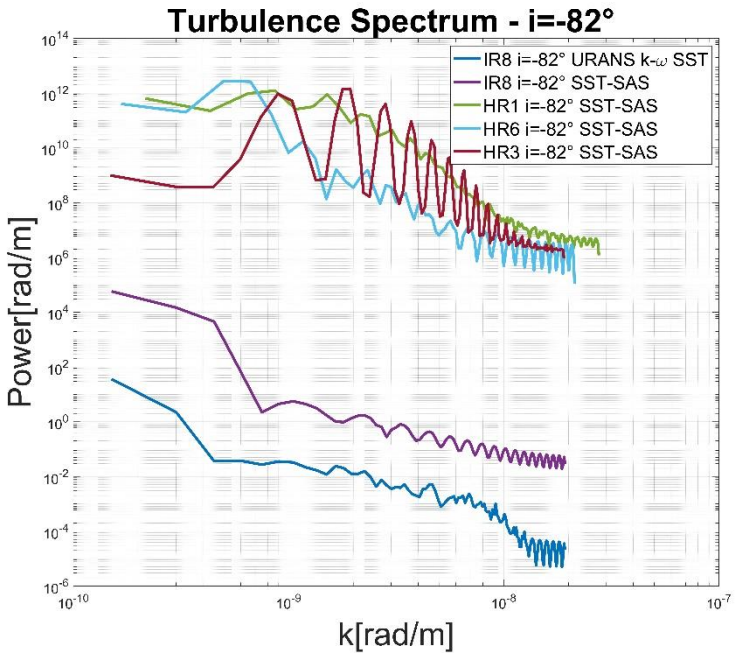

Figure 4-23: Comparison of the turbulence spectrum between SST-SAS model and URANS k-ω SST one, with the singularity of the IR8 geometry

In Figure 4-24 this issue is more visible. For the HR6 geometry, the difference in turbulent spectrum between the two models is significant, with the SST-SAS one that has a different slope and a higher power spectrum compared to the URANS k-ω SST one. For the IR8 geometry, the two spectrums are instead almost the

same. This means that, in this specific case, they are capturing the same level of turbulence, with the SST-SAS model that is converged to the URANS k- ω SST. Most likely this is the reason why, for this case, the total pressure loss coefficient has a high discrepancy between the two models.

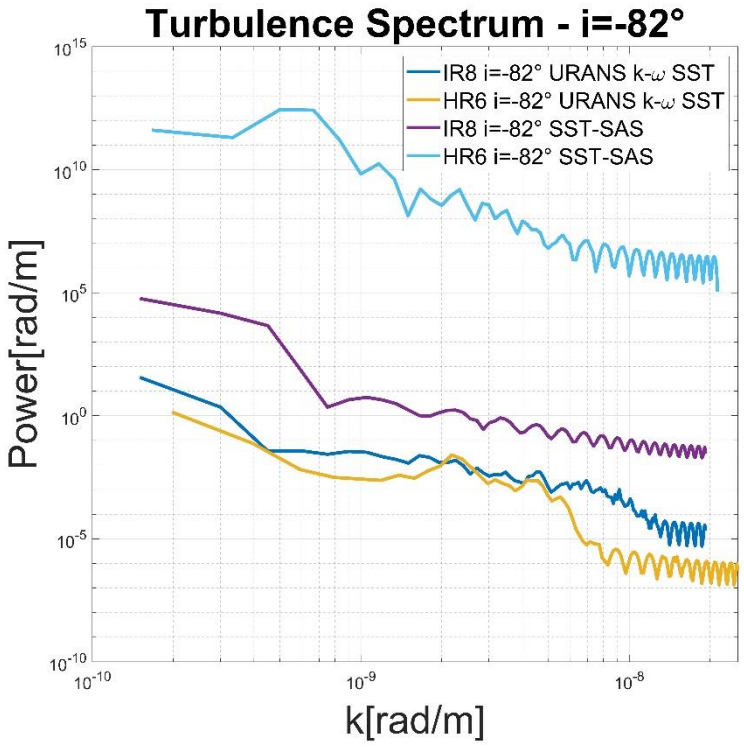

Figure 4-24: Comparison of the turbulence spectrum of the HR6 and IR8 geometries, with the two different turbulence models

This discussion is supported as well by the different values of the turbulent kinetic energy modelled in the flow field, plotted as contours for the IR8 and HR6 geometries and for the two different turbulence models. For the HR6 case, Figure 4-25 (at $i = -82°$) shows that there is a significant difference between the two models: for the SST-SAS case, the modelled turbulent kinetic energy is much lower than the one of the URANS k-ω SST one. The reason for this is that in the first case smaller length scales are solved in the flow structures, and hence the modelled turbulent kinetic energy is lower. This is also visible in the flow pattern: in the SST-SAS case, the structures solved in the wake are much more complex the URANS k-ω SST ones, that are much more linear since the smaller scales

are not captured. For the IR8 case, in Figure 4-26 (at $i = -82$) it is clear that the two models are not behaving in a different way: they are modelling the same level of turbulence, without solving the smaller length scales, and a similar flow field.

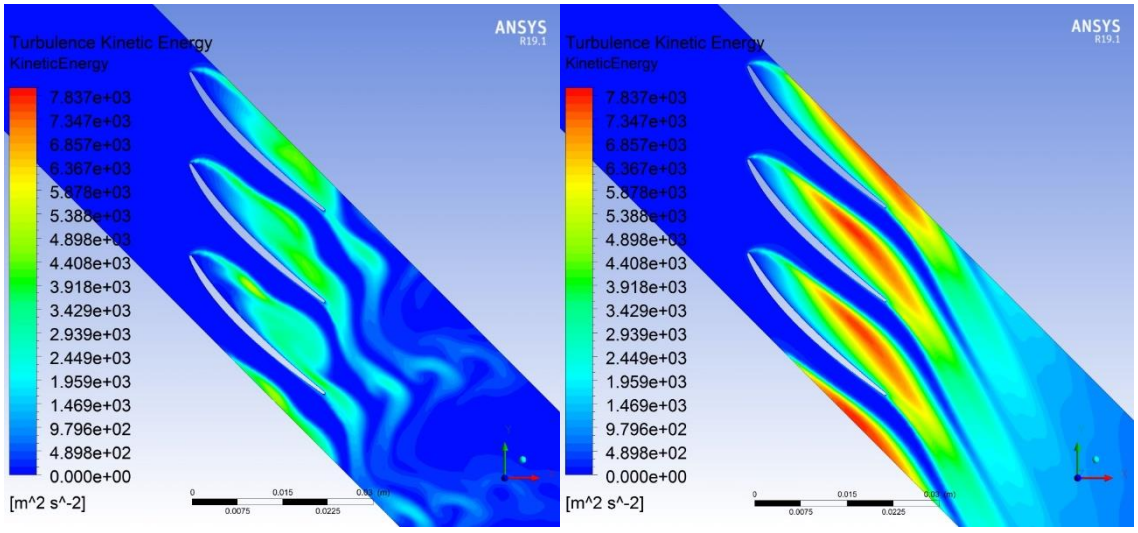

Figure 4-25: Turbulence kinetic energy contours of the HR6 geometry for the SST-SAS model (on the left) and the URANS k-ω SST one (on the right)

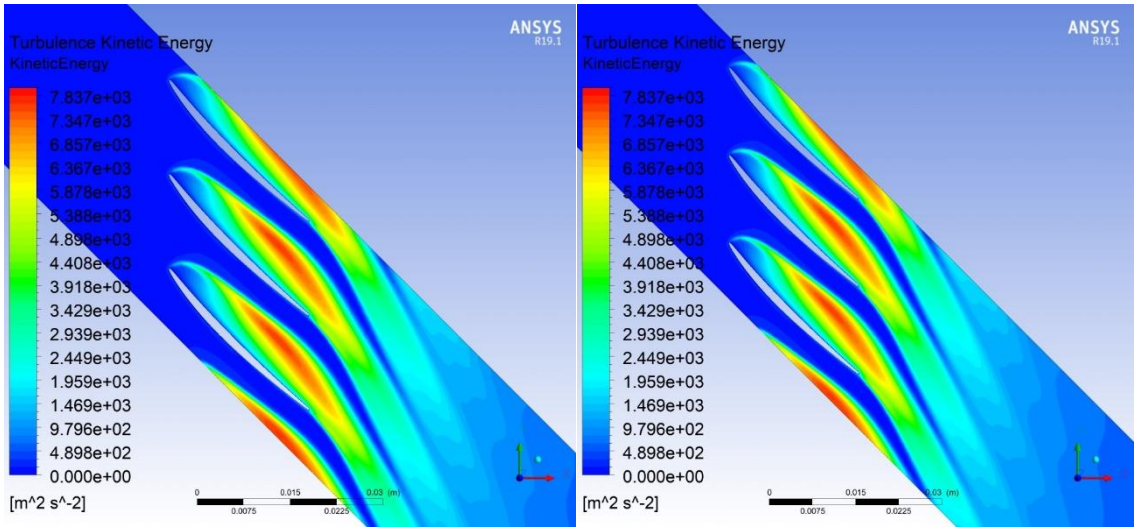

Figure 4-26: Turbulence kinetic energy contours of the IR8 geometry for the SST-SAS model (on the left) and the URANS k-ω SST one (on the right)

Since there is so much discrepancy in the behaviour of the SST-SAS model with the different geometries, it is then necessary to understand why this is happening and how this can be solved. Moreover, due to these discrepancies, the

dependence of the total pressure loss coefficient from the camber angle is still not clear. In fact, the differences seen in the transient results (Figure 4-21) can be due to both the factors. In the future, further work should be done in order to understand the effect of the camber angle on the total pressure loss coefficient, decoupling the effect of the geometry change on the considered turbulence model.

5 CONCLUSIONS

In this chapter, the conclusions to the work performed in the current project will be presented. In addition, suggestions for further work to be done will be provided.

5.1 Concluding Remarks

The work done in the current project was focused on two main topics: the assessment of the camber angle influence on the existing correlations and the evaluation of the applicability of the steady-state approach to clearly unsteady flows. In fact, at high negative incidence, a huge separation bubble on the pressure side of the blades, and the consequent vortex shedding in the wake, are occurring.

For the first part, four different geometries, with four different camber angles have been simulated. The range of camber angles has been chosen considering the modern compressors geometries, limited by the aerodynamic issues encountered by the flow, such as the boundary layer separation due to the adverse pressure gradient. The numerical model was set to support the parametric study by changing systematically the solidity and the incidence angle within the ranges considered significant for sub-idle operating conditions. The sensitivity studies for the mesh and solver settings have been conducted, hence the results are can be considered reliable.

Simplified correlations for the zero-lift incidence and the deflection angle have been found. The zero-lift incidence has been considered as a linear function of the solidity and the camber angle. Once the zero-lift incidence correlation was set, then the deflection angle one has been considered. It was assumed as a linear function of the incidence, with validity until the stall incidence. The effect of the camber was implicit in the zero-lift incidence, from which every line was constrained to pass through. The effect of solidity has been considered to have an influence on the slope coefficient. It has been evaluated crossing the data of the current project with the previous year project, in order to have a better fitting

of the curves. It resulted that the solidity is affecting the linear slope coefficient only for values below 1.4, after which it is constant. The difference between the CFD data and the approximated ones has been considered. Although for the two lowest camber angles the error is very small, for the other two it is quite high and the approximation not accurate enough. For this reason, the deviation angle has been considered as well.

Analysing the difference of deviation angle from the baseline model, it resulted that the camber angle has no influence on it. In fact, for $i < -15°$, it is very close to 0 for every camber angle considered. Hence, the change in deflection due to the camber angle can be considered the camber angle itself.

This is suggesting that no modifies are needed to the existing model for the part of the deviation angle and, hence, the mean-line code in which the model will be implemented will just need to consider the difference of blade camber angle to calculate the difference of deflection, with a ratio of $1:1$.

Regarding the total pressure loss coefficient, it is mostly dependent on the solidity, since the curves are grouped based on that. However, the trend for the change in the camber angle is not clear. It is the author opinion that this is due to other factors rather than the camber angle, such as the unsteadiness effects.

Hence, the possibility of some discrepancies between the steady-state approach and the unsteady one was considered. Two different turbulence models for the unsteady analysis have been employed: a URANS k-ω SST model and an SST-SAS one.

The first part of this analysis assessed the validity of the steady-state results. Regarding the deflection angle, it is confirmed by both the considered turbulence models that the steady-state values are reliable since a negligible difference between the three is registered. For the total pressure loss coefficient, whilst the URANS k-ω SST model confirmed the steady-state results with the same behaviour for each geometry, the SST-SAS model showed a different response. In fact, for some of the geometries it was really close to the steady-state results,

while for some other ones the discrepancy was much higher. The reason for this is probably due to the approach with which this model is dealing with the turbulence: although it is derived from the URANS k-ω SST one, it includes an additional scale-adaptive term that is changing automatically the solved turbulence range, allowing theoretically more accurate results. However, for a parametric study as the current one, this characteristic can raise some problems. It is the author's opinion that, since the solved turbulence length scale cannot be controlled, then a slight change in the geometry can trigger or not this mechanism, giving, as a result, a different behaviour and a different way in which the turbulence is solved. Thus, different total pressure loss coefficient values can be found, although it should give the same ones.

5.2 Suggestions for Further Work

Throughout this project, the camber parameter to be considered for having a wide enough data range has been considered. However, some hints for further work to be done to improve the understanding of the physical phenomena are provided.

The problem encountered in the unsteady analysis with the turbulence models should be further investigated to understand why the SST-SAS model is giving much different results when compared to the URANS k-ω SST one. The level of solved and modelled turbulence should be then considered, as well as the way to control it. Once understood how the basic model in working, the effect on the geometry should be considered. Once removed this variable from the results, the analysis of the total pressure loss coefficient dependence from the camber angle should be then considered, refining its understanding.

Moreover, since the turbulence is a highly 3D phenomena, a 3D model of the same geometries considered for the 2D case should be considered. For this case, it would be useful to quantify the effect of the 3D phenomena on both the deviation angle and the total pressure loss coefficient and verify the validity of the overall trends found in the current project.

REFERENCES

[1] Walsh, P. P. and Fletcher, P. (2004) *Gas Turbine Performance*. 2nd edn. Oxford, UK: Blackwell Science Ltd. doi: 10.1016/b978-185617472-5/50033-2.

[2] Iglesias Perez, A. (2018) *Scale-Resolving Simulations of Compressor Blading at Negative Incidences*. Cranfield University.

[3] Agrawal, R. K. and Yunis, M. (1981) 'A Generalized Mathematical Model to Estimate Gas Turbine Starting Characteristics', *Journal of Engineering for Power*, 104(1), pp. 1–8. doi: 10.1115/1.3227249.

[4] Aslanidou, I., Zachos, P. K., Pachidis, V. and Singh, R. (2010) 'A Physically Enhanced Method for Sub-idle Compressor Map Generation and Representation', in *ASME Turbo Expo 2010: Power for Land, Sea and Air*, pp. 1–10.

[5] Grech, N. (2013) *Gas Turbine Performance Modelling: Groundstart, Altitude Relight and Windmilling*. Cranfield University.

[6] Howard, J. (2007) *Sub-idle Modelling of Gas Turbines: Altitude Relight and Windmilling*. Cranfield University.

[7] Dixon, L. S. and Hall, C. A. (2014) *Fluid Mechanics and Thermodynamics of Turbo-Machinery*. 7th edn. Oxford, UK: Elsevier Inc.

[8] Allegretti, A. (2018) *Sub-idle Loss and Deviation Models for Modern Compressor Blading*. Cranfield University.

[9] Jones, G., Pilidis, P. and Curnock, B. (2002) 'Extrapolation of Compressor Characteristics to the Low-speed Region for Sub-idle Performance Modelling', in *ASME Turbo Expo 2002*. Amsterdam, Netherlands: ASME, pp. 1–7.

[10] Zachos, P. K. (2010) *Gas Turbine Sub-idle Performance Modelling: Altitude Relight and Windmilling*. Cranfield University. doi: 10.1177/0885066613507420.

[11] Zachos, P. K., Aslanidou, I., Pachidis, V. and Singh, R. (2011) 'A Sub-idle Compressor Characteristic Generation Method With Enhanced Physical

Background', *Journal of Engineering for Gas Turbines and Power*, 133, pp. 1–8. doi: 10.1115/1.4002820.

[12] Hill, P. G. and Peterson, C. R. (1992) *Mechanics and Thermodynamics of Propulsion*. 2nd edn. USA: Addison-Wesley Publishing Company.

[13] Boyce, M. P. (2012) *Gas Turbine Engineering Handbook*. 2nd edn. Oxford, UK: Elsevier Ltd. doi: 10.1115/1.859537.ch4.

[14] Johnsen, I. A. and Bullock, R. O. (1956) *Aerodynamic Design of Axial-Flow Compressors*. Cleveland, Ohio.

[15] Denton, J. D. (1993) 'Loss Mechanisms in Turbomachines', in *International Gas Turbine and Aeroengine Congress and Exposition*. Cincinnati, Ohio: ASME, pp. 1–40. doi: 10.1115/93-GT-435.

[16] Schneider, M. (2017) *Compressor Blade Performance Under Sub-Idle Operating Conditions*. Cranfield University.

[17] Howell, A. R. (1945) 'Fluid Dynamics of Axial Compressors', in *Institution of Mechanical Engineers*, pp. 441–452. doi: 10.1243/PIME_PROC_1945_153_049_02.

[18] Lieblein, S. and Roudebush, W. H. (1956) *Theoretical Loss Relations for Low-speed Two-Dimensional Cascade Flow*. Cleveland, Ohio.

[19] Swan, W. C. (1961) 'A Practical Method of Predicting Transonic-Compressor Performance', *Journal of Engineering for Power*, 83(3), pp. 322–330. doi: 10.1115/1.3673194.

[20] Creveling, H. F. and Carmody, R. H. (1968) *Axial Flow Compressor Computer Program for Calculating Off-Design Performance*. Indianapolis, Indiana.

[21] Koch, C. C. and Smith, L. H. (1976) 'Loss Sources and Magnitudes in Axial-Flow Compressors', *Journal of Engineering for Power*, 98(3), pp. 411–424. doi: 10.1115/1.3446202.

[22] Çetin, M., Üçer, A., Hirsch, C. and Serovy, G. K. (1987) *Application of Modified Loss and Deviation Correlations to Transonic Axial Compressors*. Nuilly sur Seine.

[23] König, W. M., Hennecke, D. K. and Fottner, L. (1994) 'Improved Blade Profile Loss and Deviation Angle Models for Advanced Transonic Compressor Bladings: Part I - A Model for Subsonic Flow', in *International Gas Turbine and Aeroengine Congress and Exposition*. The Hague, Netherlands: ASME, pp. 1–9.

[24] Carter, S. (1949) *The Low Speed Performance of Related Aerofoils in Cascades*. London.

[25] Lieblein, S. (1960) 'Incidence and Deviation-Angle Correlations for Compressor Cascades', *Journal of Basic Engineering*, 82(3), p. 575. doi: 10.1115/1.3662666.

[26] Rülke, C. (2009) 'Experimental / CFD Analysis of the flow through a "locked" HP compressor'.

[27] Tu, J., Yeoh, G. H. and Liu, C. (2012) *Computational Fluid Dynamics - A Practical Approach*. 2nd edn. Elsevier Science and Technology.

[28] Mgbemene, C. A. (2012) 'The Design and Fabrication of Low Speed Axial-Flow Compressor Blades by Joukowski Transformation of a Circle', *International Journal of Engineering Research & Technology (IJERT)*, 1(8), pp. 1–17.

[29] ANSYS Inc. (2018) *ANSYS Meshing User's Guide*. Release 19. USA.

[30] ANSYS Inc. (2018) *ANSYS Fluent User's Guide*. Release 19. USA.

[31] ANSYS Inc. (2016) *Introduction to ANSYS Fluent, Module 07: Turbulence*. Release 17, *Introduction to ANSYS Fluent*. Release 17. USA.

[32] Camp, T. R. and Shin, H.-W. (1994) 'Turbulence Intensity and Length Scale Measurements in Multistage Compressors', in *International Gas Turbine and Aeroengine Congress and Exposition*. ASME, p. 10. doi: 10.1115/94-GT-004.

[33] Mockett, C. (2009) *A Comprehensive Study of Detached-Eddy Simulation*.

Universitatsverlag der TU Berlin.

[34] Kajishima, T. and Taira, K. (2017) *Computational Fluid Dynamics*. Springer.

[35] ANSYS Inc. (2018) *ANSYS Fluent Theory Guide*. Release 19. USA.

[36] Zachos, P. K., Grech, N., Charnley, B., Pachidis, V. and Singh, R. (2011) 'Experimental and Numerical Investigation of a Compressor Cascade at Highly Negative Incidence', *Engineering Applications of Computational Fluid Mechanics*, 5(1), pp. 26–36. doi: 10.1080/19942060.2011.11015350.

[37] Menter, F. R. (1994) 'Two-Equation Eddy-Viscosity Turbulence Models for Engineering Applications', *AIAA Journal*, 32(8), pp. 1598–1605. doi: 10.2514/3.12149.

[38] Menter, F. and Egorov, Y. (2005) 'A Scale Adaptive Simulation Model using Two-Equation Models', in *43rd AIAA Aerospace Sciences Meeting and Exhibit*. Reston, Virigina: American Institute of Aeronautics and Astronautics. doi: 10.2514/6.2005-1095.

[39] Rotta, J. C. (1972) *Turbulente Strömungen*. Stuttgart: Vieweg+Teubner Verlag. doi: 10.1007/978-3-322-91206-0_3.